Title

Search for a Very Light NMSSM Higgs Boson Produced in Decays of the 125 GeV Scalar Boson and Decaying Into tau Leptons in pp Collisions at the LHC

Author

Shrinivas, Amithabh

Publication Date

2016

UNIVERSITY OF CALIFORNIA
RIVERSIDE

Search for a Very Light NMSSM Higgs Boson Produced in Decays of the 125 GeV Scalar Boson and Decaying Into tau Leptons in pp Collisions at the LHC

A Dissertation submitted in partial satisfaction
of the requirements for the degree of

Doctor of Philosophy

in

Physics

by

Amithabh Shrinivas

August 2016

Dissertation Committee:

Professor Robert Clare, Chairperson
Professor Steve Wimpenny
Professor Owen Long

The Dissertation of Amithabh Shrinivas is approved:

Committee Chairperson

University of California, Riverside

Acknowledgments

First and foremost, I would like to thank my advisors Prof. Robert Clare and Prof. Steve Wimpenny for their continuous support throughout my Ph.D, for their patience, motivation, and immense knowledge. They have supported me not only academically but also emotionally through the rough road to finishing this thesis. I could not have imagined having a better advisor and mentor for my Ph.D. Besides my advisors, I would like to thank Prof. Owen Long who was part of my thesis committee, for his insightful comments and encouragement, but also for the hard questions which incentivized me to widen my research from various perspectives. My sincere thanks also goes to Dr. Alexei Rasperaza from DESY who provided me an opportunity to join their group as a graduate student, and who wholeheartedly helped throughout my research. Without his precious support it would not be possible to conduct this research. I would like to thank my fellow students for the stimulating discussions, for the sleepless nights we were working together before comps, and for all the fun we have had during the first two years of my coursework. I also thank my friends Manuel, Pawandeep and Jesse for their support during my stint at CERN. Last but not the least, I would like to thank my family: my parents and to my brother and sister for supporting me spiritually throughout writing this thesis and my life in general.

To my family for all the support.

ABSTRACT OF THE DISSERTATION

Search for a Very Light NMSSM Higgs Boson Produced in Decays of the 125 GeV Scalar Boson and Decaying Into tau Leptons in pp Collisions at the LHC

by

Amithabh Shrinivas

Doctor of Philosophy, Graduate Program in Physics
University of California, Riverside, August 2016
Professor Robert Clare, Chairperson

A search for a very light Higgs boson decaying into a pair of tau leptons is presented within the framework of the next-to-minimal supersymmetric standard model(NMSSM). This search is based on a data set corresponding to an integrated luminosity of 19.7 fb^{-1} and 2.5 fb^{-1} of proton-proton collisions collected by the CMS experiment at a centre-of-mass energy of 8 TeV and 13 TeV respectively. The signal consists of the production of either of the two lightest scalars, h_1 or h_2, via gluon-gluon fusion and subsequent decay into a pair of the lightest Higgs bosons, a_1 or h_1. The h_1 or h_2 boson is identified with the observed state at a mass of 125 GeV. The analysis searches for decays of the $\mathrm{a}_1(\mathrm{h}_1)$ states into pairs of tau leptons and covers a mass range for the $\mathrm{a}_1(\mathrm{h}_1)$ boson of 4 to 15 GeV. The search reveals no significant excess in data above standard model background expectations, and an upper limit is set on the signal production cross section times branching fraction as a function of the $\mathrm{a}_1(\mathrm{h}_1)$ boson mass.

Contents

List of Figures

List of Tables

Chapter 1

Introduction

"*From the earliest times, man's dream has been to comprehend the complexity of nature in terms of as few unifying concepts as possible...*"

Dr. Abdus Salam

1.1 Standard Model of Particle Physics

The Standard Model (SM) of particle physics is a theory of elementary particles and their interactions. Practically, all the experimental data from high energy experiments can be accounted for by it. There are three kinds of elementary particles that constitute all matter: leptons, quarks and gauge bosons(mediators). There are six flavors of spin-$\frac{1}{2}$ leptons, classified according to their charge (Q), electron number (L_e), muon number (L_μ), and tau number (L_τ), which naturally fall into three generations. The known leptons come in two categories: the electron (e), the muon(μ), and the tau (τ), each with one unit of electric charge, and three corresponding neutrinos (ν_e, ν_μ, ν_τ), which are electrically neutral.

Leptons do not interact via the strong interaction. Similarly, there are six flavors of spin-1/2 quarks, classified by charge (Q), strangeness (S), charm (C), beauty (B) and truth (T) which also fall into three generations. The 6 known flavors of quarks are either "up-type"quarks - the up (u), charm (c), and top (t) quarks - carrying an electric charge of +2/3, or "down-type"quarks - the down (d), strange (s), and bottom (b) quarks - carrying an electric charge of -1/3. Quarks also carry "color charge", a property related to the strong interaction. Each flavor of quark comes in three colors. While leptons exist as free particles, quarks do not seem to do so. This phenomenon is called quark confinement [5].

The Standard Model (SM) includes three basic types of interactions: namely electromagnetic, weak and strong interaction. Gravity remains excluded from this model. Every interaction has a mediator - the photon (γ) for the electromagnetic interaction, W^+, W^- and Z boson for the weak interaction and gluons(g) for the strong interaction. They are spin-1 particles collectively called the gauge bosons. The photon is massless and electrically neutral while W and Z bosons are massive. Eight massless gluons mediate the strong interaction between quarks which carry a color charge; gluons themselves also carry color charge as a result of which they have the special ability to interact with other gluons. In all, there are about 25 free parameters in the standard model which are to be obtained experimentally and not provided by the model. These include the masses of the 12 fermions, a coupling constant for each of the 3 interactions, the vacuum expectation value of the Higgs field, the mass of the Higgs boson, the 4 angles of the Pontecorvo-Maki-Nakagawa-Sakata [6] weak mixing matrix and the 4 angles of the Cabibbo-Kobayashi-Maskawa [7,8] quark mixing matrix.

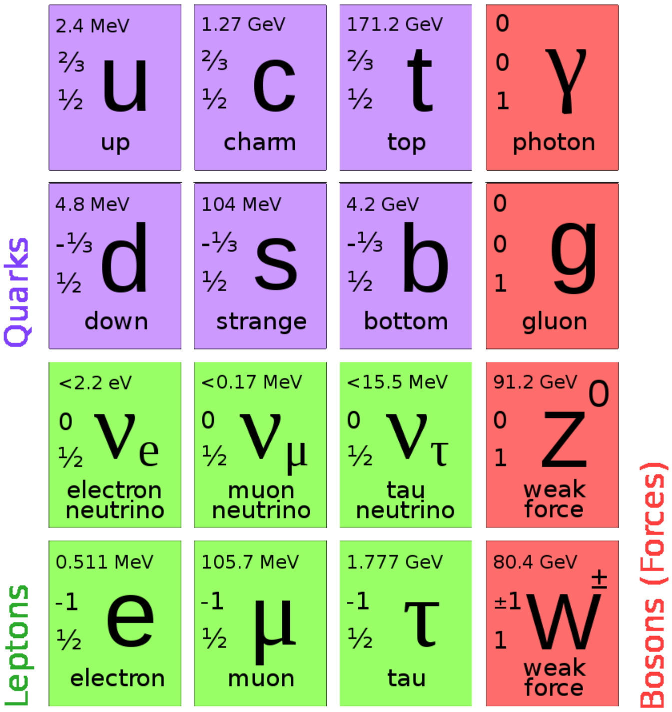

Figure 1.1: Standard Model

Mathematically, the SM is formulated as a quantum field theory with the gauge symmetry group $SU(3)_c \otimes SU(2)_L \otimes U(1)_Y$ [9]. Here the subscript c denotes color,L means the fields participating in the interaction are left-handed and Y denotes the weak hypercharge. The strong interaction between quarks and gluons, is governed by the $SU(3)_c$ subgroup. $SU(2)_L$ is the symmetry of weak isospin which couples only to “left-handed” chiral states and $U(1)_Y$ the symmetry of weak hypercharge.

Table 1.1: Chiral fields in Standard Model

	Spin-$\frac{1}{2}$	Representation under $SU(3)_c \otimes SU(2)_L \otimes U(1)_Y$
quarks	$(\mathrm{u}_L, \mathrm{d}_L)$	(3, 2, $\frac{1}{6}$)
	$\mathrm{u}_R^\dagger$	($\bar{3}$, 1, -$\frac{2}{3}$)
	$\mathrm{d}_R^\dagger$	($\bar{3}$, 1, $\frac{1}{3}$)
leptons	(ν_L, e_L)	(1, 2, -$\frac{1}{2}$)
	$\mathrm{e}_R^\dagger$	(1, 1, 1)

Table 1.2: Gauge Fields in Standard Model

	Spin-1	Representation under $SU(3)_c \otimes SU(2)_L \otimes U(1)_Y$
gluons	g	(8, 1, 0)
W^μ	$W^\pm, W^0$	(1, 3, 0)
B^μ	(u_L, d_L)	(1, 1, 0)

1.1.1 Quantum Chromodynamics

Quantum Chromodynamics (QCD) [10] is a quantum field theory of strongly interacting fundamental particles namely quarks mediated by gluons. Mathematically, it is a renormalizable non-Abelian gauge theory of the $SU(3)_c$ subgroup in the Standard Model. The field theory on whose basis QCD was eventually built, Yang-Mills theory [11] is a generalized principle of local gauge invariance applied to non-Abelian gauge groups. The generators of the color SU(3) group do not commute with each other due to its non-Abelian nature and hence follow the commutation relation,

$$[T_a, T_b] = i f_{abc} T_c \tag{1.1}$$

where f_{abc} are the structure constants of the group.

Only quarks and gluons participate in strong interactions. In QCD, we have three fields for each flavor of quark which are required by Pauli's Exclusion Principle. These are put into so-called color triplets. For example, the up quark is associated with the triplet,

$$\begin{pmatrix} \mathrm{u}_r \\ \mathrm{u}_g \\ \mathrm{u}_b \end{pmatrix} \tag{1.2}$$

where $\mathrm{u}_r, \mathrm{u}_g, \mathrm{u}_b$ are four-component Dirac spinors, and the subscripts r, g, b label the color states(red, green, blue). Only color singlets are found to exist freely in nature. The quarks interact with each other by the exchange of gluons, which are massless vector particles belonging to the octet representation of SU(3) which are introduced as a result of requiring gauge invariance. Even though the coupling constant is large in QCD, perturbation theory has been successful in describing the strong interactions. This has been possible only due to the property of Asymptotic freedom [12] of quarks wherein the coupling strength is small enough at small distances or large energies so that Perturbative techniques apply. Probing such small distances have been realized with the help of high energy particle colliders of today. The QCD Lagrangian for a vector field is given by [13],

$$\mathcal{L}_{QCD} = \mathcal{L}_{free} + \mathcal{L}_{interaction} + \mathcal{L}_{kinetic} \tag{1.3}$$

where,

$$\mathcal{L}_{free} = \bar{q}(i\gamma^\mu \partial_\mu - m)q \tag{1.4}$$

$$\mathcal{L}_{interaction} = -g(\bar{q}\gamma^\mu T_a q)G^a_\mu \tag{1.5}$$

$$\mathcal{L}_{kinetic} = -\frac{1}{4}G^a_{\mu\nu}G^{\mu\nu}_a \tag{1.6}$$

1.1.2 Electroweak Unification

The electroweak theory is a unified gauge theory of the $SU(2)_L \otimes U(1)_Y$ subgroup in the Standard Model. The weak isospin operator generates the symmetry group $SU(2)_L$ while the hypercharge operator generates the symmetry group $U(1)_Y$ related by,

$$Q = T_3 + \frac{Y}{2} \tag{1.7}$$

where Q is the electric charge and T_3 is the third component of weak isospin.

The $SU(2)_L \otimes U(1)_Y$ symmetry group is formed by the two charged currents J_μ and $J^\dagger_\mu$ defined as,

$$J_\mu = \bar{\nu}_L \gamma_\mu \mathrm{e}_L \tag{1.8}$$

$$J^\dagger_\mu = \bar{\mathrm{e}}_L \gamma_\mu \nu_L \tag{1.9}$$

and an orthogonal combination of the weak neutral current J^3_μ and the weak hypercharge current J^Y_μ defined as,

$$j^{em}_\mu = J^3_\mu + \frac{1}{2} j^Y_\mu \tag{1.10}$$

where,

$$J^3_\mu = \frac{1}{2}\bar{\nu}_L\gamma_\mu\nu_L - \frac{1}{2}\bar{\mathrm{e}}_L\gamma_\mu \mathrm{e}_L \tag{1.11}$$

$$j^Y_\mu = \bar{\psi}\gamma_\mu Y\psi \tag{1.12}$$

where e and ν are the electron and neutrino spinors.

The $SU(2)_L$ transformations of weak isospin operate only on left-handed fermion doublets, which can be represented as,

$$\begin{pmatrix} \nu_e \\ \mathrm{e} \end{pmatrix}_L, \begin{pmatrix} \nu_\mu \\ \mu \end{pmatrix}_L, \begin{pmatrix} \nu_\tau \\ \tau \end{pmatrix}_L \tag{1.13}$$

for leptons and

$$\begin{pmatrix} \mathrm{u} \\ \mathrm{d}' \end{pmatrix}_L, \begin{pmatrix} \mathrm{c} \\ \mathrm{s}' \end{pmatrix}_L, \begin{pmatrix} \mathrm{t} \\ \mathrm{b}' \end{pmatrix}_L \tag{1.14}$$

for quarks. The left-handed doublets have weak isospin T=1/2, while right-handed fermions form isospin singlets with T=0 and do not couple to the $SU(2)_L$ gauge field. They are denoted as $\mathrm{e}_R, \mu_R, \tau_R$ (leptons) and $\mathrm{u}_R, \mathrm{d}'_R, \mathrm{c}_R, \mathrm{s}'_R, \mathrm{t}_R, \mathrm{b}'_R$ (quarks). The prime notation for quarks indicates that they are weak eigenstates which are a mixture of mass eigenstates as follows,

$$\begin{pmatrix} \mathrm{d}' \\ \mathrm{s}' \\ \mathrm{b}' \end{pmatrix} = V_{CKM} \begin{pmatrix} \mathrm{d} \\ \mathrm{s} \\ \mathrm{b} \end{pmatrix} \tag{1.15}$$

where V_{CKM} is the Cabibbo-Kobayashi-Maskawa quark mixing matrix. Unlike weak isospin, the weak hypercharge couples to both left-handed and right-handed components of fermions. Like QCD, the requirement of gauge invariance of the electroweak group introduces an isotriplet of vector fields W_μ^i associated with the $SU(2)_L$ symmetry group and a single vector field B_μ associated with $U(1)_Y$ symmetry group. The observable electroweak bosons - the charged W$^\pm$, the neutral Z, and the photon which are the mass eigenstates- are obtained from the mixing of the gauge fields by,

$$W_\mu^\pm = \frac{1}{\sqrt{2}}(W_\mu^1 \mp W_\mu^2) \tag{1.16}$$

$$Z_\mu = \cos\theta_W W_\mu^3 - \sin\theta_W B_\mu \tag{1.17}$$

$$A_\mu = \sin\theta_W W_\mu^3 + \cos\theta_W B_\mu \tag{1.18}$$

where θ_W is known as the weak mixing angle. It can be expressed in terms of the coupling constants of $SU(2)_L(g)$ and $U(1)_Y(g')$ by the relations,

$$\sin\theta_W = \frac{g'}{\sqrt{g^2 + g'^2}} \tag{1.19}$$

$$\cos\theta_W = \frac{g}{\sqrt{g^2 + g'^2}} \tag{1.20}$$

θ_W is a free parameter of the SM and is experimentally measured to be 30°. The Lagrangian for the electroweak group is given by,

$$\mathcal{L}_{electroweak} = \mathcal{L}_{fermionic} + \mathcal{L}_{kinetic} \tag{1.21}$$

where,

$$\mathcal{L}_{fermionic} = \bar{\chi}_L i\gamma^\mu(\partial_\mu + i\frac{g'}{2}YB_\mu + i\frac{g}{2}\tau^a W^a_\mu)\chi_L + \bar{\psi}_R i\gamma^\mu(\partial_\mu + i\frac{g'}{2}YB_\mu)\psi_R \tag{1.22}$$

$$\mathcal{L}_{kinetic} = -\frac{1}{2}W^a_{\mu\nu}W^{a\mu\nu} - \frac{1}{4}B_{\mu\nu}B^{\mu\nu} \tag{1.23}$$

Here χ_L, ψ_R denote a left-handed doublet and right-handed singlet of weak isospin respectively, γ^μ the Dirac matrices, τ^a the Pauli spin matrices, and Y the hypercharge operator. The $SU(2)_L \otimes U(1)_Y$ gauge symmetry of the electroweak Lagrangian prohibits mass terms for the gauge bosons of the form $M^2 W^a_\mu W^{a\mu}$ since they would break local gauge invariance and render the theory unrenormalizable. An explicit mass term for the fermions of the form,

$$m\bar{\psi}\psi = m(\bar{\psi}_L\psi_R + \bar{\psi}_R\psi_L) \tag{1.24}$$

violates $SU(2)_L$ gauge symmetry since the $SU(2)_L$ transformations operate differently on left-handed and right-handed states. However, the W and Z bosons and the fermions are experimentally known to be massive. This mass problem is solved by introducing spontaneous symmetry breaking via the Higgs mechanism.

1.1.3 Higgs Mechanism

The way to achieve spontaneous symmetry breaking, is to introduce scalar fields, called Higgs bosons which give rise to the Higgs mechanism [14–16]. Since we start with 4 gauge bosons(3 associated with $SU(2)_L$ and 1 with $U(1)_Y$) and finally want to have 1 massless photon associated with $U(1)_{em}$, we need scalars with at least 4 degrees of freedom. The simplest model of such scalars is an SU(2) doublet of 2 complex scalar fields whose weak hyper charge is Y_ϕ=+1,

$$\phi = \begin{pmatrix} \phi^+ \\ \phi^0 \end{pmatrix} = \frac{1}{\sqrt{2}} \begin{pmatrix} \phi_1 + i\phi_2 \\ \phi_3 + i\phi_4 \end{pmatrix} \tag{1.25}$$

The Lagrangian for the Higgs sector is then given by,

$$\mathcal{L} = (\partial_\mu \phi + i\frac{g}{2}\tau.W_\mu \phi)^\dagger (\partial^\mu \phi + i\frac{g}{2}\tau.W^\mu \phi) - V(\phi) - \frac{1}{4}W_{\mu\nu}W^{\mu\nu} \tag{1.26}$$

with,

$$V(\phi) = \mu^2 \phi^\dagger \phi + \lambda(\phi^\dagger \phi)^2 \tag{1.27}$$

where $\mu^2 < 0$ and $\lambda > 0$.

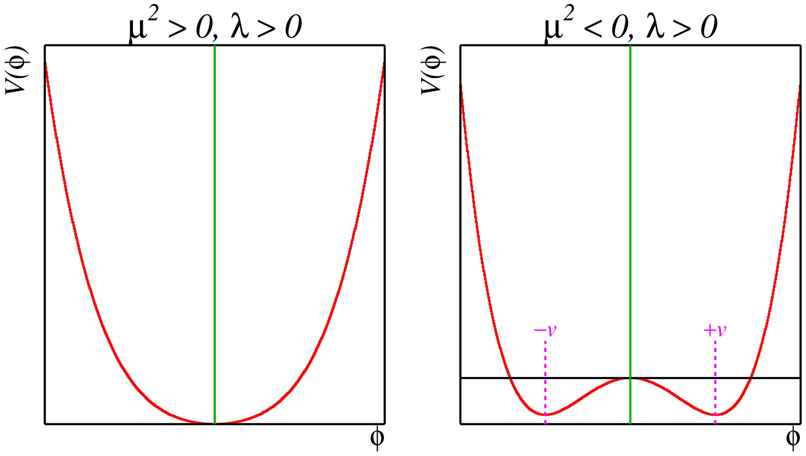

Figure 1.2: Comparison of potential having a symmetric vacuum state with a asymmetric vacuum state causing spontaneous symmetry breaking

The potential has its minima at,

$$\phi_1 = \phi_2 = \phi_3 = 0 \quad \text{and} \quad \phi_4 = -\frac{\mu^2}{2\lambda} \equiv v^2 \tag{1.28}$$

We now expand $\phi(x)$ about this particular vacuum:

$$\phi_0 = \frac{1}{\sqrt{2}} \begin{pmatrix} 0 \\ v \end{pmatrix} \tag{1.29}$$

We can recast the potential in the form of fluctuations about the vacuum state as,

$$\phi_0 = \frac{1}{\sqrt{2}} \begin{pmatrix} 0 \\ v + h(x) \end{pmatrix} \tag{1.30}$$

Here $h(x)$ is the Higgs field. Inserting it into the Lagrangian for Higgs and gauge fields, we end up with 3 massive vector fields and a massive scalar field. The masses generated for the gauge bosons can be obtained by comparing the terms in $\left|i\frac{g}{2}\tau.W_\mu{}^2\right|$ with typical mass terms of a boson with mass of W boson given by,

$$M_{\mathrm{W}} = \frac{1}{2} g v \tag{1.31}$$

and that of Z boson given by,

$$M_{\mathrm{Z}} = \frac{1}{2} v \sqrt{g^2 + g'^2} \tag{1.32}$$

1.2 Supersymmetry

The Standard Model though explains the real world quite well, it is still considered to be a low energy effective theory which is divergent at high energies.

- There is the ‘mass hierarchy’ problem. Within the SM, the mass of the Higgs particle is extremely sensitive to any new physics at higher energies and its natural value is of order of the Planck mass, if the SM is valid up to that scale. This is several orders of magnitude higher than the electroweak scale implied by experiment. The SM Higgs field (ϕ) is a complex scalar with a classical potential,

$$V = \mu^2\phi^2 + \lambda\phi^4 \tag{1.33}$$

The SM requires a non-vanishing vacuum expectation value (VEV) for ϕ at the minimum of the potential. This occurs if $\mu_H^2 < 0$ and $\lambda > 0$, resulting in $\langle\phi\rangle = \sqrt{-\frac{\mu_H^2}{2\lambda}}$. For a Higgs boson with a mass near 125 GeV, $\lambda = 0.126$ and $\mu_H^2 = -(92.9\ \text{GeV})^2$. The problem is that μ_H^2 receives enormous quantum corrections from the virtual effects of every particle or other phenomenon that couples, directly or indirectly, to the Higgs field. For example, in Figure 1.3, we have a correction to μ_H^2 from a loop containing a Dirac fermion f with mass m_f. If the Higgs field couples to f with a term in the Lagrangian $-\lambda_\text{f}\phi\text{ff}$, then the Feynman diagram in Figure 1.3 yields a correction [17],

$$\Delta\mu_H^2 = -\frac{|\lambda_\text{f}|^2}{8\pi^2}[\Lambda_{UV}^2 + ...] \tag{1.34}$$

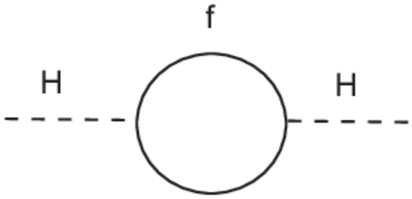

Figure 1.3: One-loop quantum corrections to the Higgs mass squared term μ_H^2 due to Dirac fermion f

Here Λ_{UV} is an ultraviolet momentum cutoff used to regulate the loop integral; it should be interpreted as at least the energy scale at which new physics enters to alter the high-energy behavior of the theory. Each of the leptons and quarks of the SM can play the role of f; for quarks, eq.(1.34) should be multiplied by 3 to account for color. The largest correction comes when f is the top quark with $\lambda_{\mathrm{f}} \approx 0.94$. The problem is that if Λ_{UV} is of order M_P, say, then this quantum correction to μ_{H}^2 is some 30 orders of magnitude larger than the required value of $\mu_{\mathrm{H}}^2 \approx -(92.9\ \mathrm{GeV})^2$. This is only directly a problem for corrections to the Higgs scalar boson squared mass, because quantum corrections to fermion and gauge boson masses do not have the direct quadratic sensitivity to Λ_{UV} found in eq.(1.34). However, the quarks and leptons and the electroweak gauge bosons $Z, W^{\pm}$ of the Standard Model all obtain masses from $\langle\phi\rangle$, so that the entire mass spectrum of the SM is directly or indirectly sensitive to the cutoff Λ_{UV}.

- The SM does not include gravity. It says absolutely nothing about one of the four fundamental forces of nature.

- There are many free parameters in the SM and moreover, it does not predict any unification of the gauge coupling constants at high energies(Planck scale).

- It does not explain why the charges of elementary particles are quantized.

- It does not describe the dark matter or the dark energy of the universe. Astronomical observations tell us that the ordinary baryonic matter is only a tiny fraction of the energy of the universe. There are observations that point towards the fact that a kind of non-luminous matter is out there and that it is actually much more abundant than baryonic matter, consisting of around 25 % of the total energy density of the universe.

Supersymmetry (SUSY) is a symmetry which connects particles and fields with different spin-statistics, i.e. bosons and fermions. SUSY is independent of any internal symmetry such as gauge symmetry, and therefore connects a pair of particles, "superpartners" of each other, with different spins but the same quantum numbers such as electric charge, weak isospin, color etc. A SUSY transformation turns a bosonic state into a fermionic state, and vice versa which is of the form,

$$Q\,|\text{Boson}\rangle = |\text{Fermion}\rangle\,, \qquad Q\,|\text{Fermion}\rangle = |\text{Boson}\rangle \tag{1.35}$$

A SUSY algebra [18] with a single spinor generator Q_α, where α=1 is called the N=1 supersymmetric theory and is the most simplest theory of SUSY. In general, the Lie algebra is commutative and so the only way to extend the standard model to include SUSY which consists of anti-commutative generators is to extend the Lie algebra. This extended Lie algebra goes under the name of Graded Lie algebra. The SUSY algebra is a graded Lie algebra of grade one, namely

$$L = L_0 \oplus L_1 \tag{1.36}$$

where L_0 is the Poincaré algebra and $L_1 = (Q_\alpha, \bar{Q}_{\dot{\beta}})$ where $Q_\alpha, \bar{Q}_{\dot{\beta}}$ is a set of 2 anti-commuting Weyl spinors transforming in the representations $(\frac{1}{2}\,, 0)$ and $(0,\, \frac{1}{2})$ of the Lorentz group, respectively. Haag, Lopuszanski and Sohnius proved that this is the only possible consistent extension of the Poincaré algebra. The generators of L_1 are spinors and hence they transform non-trivially under the Lorentz group. Therefore, SUSY is not an internal symmetry. Rather it is an extension of Poincaré space-time symmetries. Hence, Poincaré algebra is a subset of the SUSY algebra. The SUSY algebra is,

$$\left\{Q_\alpha, \bar{Q}_{\dot{\beta}}\right\} = 2\sigma^{\mu}_{\alpha\dot{\beta}} P_\mu \tag{1.37}$$

$$\{Q_\alpha, Q_\beta\} = \left\{\bar{Q}_{\dot{\alpha}}, \bar{Q}_{\dot{\beta}}\right\} = 0 \tag{1.38}$$

$$\{P_\mu, Q_\alpha\} = \left\{P_\mu, \bar{Q}_{\dot{\alpha}}\right\} = 0 \tag{1.39}$$

$$\{P_\mu, P_\nu\} = 0 \tag{1.40}$$

where P_μ is the generator of translations and σ_μ are Pauli matrices. There are also transformations involving the Lorentz generators $\Lambda^{\alpha\beta}$ given by,

$$[Q_\alpha, M^{\mu\nu}] = (\sigma^{\mu\nu})_\alpha^\beta Q_\beta \tag{1.41}$$

where $M^{\mu\nu}$ is the generator of Lorentz transformations. In addition to these, there is also the commutation relations of the Poincaré algebra. The prime motivation for Supersymmetry is its ability to solve the mass hierarchy problem of the SM. Each particle that couples to the Higgs field has a Yukawa coupling λ_{f}. The coupling with the Higgs field for fermions gives an interaction term $\mathcal{L}_{\text{Yukawa}} = -\lambda_{\text{f}}\bar{\psi}\text{H}\psi$, with ψ being the Dirac Field and H the Higgs Field. Also, the mass of a fermion is proportional to its Yukawa coupling, meaning that the Higgs boson will couple most to the most massive particle. This means that the most significant corrections to the Higgs mass will originate from the heaviest particles, most prominently the top quark. However, suppose there existed two complex scalars (taken to be spin 0) such that:

$$\lambda_S = |\lambda_{\mathrm{f}}|^2 \tag{1.42}$$

Then by the Feynman rules, the correction (from both scalars) is:

$$\Delta\mu_H^2 = 2 \times \frac{\lambda_S}{16\pi^2}[\Lambda_{UV}^2 + ...] \tag{1.43}$$

Combining this contribution with that from the Dirac fermion(eq.(1.34)) brings about the cancellation of the corrections to the Higgs mass.

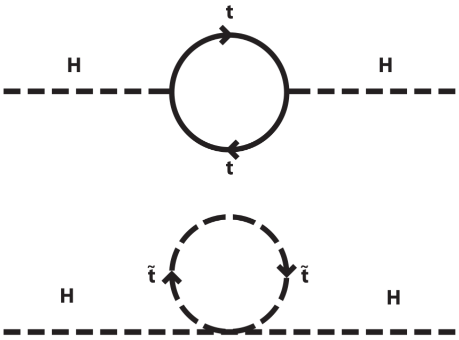

Figure 1.4: Cancellation of the one-loop corrections to Higgs mass squared term between a fermionic top quark loop and scalar stop squark loop

1.2.1 Minimal Supersymmetric Standard Model

The simplest SUSY model which satisfies all the phenomenological constraints is called the Minimal Supersymmetric Standard Model (MSSM). The matter fields are grouped under chiral supermultiplets (left and right-handed components transform differently under a Lorentz transformation) and the gauge fields are grouped under gauge or vector supermultiplets. A supermultiplet is a set of quantum states which can be transformed into one another by one or more supersymmetric transformations. The SM fermion fields with its corresponding Higgs and their super partners (squarks, sleptons and higgsinos) form the chiral supermultiplet, while the SM gauge fields and their super partners (gluinos, winos and bios) form the gauge supermultiplet. Unlike SM, MSSM requires 2 Higgs doublets to guarantee the cancellation of anomalies from the introduction of the higgsino superpartners. Moreover, without a second Higgs doublet, one cannot generate mass for both "up-type" and "down-type" quarks (and charged leptons) in a way consistent with the underlying supersymmetry. $\mathrm{H_u}$ and $\mathrm{H_d}$ form an $\mathrm{SU(2)_L}$ doublet of complex scalar fields with $Y = +\frac{1}{2}$ and $Y = -\frac{1}{2}$ respectively. The weak isospin components of $\mathrm{H_u}$ with $T_3 = (\frac{1}{2}, -\frac{1}{2})$ have electric charges 1, 0 respectively, and are denoted $(\mathrm{H_u^+}, \mathrm{H_u^0})$. Similarly, $(\mathrm{H_d^0}, \mathrm{H_d^-})$ are weak isospin components of the $\mathrm{SU(2)_L}$ doublet $\mathrm{H_d}$ with $T_3 = (\frac{1}{2}, -\frac{1}{2})$. The neutral scalar that corresponds to the physical SM Higgs boson is a linear combination of $\mathrm{H_u^0}$ and $\mathrm{H_d^0}$.

If SUSY was unbroken, then we would have been observed selectrons and squarks with the same mass as the electrons and quarks respectively. The same argument goes for other super partners of the SM particles. This also means that the SUSY particles are relatively heavier than the SM particles. Clearly, therefore, SUSY is a broken symmetry. In the SM, the Electroweak symmetry was broken spontaneously and so it is worth considering a similar method for SUSY as well. But spontaneous symmetry breaking of SUSY involves the introduction of new particles and interactions at very high mass scales in order that the theory be free of any hierarchy problem which is the prime motivation for extending the SM. Moreover, it is not clear how this should be done. However, from a practical point of view, it is extremely useful to simply parametrize our ignorance of these issues by just introducing extra terms that break SUSY explicitly in the effective MSSM Lagrangian. Such terms are said to break SUSY softly, and their couplings are collectively denoted the soft parameters. The part of the Lagrangian which contains these terms is generically called the soft SUSY-breaking Lagrangian L_{soft}, or simply the soft Lagrangian. They are soft in the sense that though they break SUSY they do not reintroduce the hierarchy problem. The

Table 1.3: Chiral Superfields in MSSM

		Spin-0	Spin-$\frac{1}{2}$	Representation under $SU(3)_c \otimes SU(2)_L \otimes U(1)_Y$
squarks and quarks	Q	$(\tilde{u}_L, \tilde{d}_L)$	(u_L, d_L)	(3, 2, $\frac{1}{6}$)
	U	$\tilde{u}^\dagger_R$	$u^\dagger_R$	($\bar{3}$, 1, -$\frac{2}{3}$)
	D	$\tilde{d}^\dagger_R$	$d^\dagger_R$	($\bar{3}$, 1, $\frac{1}{3}$)
sleptons and leptons	L	$(\tilde{\nu}_L, \tilde{e}_L)$	(ν_L, e_L)	(1, 2, -$\frac{1}{2}$)
	E	$\tilde{e}^\dagger_R$	$e^\dagger_R$	(1, 1, 1)
higgs and higgsinos	H_u	(H^+_u, H^0_u)	$(\tilde{H}^+_u, \tilde{H}^0_u)$	(1, 2, $\frac{1}{2}$)
	H_d	(H^+_d, H^0_d)	$(\tilde{H}^+_d, \tilde{H}^0_d)$	(1, 2, -$\frac{1}{2}$)

Table 1.4: Gauge Superfields in MSSM

	Spin-$\frac{1}{2}$	Spin-1	Representation under $SU(3)_c \otimes SU(2)_L \otimes U(1)_Y$
gluinos and gluons	$\tilde{g}$	g	(8, 1, 0)
winos and W-bosons	$\tilde{W}^\pm, \tilde{W}^0$	$W^\pm, W^0$	(1, 3, 0)
bino and B-bosons	$\tilde{B}$	B	(1, 1, 0)

Lagrangian for the MSSM is given by,

$$\mathcal{L}_{\text{MSSM}} = \mathcal{L}_{\text{chiral, free}} + \mathcal{L}_{\text{chiral, int}} + \mathcal{L}_{\text{gauge}} + \mathcal{L}_{\text{Yukawa}} + \mathcal{L}_{\text{soft}} \tag{1.44}$$

where,

$$\mathcal{L}_{\text{chiral, free}} = -\nabla^{\mu}\phi^{*i}\nabla_{\mu}\phi_i + i\psi^{\dagger i}\bar{\sigma}^{\mu}\nabla_{\mu}\psi_i + F^{*i}F_i \tag{1.45}$$

Here, the first 2 terms are the fermion and scalar fields of the chiral supermultiplet and F is a new complex scalar field, which does not have a kinetic term. Such fields are called auxiliary fields, and they are really just book-keeping devices that allow the SUSY algebra to close off-shell.

$$\mathcal{L}_{\text{chiral, int}} = \Big(-\frac{1}{2}W^{ij}\psi_i\psi_j + W^{i}F_i \Big) + c.c \tag{1.46}$$

This part takes care of the interactions between the chiral fields consistent with SUSY. W^{ij} and W^{i} are polynomials of the scalar fields ϕ_i, ϕ^{*i} with,

$$W^{ij} = M^{ij} + y^{ijk}\phi_k \tag{1.47}$$

where M^{ij} is a symmetric mass matrix for the fermion fields, and y^{ijk} is a Yukawa coupling of a scalar ϕ_k and 2 fermions $\psi_i\psi_j$ that is totally anti-symmetric under interchange of i, j, k.

It turns out that,

$$W^{ij} = \frac{\delta^2}{\delta\phi_i\delta\phi_j}W \tag{1.48}$$

where W is the superpotential defined as,

$$W = \frac{1}{2}M^{ij}\phi_i\phi_j + \frac{1}{6}y^{ijk}\phi_i\phi_j\phi_k \tag{1.49}$$

This is not a scalar potential in the ordinary sense. It can be recast in terms of the super fields as,

$$W = Uy_uQH_u - Dy_dQH_d - Ey_eLH_d + \mu H_uH_d \tag{1.50}$$

Here y_u, y_d, y_e are dimensionless Yukawa coupling parameters. The μ in the last term of this potential is the supersymmetric version of the Higgs boson mass of the SM.

$$\mathcal{L}_{\text{gauge}} = -\frac{1}{4}F^a_{\mu\nu}F^{\mu\nu a} + i\lambda^{\dagger a}\bar{\sigma}^\mu\nabla_\mu\lambda^a + \frac{1}{2}D^aD^a \tag{1.51}$$

with,

$$D^a = -g(\phi^*T^a\phi) \tag{1.52}$$

Here $F^a_{\mu\nu}$ is the usual Yang-Mills field strength, λ^a is the gaugino field and D^a is an auxiliary field like F^a. These constitute the gauge field part of the Lagrangian.

$$\mathcal{L}_{\text{Yukawa}} = -\sqrt{2}g(\phi^* T^a \psi)\lambda^a - \sqrt{2}g\lambda^{\dagger a}(\psi^\dagger T^a \phi) + g(\phi^* T^a \psi)D^a \tag{1.53}$$

This part of the Lagrangian consists of the direct coupling of gauginos to matter fields; this can be thought of as the "supersymmetrization" of the usual gauge boson couplings to matter fields. The strength of their interactions are fixed to be gauge couplings by the requirements of supersymmetry, even though they are not gauge interactions from the point of view of an ordinary field theory.

$$\mathcal{L}_{\text{soft}} = -\Big(\frac{1}{2}M_a\lambda^a\lambda^a + \frac{1}{6}a^{ijk}\phi_i\phi_j\phi_k + \frac{1}{2}b^{ij}\phi_i\phi_j\Big) + c.c - (m^2)^i_j\phi^{j*}\phi_i \tag{1.54}$$

This is the generic form of the soft SUSY-breaking Lagrangian. The terms in $\mathcal{L}_{\text{soft}}$ clearly break SUSY, because they involve only scalars and gauginos, consisting of gaugino masses M^a for each gauge group, scalar squared-mass terms $(m^2)^i_j$ and b^{ij}, and (scalar)^3 couplings a^{ijk}. Since F_i and D^a are functions of scalar fields, the complete scalar potential is given by,

$$V = V_F + V_D = F^{*i}F_i + \frac{1}{2}D^aD^a \tag{1.55}$$

In the MSSM, the electroweak symmetry breaking is slightly complicated by the fact that there are two complex Higgs doublets $H_u = (H_u^+,\, H_u^0)$ and $H_d = (H_d^0,\, H_d^-)$ rather than just one in the SM. With the help of eq.(1.55) along with contributions from soft-symmetry breaking terms, the classical scalar potential for the Higgs scalar fields in the MSSM is given by,

$$
\begin{aligned}
V = {} & (|\mu|^2+m_{H_u}^2)(|H_u^0|^2+|H_u^+|^2) + (|\mu|^2+m_{H_d}^2)(|H_d^0|^2+|H_d^-|^2) \\
& + [b(H_u^+H_d^- - H_u^0H_d^0) + c.c] \\
& + \frac{1}{8}(g^2+g^{'2})(|H_u^0|^2+|H_u^+|^2-|H_d^0|^2-|H_d^-|^2)^2 + \frac{1}{2}g^2|H_u^+H_d^{0*} + H_u^0H_d^{-*}|^2
\end{aligned}
\tag{1.56}
$$

The terms proportional to $|\mu|^2$ come from F-terms, the terms proportional to g^2 and $g^{'2}$ are the D-term contributions and the rest are contributions from the soft-symmetry breaking potential. We can use the freedom to make gauge transformations to simplify the determination of the minimum of this potential. First, the freedom to make $SU(2)_L$ gauge transformations allows us to rotate away a possible VEV for one of the weak isospin components of one of the scalar fields, so without loss of generality we can take $H_u^+ = 0$ at the minimum of the potential. Then one can check that a minimum of the potential satisfying $\frac{\partial V}{\partial H_u^+} = 0$ must also have $H_d^- = 0$. This is good, because it means that at the minimum of the potential electromagnetism is necessarily unbroken, since the charged components of the Higgs scalars cannot get VEV's. After setting $H_u^+ = H_d^- = 0$, we are left to consider the scalar potential,

$$
\begin{aligned}
V = (|\mu|^2+m_{H_u}^2)|H_u^0|^2+(|\mu|^2+m_{H_d}^2)|H_d^0|^2+[-H_u^0H_d^0 + c.c] - (bH_u^0H_d^0 + c.c) \\
+\frac{1}{8}(g^2+g^{'2})(|H_u^0|^2-|H_d^0|^2)^2
\end{aligned}
\tag{1.57}
$$

In order for the MSSM scalar potential to be viable, the potential is bounded from below for arbitrarily large values of the scalar fields, so that V will really have a minimum. In purely supersymmetric theories, the scalar potentials are automatically non-negative and so clearly bounded from below. But, now that we have introduced SUSY breaking terms, it does not hold any more and so we have to be impose such a condition on the potential. Moreover, the b-term always favors electroweak symmetry breaking. Requiring that one linear combination of H_u^0 and H_d^0 has a negative squared mass near $H_u^0 = H_d^0 = 0$ amounts to the following conditions,

$$2b < 2|\mu|^2 + m_{H_u}^2 + m_{H_d}^2 \tag{1.58}$$

$$b^2 > (|\mu|^2 + m_{H_u}^2)(|\mu|^2 + m_{H_d}^2) \tag{1.59}$$

If this inequality is not satisfied, then $H_u^0 = H_d^0 = 0$ will be a stable minimum of the potential (or there will be no stable minimum at all), and electroweak symmetry breaking will not occur. Note that although a negative value for $|\mu|^2 + m_{H_u}^2$ will help eq. (1.59) to be satisfied, it is not strictly necessary. Furthermore, even if $m_{H_u}^2 < 0$, there may be no electroweak symmetry breaking if $|\mu|$ is too large or if b is too small. These two are essentially the conditions necessary for H_u^0 and H_d^0 to have non-zero VEV's. Let us write,

$$v_u = \langle H_u^0 \rangle, \quad v_d = \langle H_d^0 \rangle \tag{1.60}$$

These VEV's are related to the known mass of the Z boson and the electroweak gauge couplings:

$$v_u^2 + v_d^2 = v^2 = \frac{2m_Z^2}{(g^2 + g'^2)} \approx (174 \text{ GeV})^2 \tag{1.61}$$

The ratio of the VEVs is traditionally written as,

$$\tan\beta \equiv \frac{v_u}{v_d} \tag{1.62}$$

The value of tan β is not fixed by present experiments, but it depends on the Lagrangian parameters of the MSSM in a calculable way. Since v_u = v sin β and v_d = v cos β were taken to be real and positive by convention, we have $0 < \beta < \frac{\pi}{2}$. Now one can write down the conditions $\frac{\partial V}{\partial H_u^0} = \frac{\partial V}{\partial H_d^0} = 0$ under which the potential eq. (1.57) will have a minimum satisfying eqs. (1.61) and (1.62):

$$m_{H_u}^2 + |\mu|^2 - b \cot \beta - \left(\frac{m_Z^2}{2}\right) \cos(2\beta) = 0 \tag{1.63}$$

$$m_{H_d}^2 + |\mu|^2 - b \tan \beta + \left(\frac{m_Z^2}{2}\right) \cos(2\beta) = 0 \tag{1.64}$$

Taking $|\mu|^2$, b, $m_{H_u}^2$ and $m_{H_d}^2$ as input parameters, and m_Z^2 and tan β as output parameters obtained by solving these two equations, one obtains:

$$sin(2\beta) = \frac{2b}{m_{H_u}^2 + m_{H_d}^2 + |\mu|^2} \tag{1.65}$$

$$m_Z^2 = \frac{\left|m_{H_d}^2 - m_{H_u}^2\right|}{\sqrt{1 - \sin^2(2\beta)}} - m_{H_u}^2 - m_{H_d}^2 - 2|\mu|^2 \tag{1.66}$$

Without miraculous cancellations, all of the input parameters ought to be within an order of magnitude or two of m_Z^2. This is the famous μ-problem in the MSSM and is the biggest motivation for the Next to Minimal Supersymmetric Standard Model. The other motivations for considering extensions of the MSSM include:

- The Higgs sector is highly restricted in the MSSM. The lower bounds on the Higgs-boson masses from LEP measurements require large quantum corrections accompanied by a large stop mass in this model. An extended Higgs sector may relax this restrictions and thus circumvent the lower experimental bounds.

- The MSSM Higgs-boson sector is CP-conserving at tree level. Extending the Higgs sector in an appropriate way, CP violating phases arise. Sufficient CP-violation would meet one of the necessary Sakharov criteria in order to generate the baryon-antibaryon asymmetry in our Universe.

- The baryon-antibaryon asymmetry may be generated by strong electroweak phase transitions of first order. The required cubic terms in the effective potential arise in the SM and the MSSM only via generically small radiative corrections. An explicit cubic term is possible in extensions of the MSSM.

1.2.1.1 Higgs Sector in MSSM

The Higgs sector of the MSSM consists of two $\mathrm{SU(2)_L}$ doublets. Assuming a CP-conserving Higgs Sector, after electroweak symmetry breaking (EWSB), there are five physical states left in the spectrum - two CP-even states h^0 and H^0 with $m_{\mathrm{h}^0} < m_{\mathrm{H}^0}$, one CP-odd state A^0, and two charged scalar states $\mathrm{H}^{\pm}$. At tree-level, it is customary to use the mass m_{A} and the ratio of the vacuum expectation values $\tan\beta = \frac{v_u}{v_d}$ as the free parameters to determine the other masses. These masses receive large radiative corrections from the top-stop sector due to the large top Yukawa coupling. If we categorize these Higgs bosons according to their couplings to the electroweak gauge bosons, there are two distinct regions in the MSSM:

1. The "decoupling region": For a relatively heavy $\mathrm{A}^0 (m_{\mathrm{A}} \geq 300$ GeV), the lighter CP-even state h^0 is the SM-like Higgs and the others H^0, A^0 and $\mathrm{H}^{\pm}$ are heavy and nearly

degenerate.

2. The “non-decoupling region”: For $m_{\rm A} \approx m_{\rm Z}$, the heavier CP-even Higgs $\rm H^0$ is the SM-like Higgs, while $\rm h^0$ and $\rm A^0$ are light and nearly degenerate. The mass of the charged Higgs $\rm H^{\pm}$ is typically around 140 GeV.

The decoupling scenario comfortably accommodates the current searches due to the effective absence of the non-SM-like Higgs states. In fact, it would be very difficult to observe any of the heavy MSSM Higgs bosons at the LHC if $m_{\rm A} \geq 400$ GeV for a modest value of tan $\beta \leq 10$. The non-decoupling scenario, on the other hand, would lead to a rich LHC phenomenology due to the existence of multiple light Higgs bosons. Although this latter scenario would be more tightly constrained by current experiments, it would correspondingly have greater predictive power for its phenomenology.

1.2.2 Next to Minimal Supersymmetric Standard Model

In the NMSSM an additional gauge singlet is introduced which generates the ţ-term dynamically, that is, an effective μ-term arises spontaneously and the adjustment by hand drops out. This is the main motivation for the NMSSM and the price to pay, is the introduction of an additional gauge-singlet superfield. The particle content in the bosonic part of the singlet results in two additional Higgs bosons whereas in the fermionic part we have one additional neutralino, called singlino. Altogether we have seven Higgs bosons and five neutralinos in the NMSSM, compared to five Higgs bosons and four neutralinos in the MSSM. The gauge field sector is the same as in the MSSM. The Lagrangian for NMSSM is same as for MSSM except for the soft symmetry breaking sector which has the generic

Table 1.5: Chiral Superfields in NMSSM

		Spin-0	Spin-$\frac{1}{2}$	Representation under $SU(3)_c \otimes SU(2)_L \otimes U(1)_Y$
squarks and quarks	Q	$(\tilde{u}_L, \tilde{d}_L)$	(u_L, d_L)	(3, 2, $\frac{1}{6}$)
	U	$\tilde{u}_R^\dagger$	$u_R^\dagger$	($\bar{3}$, 1, -$\frac{2}{3}$)
	D	$\tilde{d}_R^\dagger$	$d_R^\dagger$	($\bar{3}$, 1, $\frac{1}{3}$)
sleptons and leptons	L	$(\tilde{\nu}_L, \tilde{e}_L)$	(ν_L, e_L)	(1, 2, -$\frac{1}{2}$)
	E	$\tilde{e}_R^\dagger$	$e_R^\dagger$	(1, 1, 1)
higgs and higgsinos	H_u	(H_u^+, H_u^0)	$(\tilde{H}_u^+, \tilde{H}_u^0)$	(1, 2, $\frac{1}{2}$)
	H_d	(H_d^+, H_d^0)	$(\tilde{H}_d^+, \tilde{H}_d^0)$	(1, 2, -$\frac{1}{2}$)
	$\hat{S}$	S	$\tilde{S}$	(1, 1, 0)

form,

$$\mathcal{L}_{\text{soft}}^{\text{NMSSM}} = \mathcal{L}_{\text{soft}}^{\text{MSSM}} - (\lambda A_\lambda \hat{S} H_u H_d + \frac{1}{3}\kappa A_\kappa \hat{S}^3 + c.c) - m_S^2 |\hat{S}|^2 \tag{1.67}$$

The super potential for the NMSSM gets some extra terms as well due to to the additional singlet field ($\hat{S}$) and is given by,

$$V_{\text{NMSSM}} = V_{\text{MSSM}}\Big|_{\mu=0} + \lambda \hat{S} H_u H_d + \frac{1}{3}\kappa \hat{S}^3 \tag{1.68}$$

The last 2 terms replace the μ-term of the MSSM. Even though it is not explicitly included, it arises from spontaneously symmetry breaking with $\mu = \lambda \langle S \rangle \equiv \lambda v_s$. The six parameters λ, κ, A_λ, A_κ, μ and tan β then determine the tree-level Higgs spectrum after minimizing the scalar potential and solving for the SUSY-breaking Higgs masses.

1.2.2.1 Higgs Sector in NMSSM

In the NMSSM, as a result of the addition of a complex $\mathrm{SU(2)_L \otimes U(1)_Y}$ singlet scalar field, after the scalar fields acquire VEV's, one new CP-even and one new CP-odd state are added to the MSSM spectrum, resulting in three CP-even scalar mass eigenstates (denoted by $\mathrm{H_1, H_2, H_3}$), two CP-odd pseudo-scalar mass eigenstates $(\mathrm{A_1, A_2})$, with $m_{\mathrm{H_1}} \leq m_{\mathrm{H_2}} \leq m_{\mathrm{H_3}}$ and $m_{\mathrm{A_1}} \leq m_{\mathrm{A_2}}$ (for a CP-conserving Higgs Sector) plus a pair of charged states $(\mathrm{H^\pm})$.

Chapter 2

The LHC and the CMS Detector

2.1 Large Hadron Collider

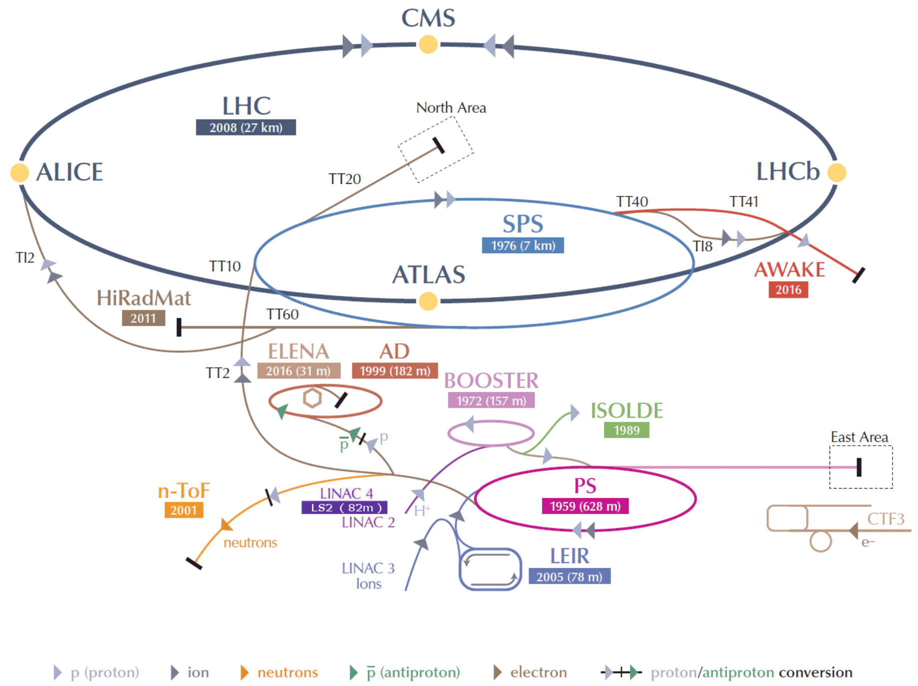

Figure 2.1: Large Hadron Collider

The Large Hadron Collider (LHC) [19–21] is the world's largest and most powerful particle accelerator. It is a two-ring, superconducting accelerator and collider installed in the 27 km long LEP tunnel with a number of accelerating structures to boost the energy of the particles along the way to a maximum energy of 7 TeV (post LS-1 upgrade). Inside the accelerator, two high-energy particle beams travel at close to the speed of light before they are made to collide. The beams travel in opposite directions in separate beam pipes - two tubes kept at ultrahigh vacuum. They are guided around the accelerator ring by a strong magnetic field maintained by superconducting electromagnets. The electromagnets are built from coils of special electric cable that operates in a superconducting state, efficiently conducting electricity without resistance or loss of energy. This requires chilling the magnets to -271.3°C - a temperature colder than outer space. For this reason, much of the accelerator is connected to a distribution system of liquid helium, which cools the magnets, as well as to other supply services. Thousands of magnets of different varieties and sizes are used to direct the beams around the accelerator. These include 1232 dipole magnets 15 meters in length which bend the beams, and 392 quadrupole magnets, each 5-7 meters long, which focus the beams. Just prior to collision, another type of magnet is used to "squeeze" the particles closer together to increase the chances of collisions. The particles are so tiny that the task of making them collide is akin to firing two needles 10 kilometers apart with such precision that they meet halfway.

The quantity that measures the ability of a particle accelerator to produce the required number of interactions is called the luminosity(L) and is the proportionality factor between the number of events per second $\frac{dR}{dt}$ and the cross section σ_{event} is given by:

$$\frac{dR}{dt} = L\sigma_{\text{event}} \tag{2.1}$$

The machine luminosity depends only on the beam parameters and can be written for a Gaussian beam distribution as:

$$L = \frac{N_b^2 n_b f_{rev} \gamma_r}{4\pi \epsilon_n \beta^*} F \tag{2.2}$$

where N_b is the number of particles per bunch, n_b is the number of bunches per beam, f_{rev} is the revolution frequency of the beam, γ_r is the relativistic gamma factor, ϵ_n is the normalized transverse beam emittance, β^* is the beta function at the collision point and F is the geometric luminosity reduction factor due to the crossing angle at the Interaction Point (IP) defined as:

$$F = \frac{1}{\sqrt{1 + \left(\frac{\theta_c \sigma_z}{2\sigma^*}\right)^2}} \tag{2.3}$$

where θ_c is the full crossing angle at the IP, σ_z is the Root Mean Square (RMS) bunch length and σ^* is the transverse RMS beam size at the IP (The above expression assumes equal beam parameters for both circulating beams).

The integrated Luminosity ($\mathcal{L}_{\text{integrated}}$) is the integral of the instantaneous Luminosity as a function of the time given by,

$$\mathcal{L}_{\text{integrated}} = \int L(t)dt \tag{2.4}$$

It is generally measured in units of fb^{-1}.

Table 2.1: Comparison of LHC design beam parameters with 2012 and 2015 data

	Units	**Design**	**2012**	**2015**
Proton energy	[TeV]	7	4	6.5
Number of particles per bunch		1.15×10^{11}	1.7×10^{11}	1.2×10^{11}
Number of bunches		2808	1368	2244
Bunch spacing	[ns]	25	50	25
Average pile-up		25	35	15
Transverse normalized emittance	[μm rad]	3.75	2.5	2.5
Circulating beam current	[A]	0.58	0.42	0.49
Stored energy per beam	[MJ]	362	149	280
RMS bunch length	[cm]	7.55	9	7.55
Full Crossing angle at IP5	[μrad]	285	290	290
RMS beam size at IP5	[μm]	16.7	18.8	17
Geometric Luminosity reduction factor at IP5		0.84	0.82	0.84
Peak Luminosity at IP5	[$\mathrm{cm}^{-2}\mathrm{sec}^{-1}$]	1.0×10^{34}	0.77×10^{34}	0.5×10^{34}

2.1.1 Beam injection chain

The protons from the time they are produced by a source, go through a chain of smaller accelerators before entering the LHC tunnel.

2.1.1.1 Linear Accelerator 2

Linear accelerator 2 (Linac 2) is the starting point for the protons used in experiments at CERN. Linear accelerators use radiofrequency cavities to charge cylindrical conductors. The protons pass through the conductors, which are alternately charged positive or negative. The conductors behind them push the particles and the conductors ahead of them pull, causing the particles to accelerate. Small quadrupole magnets ensure that the protons remain in a tight beam. The proton source is a bottle of hydrogen gas at one end of Linac 2. The hydrogen is passed through an electric field to strip off its electrons, leaving only protons to enter the accelerator. By the time they reach the other end, the protons have reached the energy of 50 MeV and gained 5% in mass. They then enter the Proton Synchrotron Booster (PSB), the next step in CERN's accelerator chain, which takes them to a higher energy. The proton beams are pulsed from the hydrogen bottle for up to 100 microseconds per pulse. The pulses are repeated again and again until enough protons are produced.

2.1.1.2 Proton Synchrotron Booster

The Proton Synchrotron Booster (PSB) is made up of four superimposed synchrotron rings that receive beams of protons from the Linac 2 at 50 MeV and accelerate them to 1.4 GeV for injection into the Proton Synchrotron (PS).

2.1.1.3 Proton Synchrotron

The Proton Synchrotron (PS) is a key component in CERN's accelerator complex, where it usually accelerates either protons delivered by the Proton Synchrotron Booster or heavy ions from the Low Energy Ion Ring (LEIR). With a circumference of 628 meters, the PS has 277 conventional (room-temperature) electromagnets, including 100 dipoles to bend the beams round the ring. The accelerator operates at up to 25 GeV.

2.1.1.4 Super Proton Synchrotron

The Super Proton Synchrotron (SPS) is the second-largest machine in CERN's accelerator complex. Measuring nearly 7 kilometres in circumference, it takes particles from the Proton Synchrotron and accelerates them to provide beams for the Large Hadron Collider, the NA61/SHINE and NA62 experiments, the COMPASS experiment and the CNGS project. The SPS operates at up to 450 GeV. It has 1317 conventional (room-temperature) electromagnets, including 744 dipoles to bend the beams round the ring.

2.1.2 LHC Collider system

The Large Hadron Collider (LHC) is currently operating at the energy of 6.5 TeV per beam. At this energy, trillions of protons circle the collider's 27-kilometre tunnel 11,245 times per second. After injecting the beam into the LHC tunnel from the SPS, more than 50 types of magnets are needed to send them along complex paths without their losing speed. All the magnets on the LHC are electromagnets. The main dipoles generate powerful 8.4 Tesla magnetic fields - more than 100,000 times more powerful than the Earth's magnetic field. The electromagnets use a current of 11,850 amperes to produce the field, and a superconducting coil allows the high currents to flow without losing any energy to electrical resistance.

2.1.2.1 Lattice magnets

Thousands of "lattice magnets" on the LHC bend and tighten the particle's trajectory. They are responsible for keeping the beams stable and precisely aligned. Dipole magnets, one of the most complex parts of the LHC, are used to bend the paths of the particles. There are 1232 main dipoles, each 15 metres long and weighing in at 35 tonnes. If normal magnets were used in the 27 km-long LHC instead of superconducting magnets, the accelerator would have to be 120 kilometres long to reach the same energy. Powerful magnetic fields generated by the dipole magnets allow the beam to handle tighter turns. When particles are bunched together, they are more likely to collide in greater numbers when they reach the LHC detectors. Quadrupoles help to keep the particles in a tight beam. They have four magnetic poles arranged symmetrically around the beam pipe to squeeze the beam either vertically or horizontally. Dipoles are also equipped with sextupole, octupole and decapole magnets, which correct for small imperfections in the magnetic field at the extremities of the dipoles.

2.1.2.2 Insertion magnets

When the particle beams enter the detectors, insertion magnets take over. Particles must be squeezed closer together before they enter a detector so that they collide with particles coming from the opposite direction. Three quadrupoles are used to create a system called an inner triplet. There are eight inner triplets, two of which are located at each of the four large LHC detectors, ALICE, ATLAS, CMS and LHCb. Inner triplets tighten the beam, making it 12.5 times narrower - from 0.2 millimetres down to 16 micrometres across. After the beams collide in the detector, enormous magnets aid the measurement of particles. For example, physicists look at how charged particles bend in the magnetic field to determine their identity. Charged particles are deflected by the magnetic field in the detector, and their momentum can be calculated from the amount of deflection. After colliding, the particle beams are separated again by dipole magnets. Other magnets minimize the spread of the particles from the collisions. When it is time to dispose of the particles, they are deflected from the LHC along a straight line towards the beam dump. A “dilution” magnet reduces the beam intensity by a factor of 100,000 before the beam collides with a block of concrete and graphite composite for its final stop. Insertion magnets are also responsible for beam cleaning, which ensures that stray particles do not come in contact with the LHC’s most sensitive components.

2.1.2.3 Cryogenics

All of the magnets on the LHC are superconducting electromagnets. The LHC’s main magnets operate at a temperature of 1.9 K (-271.3^{o}C), colder than the 2.7 K (-270.5^{o}C) of outer space. Magnets produce a magnetic field of 8.33 Tesla to keep particle beams on course around the LHC’s 27-kilometre ring. Superconductivity could not happen without the use of cryogenic systems. The coil’s niobium-titanium (NbTi) wires must be kept at low temperatures to reach a superconducting state. The LHC’s superconducting magnets are therefore maintained at 1.9 K (-271.3^{o}C) by a closed liquid-helium circuit. At atmospheric pressure gaseous helium becomes liquid at around 4.2 K (-269.0^{o}C). However, if cooled below 2.17 K (-271.0^{o}C), it passes from the fluid to the superfluid state. Superfluid helium has remarkable properties, including very high thermal conductivity; it is an efficient heat conductor. These qualities make helium an excellent refrigerant for cooling and stabilising the LHC’s large-scale superconducting systems.

2.1.2.4 Vacuum

The vacuum pressure is about 10^{-7} Pa in the beam pipe at cryogenic temperature (5 K) because we want to avoid collisions with gas molecules, and lower than 10^{-9} Pa close to Interaction Points, because this is the part where collisions take place.

2.2 Compact Muon Solenoid Detector

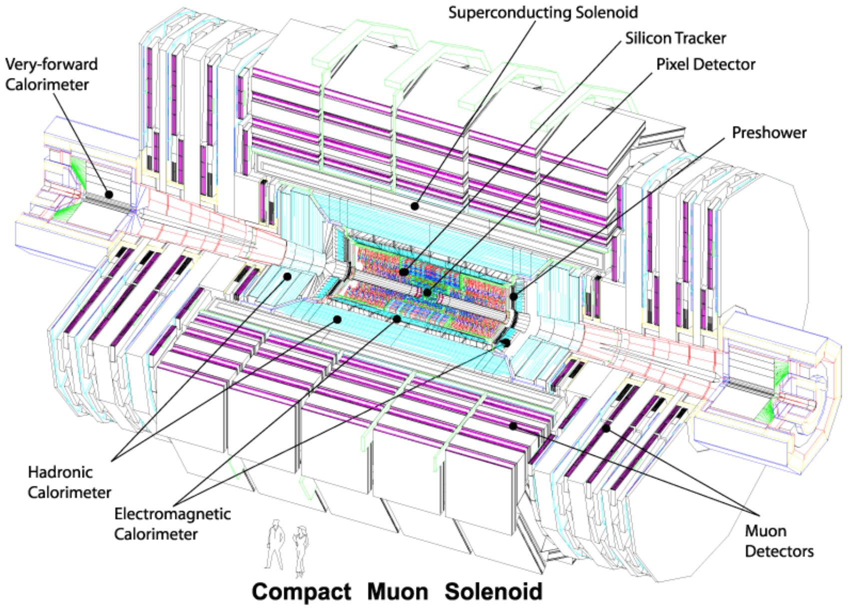

Figure 2.2: CMS Detector

The Compact Muon Solenoid (CMS) detector is one of the two high luminosity experiments located at CERN. It is 21 m long, 15 m wide and 15 m high consisting of several subsystems which are designed to measure the energy and momentum of photons, electrons, muons, and other products in proton-proton collisions. The detector is built around a huge solenoid magnet which takes the form of a cylindrical coil of superconducting cable, cooled to -268.5°C, that generates a magnetic field of 4 Tesla. The following coordinate conventions are followed in the CMS:

- The coordinate system adopted by CMS has the origin centered at the nominal collision point inside the experiment, the y-axis pointing vertically upward, the x-axis pointing radially inward toward the center of the LHC and so the z-axis points along the beam direction.
- The azimuthal angle ϕ is measured from the x-axis in the $x - y$ plane.
- The polar angle θ is measured from the z-axis.

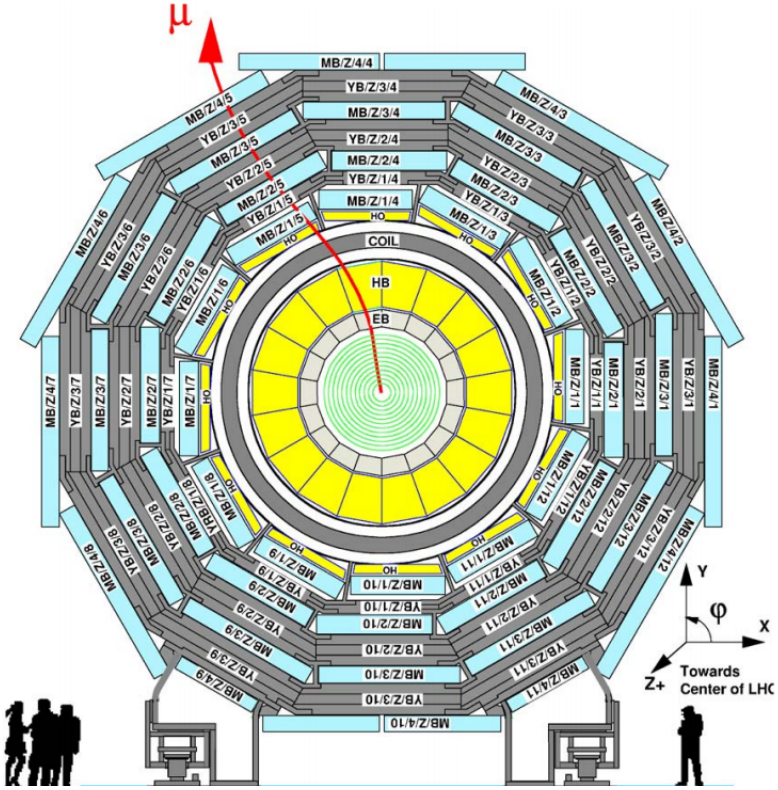

Figure 2.3: CMS coordinate axes

- The pseudorapidity is defined as $\eta = -\ln \tan(\theta/2)$.

- The momentum and energy measured transverse to the beam direction, denoted by p_T and E_T, respectively, are computed from the x and y components. The imbalance of energy measured in the transverse plane is denoted by E_T^{miss}.

The stringent requirements that had to be satisfied by the CMS detector so as to achieve the goals of the LHC physics program are as follows:

- Good muon identification and momentum resolution over a wide range of momenta in the region $|\eta| < 2.5$, good dimuon mass resolution ($\approx 1\%$ at 100 GeV), and the ability to determine unambiguously the charge of muons with $p < 1$ TeV.

- Good charged particle momentum resolution and reconstruction efficiency in the inner tracker. Efficient triggering and offline tagging of τ and b-jets, requiring pixel detectors close to the interaction region.

- Good electromagnetic energy resolution, good diphoton and dielectron mass resolution ($\approx 1\%$ at 100 GeV), wide geometric coverage ($|\eta| < 2.5$), measurement of the direction of photons and/or correct localization of the primary interaction vertex, π^0 rejection and efficient photon and lepton isolation at high luminosities.

- Good E_T^{miss} and dijet mass resolution, requiring hadron calorimeters with a large hermetic geometric coverage ($|\eta| < 5$) and with fine lateral segmentation ($\Delta\eta \times \Delta\phi < 0.1 \times 0.1$).

The CMS detector consists of the following subsystems:

1. The Muon System comprising of the Drift tube chamber (DT), Resistive Plate Chambers (RPC) and the Cathode Strip Chambers (CSC).
2. Calorimeter comprising of the Electromagnetic Calorimeter (ECAL) and the Hadronic Calorimeter (HCAL).
3. Inner Tracking system comprising the Strip tracker and the Pixel tracker.

2.2.1 Muon System

The muon system uses three types of gaseous detectors to detect and measure the muons; DTs in the barrel region, CSCs in the endcap region, and RPCs in both the barrel and endcap. They are positioned in the CMS detector based on the environment they operate in. In the barrel region ($|\eta|<1.2$), where the neutron induced background is small,the muon rate is low and the residual magnetic field in the chambers is low, DTs are used. In the 2 endcaps, where the muon rate as well as the neutron induced background rate is high, and the magnetic field is also high, CSCs are deployed and cover the region upto $|\eta|<2.4$. In addition to this, RPCs are used both in the barrel and the endcap regions covering $|\eta| < 0.9$ and $0.9 < |\eta| < 2.4$ (includes the overlap region $0.9 < |\eta| < 1.2$) respectively. RPCs provide a fast response with good time resolution but with a coarser spatial resolution than the DTs or CSCs and therefore can identify the correct bunch-crossing unambiguously.

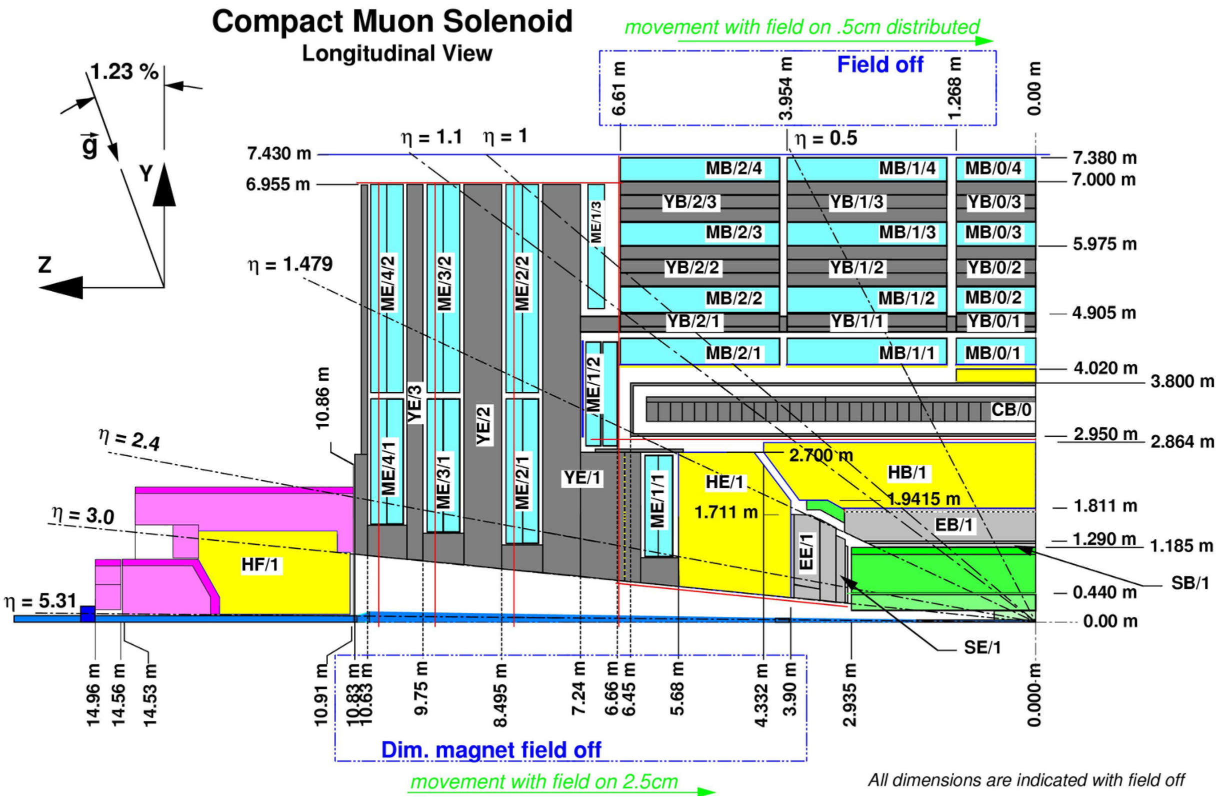

Figure 2.4: Muon System in the CMS detector

2.2.1.1 Cathode Strip Chambers

The CSC is a multiwire proportional chamber. The gas ionization and subsequent electron avalanche caused by a charged particle traversing each plane of a chamber produces a charge on the anode wire and an image charge on a group of cathode strips. The signal on the wires is fast and is used in the Level-1 Trigger. However, it leads to a coarser position resolution. A precise position measurement is made by determining the centre-of-gravity of the charged distribution induced on the cathode strips.

There are 540 CSCs of trapezoidal shape in the endcap placed between the iron disks, which return the magnetic flux of the central solenoid and also shield the chambers.

The chambers are arranged to form four disks, called stations (ME1, ME2, ME3, ME4). The ME1 has three rings of chambers (ME1/1, ME1/2, ME1/3), while the other three stations are composed from two rings of chambers (MEn/1 and MEn/2). All but the ME1/3 chambers overlap in ϕ and therefore form rings seamless in azimuth. There are 18 or 36 chambers in every ring. The gas mixture used is 40% Argon, 50% CO2 and 10% CF4. Argon is the ionizing gas, CO2 is a quencher and CF4 prevents aging in wires. Every chamber contains six detecting layers each composed of an anode wire plane stretched between two planar copper cathodes, one continuous, the other segmented in strips to provide position measurement. The wires are read out in groups while the strips are read out individually. The high voltage is supplied to ranges of wire groups, depending on the size of the chamber; the largest chambers have five such high-voltage segments. The strips in alternating layers are staggered, except in ME1/1. The strips in the ME1/1 chambers are cut along a line parallel to the short sides of the trapezoid in order to reduce the rate on any one strip being closer to the IP. The strips closer to the beam line constitute ME1/1a , and the others, ME1/1b. The CSCs are designed to measure the azimuthal oordinates (ϕ) of muon tracks well, as the bending of the muon trajectories in the magnetic flux returned through the steel disks is mainly about the direction of a unit vector pointing away from the beam line. The strips describe constant ϕ values. High precision is achieved by exploiting the shape of the charge distribution on three consecutive strips; this allows an adequate measurement of the muon momentum as needed for triggering purposes. The anode wires run perpendicular to the central strip, and hence parallel to the two parallel sides of the chamber; they provide an approximate measure of the radial coordinate. Each CSC measures up to 6 space coordinates (r,ϕ,z), one from each of the six planes. The spatial resolution provided by each chamber from the strips is typically about 200 μm (100 μm for ME1/1).The angular resolution in ϕ is of order 10 mrad.

ME1/1 chambers have to operate in an axial magnetic field in excess of 3 Tesla, while ME1/2 chambers are in a highly non-uniform magnetic field of up to 1 Tesla. The other chambers are generally in much lower magnetic fields. Most muons initially bend through the magnetic field and reach their maximum sagitta slightly in front of the first station. After this the muons are moving through the return flux and the sign of the bending is reversed. Consequently the sagitta measurement in the succeeding stations will be smaller. Therefore, the sagitta measurement at the first station is crucial and leads to more stringent requirements on the resolution and alignment in this station than in the other stations. Some other advantages of CSCs are:

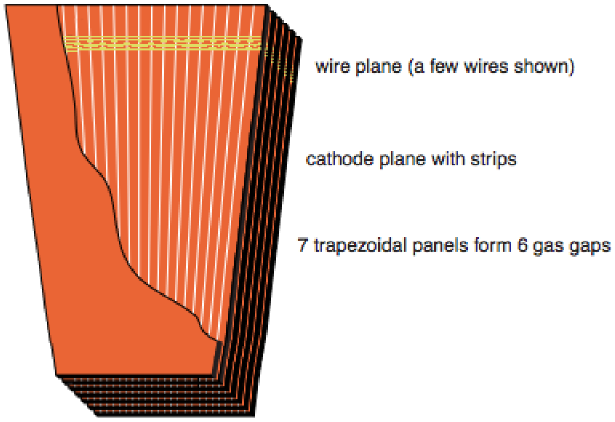

Figure 2.5: Cathode Strip Chamber

- Their intrinsic spatial resolution, being basically defined by signal-to-noise ratio, can be as good as 50 μm.

- CSCs can operate in large and non-uniform magnetic field without significant deterioration in their performance.

- Gas mixture composition, temperature, and pressure do not directly affect CSC precision and thus stringent control of these variables is not required.

- Detector mechanical precision is defined by strips which can be etched or milled with the required accuracy and can be easily extended outside the gas volume, thus making survey of plane-to-plane alignment very simple.

2.2.1.2 Resistive Plate Chambers

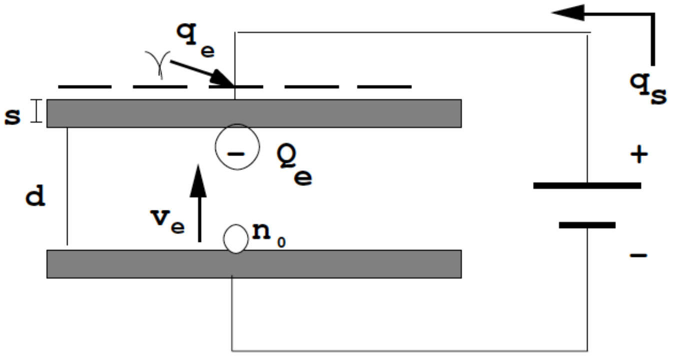

Figure 2.6: Model of the charge formation in the RPC gap

RPCs consist of two parallel plates, a positively-charged anode and a negatively-charged cathode, both made of a very high resistivity plastic material and separated by a gas volume. When a muon passes through the chamber, electrons are knocked out of gas atoms. These electrons in turn hit other atoms causing an avalanche of electrons. The electrodes are transparent to the signal (the electrons), which are instead picked up by external metallic strips after a small but precise time delay. The pattern of hit strips gives a quick measure of the muon momentum, which is then used by the trigger to make immediate decisions about whether the data are worth keeping. RPCs provide a reasonable level of spatial resolution with excellent time resolution, comparable to that of scintillators.

In the muon system, these chambers cover roughly the same area as the DTs and CSCs but provide a faster timing signal and have a different sensitivity to background. Trigger signals coming from the drift tubes, cathode strip chambers, and the RPCs proceed in parallel until reaching the level of the global trigger logic. This provides redundancy for evaluating efficiencies, and result in a higher efficiency and greater rate capability. RPCs constitute a fast dedicated trigger which can identify candidate muon tracks and assign the bunch crossing with high efficiency. Since they are low-cost devices, they are highly segmented to make it possible to measure the transverse momentum at trigger time.

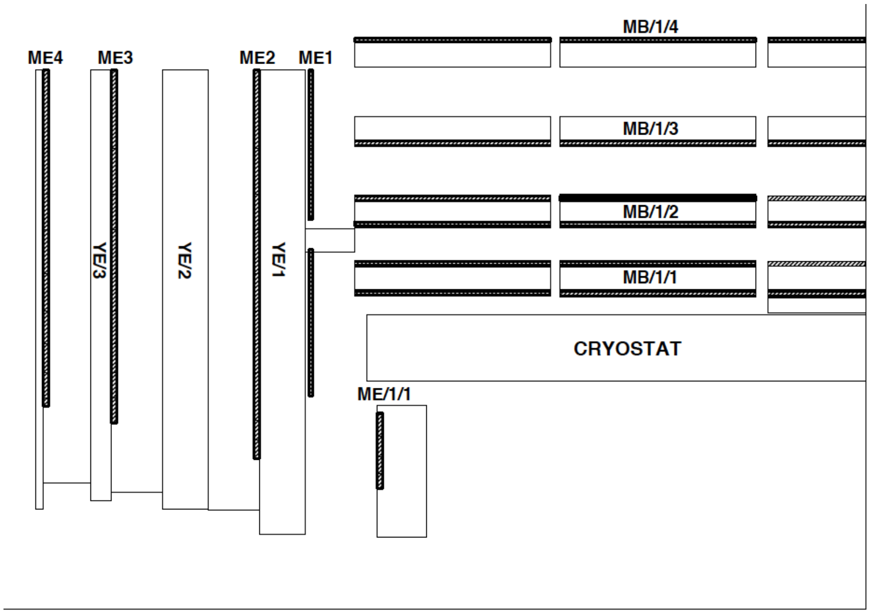

Figure 2.7: RPCs in barrel and endcap

A total of six layers of RPCs are mounted with the barrel chambers, two layers with each of stations MB1 and MB2, and one each in the outer stations MB3 and MB4. The redundancy in the first two stations allows the trigger algorithm to perform the reconstruction always on the basis of four layers, even for low p_T tracks, which may be stopped inside the detector. In the endcap region, each of the four layers of CSCs have a layer of RPCs in conjunction with it, with their shape and method of mounting determined by the η segmentation. The RPCs extend to η=2.1.

2.2.1.3 Drift Tube Chambers

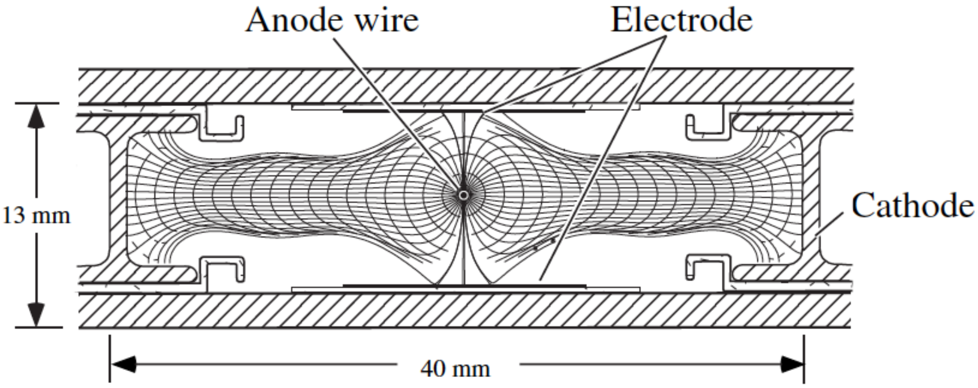

Figure 2.8: Transverse view of the Drift cell

The choice of a drift chamber as tracking detector in the barrel was dictated by the low expected rate and by the relatively low intensity of the local magnetic field. When a muon or any charged particle passes through the volume it knocks electrons off the atoms of the gas. These follow the electric field ending up at the positively-charged wire. By registering where along the wire electrons hit as well as by calculating the muon's original distance away from the wire, DTs give two coordinates for the muon's position. Each DT chamber, on average 2m x 2.5m in size, consists of 12 aluminum layers, arranged in three groups of four, each up with up to 60 tubes: the middle group measures the coordinate along the direction parallel to the beam and the two outside groups measure the perpendicular coordinate.The CMS barrel muon detector is made of four stations forming concentric cylinders around the beam line: three of them consist of 60 drift chambers each, the fourth, the most outer, of 70.

A group of three consecutive layers of thin tubes, staggered by half a tube, provides excellent time-tagging capability. A time resolution of a few nanoseconds can be obtained using signal processing based on simple mean-timer circuits, which in the case of LHC makes it possible to have efficient local standalone bunch crossing identification. In addition, the efficiency to reconstruct a high p_T muon track with a momentum measurement delivered by the barrel muon system alone is better than 95% in the rapidity range covered by 4 stations, i.e. $|\eta| < 0.8$.

The cell design makes use of four electrodes to shape an effective drift field: two on the side walls of the tube, and two above and below the wires on the ground planes between the layers. With this arrangement the requirement of 250 micron resolution per layer (which guarantees 100 microns per chamber) can be obtained while operating the tubes at atmospheric pressure with a binary Ar/CO_2 gas mixture. The multi-electrode design ensures this performance even in the presence of the unavoidable stray magnetic fields present in the chamber region.

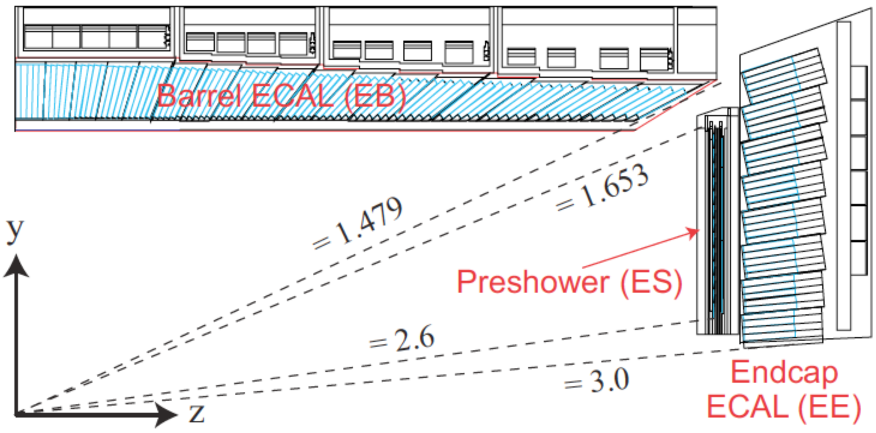

Figure 2.9: Transverse section through the ECAL

2.2.2 Electromagnetic Calorimeter

The ECAL is used primarily for measuring the energy and momentum of electrons and photons. The active material in the ECAL is lead tungstate ($PbWO_4$). When electrons and photons pass through the lead tungstate crystal, it scintillates and intensity of the light produced is proportional to the particle's energy. These high-density crystals produce light in fast, short, well-defined photon bursts that allow for a precise, fast and fairly compact detector. Photodetectors that have been especially designed to work within the high magnetic field, are also glued onto the back of each of the crystals to detect the scintillation light and convert it to an electrical signal that is amplified and sent for analysis.

The ECAL is a hermetic, homogeneous calorimeter covering the pseudorapidity range $|\eta| < 1.479$ in the barrel and $1.479 < |\eta| < 3.0$ in the endcaps. The crystals in the barrel are grouped into units, called supermodules, of 1700 crystals, while in the endcap they grouped into units, called supercrystals, of 25 crystals. These crystals have short radiation ($X_0 = 0.89$ cm) and Moliere (2.2 cm) lengths, are fast (scintillation decay time is of the same order of magnitude as the LHC bunch crossing time: about 80% of the light is emitted within 25 ns) and radiation hard (up to 10 Mrad). However, the relatively low light yield (30 γ/MeV) requires use of photodetectors with intrinsic gain that can operate in a magnetic field. Silicon avalanche photodiodes (APDs) are used as photodetectors in the barrel and vacuum phototriodes (VPTs) in the endcaps.

The Preshower detector (ES) in the endcaps, identify neutral pions within a fiducial region $1.653 < |\eta| < 2.6$. It also helps the identification of electrons against minimum ionizing particles, and improves the position determination of electrons and photons with it superior granularity. The ES is a sampling calorimeter with 2 layers: lead radiators initiate electromagnetic showers from incoming photons/electrons whilst silicon strip sensors placed after each radiator measure the energy deposited and the transverse shower profiles.

2.2.3 Hadronic Calorimeter

The HCAL in conjunction with the ECAL subdetectors form a complete calorimetry system for the measurement of jets and missing transverse energy. The HCAL is a sampling calorimeter which finds a particle's position, energy and arrival time using alternating layers of "absorber" and fluorescent "scintillator" materials that produce a rapid light pulse when the particle passes through. Special optic fibres collect up this light and feed it into readout boxes where photodetectors amplify the signal. When the amount of light in a given region is summed up over many layers of tiles in depth, called a "tower", this total amount of light is a measure of a particle's energy.

The central barrel and endcap HCAL subdetectors completely surround the ECAL and are fully immersed within the high magnetic field of the solenoid. The barrel (HB) and endcap (HE) are joined hermetically with the barrel extending out to $|\eta| = 1.4$ and the endcap covering the overlapping range $1.3 < |\eta| < 3.0$. The forward calorimeters are located 11.2 m from the interaction point and extend the pseudorapidity coverage overalapping with the endcap from $|\eta| = 2.9$ down to $|\eta| = 5$. The forward calorimeters (HF) are specifically designed to measure energetic forward jets optimized to discriminate the narrow lateral shower profile and to increase the hermeticity of the missing transverse energy measurement. Central shower containment in the region $|\eta| < 1.26$ is improved with an array of scintillators located outside the magnet in the outer barrel hadronic calorimeter (HO).

The design of the HCAL is strongly influenced by the choice of magnet parameters since most of the CMS calorimetry is located inside the magnet coil and surrounds the ECAL system. An important requirement of HCAL is to minimize the non-Gaussian tails in the energy resolution and to provide good containment and hermeticity for the E_T^{miss} measurement. Hence, the HCAL design maximizes material inside the magnet coil in terms of interaction lengths. This is complemented by an additional layer of scintillators, referred to as the hadron outer (HO) detector, lining the outside of the coil. Brass has been chosen as absorber material as it has a reasonably short interaction length, is easy to machine and is non-magnetic. Maximizing the amount of absorber before the magnet requires keeping to a minimum the amount of space devoted to the active medium. The tile/fibre technology makes for an ideal choice.

The hadron barrel (HB) part of HCAL consists of 32 towers covering the pseudorapidity region $-1.4 < \eta < 1.4$, resulting in 2304 towers with a segmentation

$\Delta\eta \times \Delta\phi < 0.087 \times 0.087$.

The hadron outer (HO) detector contains scintillators with a thickness of 10 mm, which line the outside of the outer vacuum tank of the coil and cover the region -1.26 $< \eta <$ 1.26. The tiles are grouped in 30$^{\mathrm{o}}$-sectors, matching the segmentation of the DT chambers. They sample the energy from penetrating hadron showers leaking through the rear of the calorimeters and so serve as a "tail-catcher" after the magnet coil. They increase the effective thickness of the hadron calorimetry to over 10 interaction lengths, thus reducing the tails in the energy resolution function. The HO also improves the E_T^{miss} resolution of the calorimeter. HO is physically located inside the barrel muon system and is hence constrained by the geometry and construction of that system.

Each hadron endcap (HE) of HCAL consists of 14 η towers with 5$^{\mathrm{o}}\phi$ segmentation, covering the pseudorapidity region $1.3 < |\eta| < 3.0$. For the 5 outermost towers (at smaller η) the ϕ segmentation is 5$^{\mathrm{o}}$ and the η segmentation is 0.087. For the 8 innermost towers the ϕ segmentation is 10$^{\mathrm{o}}$, whilst the η segmentation varies from 0.09 to 0.35 at the highest η.

Coverage between pseudorapidities of 3.0 and 5.0 is provided by the steel/quartz fibre Hadron Forward (HF) calorimeter. Because the neutral component of the hadron shower is preferentially sampled in the HF technology, this design leads to narrower and shorter hadronic showers and hence is ideally suited for the congested environment in the forward region. The signal originates from Cerenkov light emitted in the quartz fibres, which is then channeled by the fibres to photomultipliers.

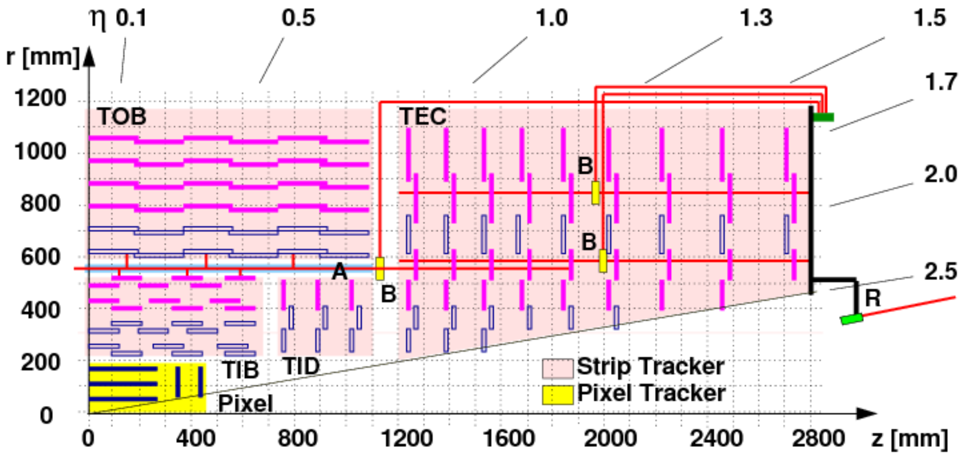

Figure 2.10: CMS tracker system

2.2.4 Inner Tracking System

The inner tracking system in the CMS is used to reconstruct the paths of high-energy muons, electrons and hadrons (particles made up of quarks) as well as see tracks coming from the decay of very short-lived particles such as beauty or "b quarks" that will be used to study the differences between matter and antimatter. The tracker needs to record particle paths accurately yet be lightweight so as to disturb the particle as little as possible. It does this by taking position measurements so accurate that tracks can be reliably reconstructed using just a few measurement points. Each measurement is accurate to 10 μm, a fraction of the width of a human hair. It is also the inner most layer of the detector and so receives the highest volume of particles: the construction materials were therefore carefully chosen to resist radiation. Silicon sensors used in the tracker system are highly suited to receive many particles in a small space due to their fast response and good spatial resolution. Determining the momentum of particles is an important parameter in building up a picture of events at the heart of the collision. One method to calculate the momentum of a particle is to track its path through a magnetic field; the more curved the path, the less momentum the particle has. This is facilitated by the CMS detector which has a strong magnetic field of 4 Tesla in its core. The momentum of a charged particle in a magnetic field is given by:

$$p_T \approx \frac{0.3BL^2}{8s} \tag{2.5}$$

where p_T is the transverse momentum, B is the magnetic field, L is the length of the track and s is the sagitta of the track.

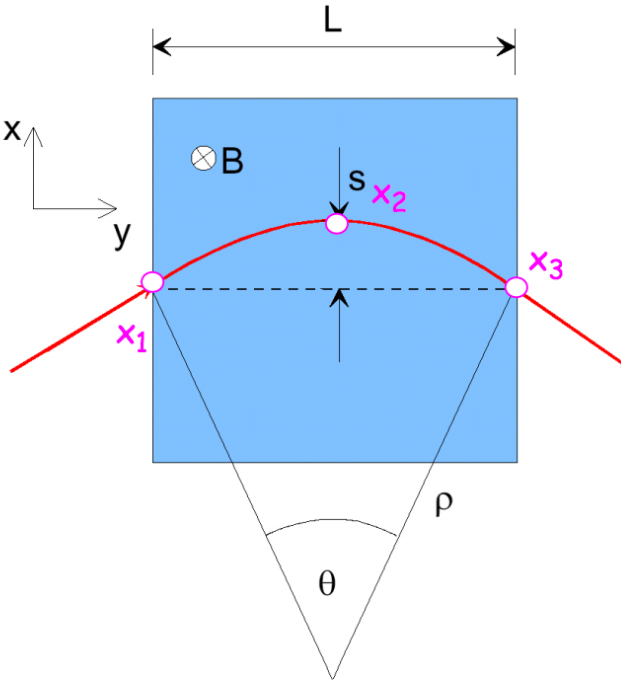

Figure 2.11: Momentum of charged particle in a magnetic field

Based on the charged particle flux at various radii at high luminosity, the tracking system in the CMS is divided into 3 regions:

- Closest to the interaction vertex where the particle flux is the highest (10^7 per second at $r \approx 10$ cm), pixel detectors are placed where size of a pixel is 100×150 μm.
- In the intermediate region ($20 < r < 55$ cm), the particle flux is low enough to enable use of silicon microstrip detectors where minimum cell size is 10×80 μm.
- In the outermost region ($r > 55$ cm), the particle flux is sufficiently low to allow use of larger-pitch silicon microstrips with a maximum cell size of 25×180 μm.

2.2.4.1 Pixel Tracker

When a charged particle passes through the pixel detector, it gives enough energy for electrons to be ejected from the silicon atoms, creating electron-hole pairs. Each pixel uses an electric current to collect these charges on the surface as a small electric signal. The signal is then amplified and sent for read out. The pixel detector consists of 3 barrel layers at radii of 4.4 cm, 7.3 cm and 10.2 cm with 2 endcap disks on each side on them extending from 6 to 15 cm in radius. In order to achieve the optimal vertex position resolution, a design with an "almost" square pixel shape of 100×150 μm^2 in both the (r,ϕ) and the z coordinates has been adopted. The large Lorentz effect (Lorentz angle is 23^{o}) improves the $r - \phi$ resolution through charge sharing. The barrel comprises of 768 pixel modules while the endcap disks have 672 pixel modules. Being closest to the IP, it plays an important role of reconstructing the tracks of very short-lived particles as well as reconstruction of vertices.

2.2.4.2 Strip Tracker

The silicon detectors work in much the same way as the pixels: as a charged particle crosses the material it knocks electron from atoms and within the applied electric field these move giving a very small pulse of current lasting a few nanoseconds. This small amount of charge is then amplified by APV25 chips, giving us "hits" when a particle passes, allowing us to reconstruct its path. The strip tracker in the barrel region is divided into 2 parts: a Tracker Inner Barrel (TIB) and a Tracker Outer Barrel (TOB). The TIB is made of 4 layers of silicon sensors covering up to $|\mathrm{z}| < 65$ cm. The first 2 layers are made with "stereo" modules in order to provide a measurement in both $r - \phi$ and $r - z$ coordinates. The TOB comprises 6 layers with a half-length of $|z| < 110$ cm. As the radiation levels are smaller in this region, thicker silicon sensors are used still maintaining a good S/N ratio. Also for the TOB the first 2 layers provide a "stereo" measurement in both $r - \phi$ and $r - z$ coordinates.

The endcaps are divided into the Tracker End Cap (TEC) and Tracker Inner Disks (TID). Each TEC comprises 9 disks that extend into the region 120 cm$< |z| <$ 280 cm, and each TID comprises 3 small disks that fill the gap between the TIB and the TEC. The TEC and TID modules are arranged in rings, centred on the beam line, and have strips that point towards the beam line, therefore having a variable pitch. The first 2 rings of the TID and the innermost 2 rings and the fifth ring of the TEC have "stereo" modules. The entire silicon strip detector consists of almost 15400 modules, operating at a temperature around 20°C.

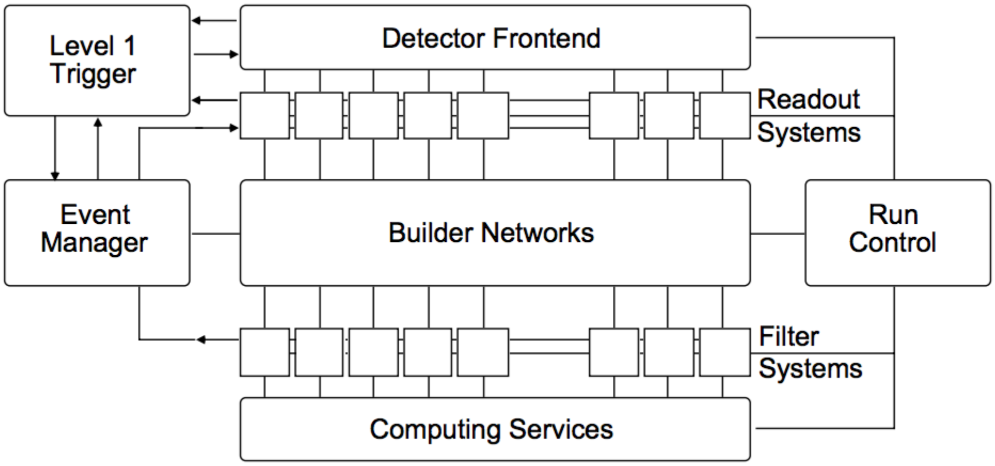

Figure 2.12: Trigger and Data Acquisition system

2.2.5 Trigger and Data Acquisition

The average number of events in each bunch crossing at the design luminosity of 10^{34} cm^{-2}s^{-1} for a bunch spacing of 25 ns corresponding to 10^9 interactions every second. Storing each and every interactions is beyond the reach of current technology. So it is reduced by a factor of 10^7 to 100 Hz, which is the maximum rate that can be archived by the on-line computer farm. CMS reduces this rate in two steps. At the first level (called Level-1), all the data is stored for 3.2 μs, after which no more than 100 kHz of the stored events are forwarded to the High Level Trigger (HLT) which is called the Level-2,3. The Level-1 (L1) system is based on hardware while the HLT on the other hand, mostly uses software to reduce the size of data further to 100 Hz. The L1 system uses only coarsely segmented data from calorimeter and muon detectors, while holding all the high-resolution data in pipeline memories in the front-end electronics. The physical size of the CMS detector and underground caverns imposes constraints on signal propagation that combine with electronics technology to require 3.2 μs, equivalent to 128 25-ns bunch crossings, for any primary decision to discard data from a particular beam crossing. During this 3.2 μs period, trigger data must be collected from the front end electronics, decisions must be developed that discard a large fraction of the data while retaining the small portion coming from interactions of interest and these decisions must be propagated to the readout electronics front end buffers.

The trigger is the start of the physics event selection process. A decision to retain an event for further consideration has to be made every 25 ns. This decision is based on the event's suitability for inclusion in one of the various data sets to be used for analysis. The following physics requirements on the L1 trigger are chosen to provide a high efficiency for the hard scattering physics to be studied at the LHC:

- The CMS trigger system should be capable of selecting leptons and jets over the pseudorapidity range $|\eta| < 2.5$, with an efficiency which is very high, above a selected threshold in transverse momentum.

- For the single lepton triggers it is required that the trigger is fully efficient ($> 95\%$) in the pseudorapidity range $|\eta| < 2.5$, with a threshold of $p_T > 40$ GeV.

- For the dilepton trigger, it is required that the trigger is fully efficient ($> 95\%$) in the pseudorapidity range $|\eta| < 2.5$ with thresholds of $p_T > 20$ and 15 GeV for the first and second leptons respectively.

- Single photon and diphoton triggers are required to have thresholds similar to those of the leptons.

- Single and multiple jet triggers are required with a well defined efficiency over the entire rapidity range $|\eta| < 5$ in order to reconstruct jet spectra that overlap with data attainable at lower energy colliders such as the Tevatron. For higher transverse momenta the jet trigger should also be fully efficient.
- A missing transverse energy trigger with a threshold of about 100 GeV is required.

2.2.5.1 Level-1 Trigger

The L1 Trigger System is organized into three major subsystems: the L1 calorimeter trigger, the L1 muon trigger, and the L1 global trigger. The muon trigger is further organized into subsystems representing the 3 different muon detector systems, the Drift Tube Trigger in the barrel, the Cathode Strip Chamber (CSC) trigger in the endcap and the Resistive Plate Chamber (RPC) trigger covering both barrel and endcap. The L1 muon trigger also has a global muon trigger that combines the trigger information from the DT, CSC and RPC trigger systems and sends this to the L1 global trigger. The data used as input to the L1 trigger system as well as the input data to the global muon trigger, global calorimeter trigger and the global trigger are transmitted to the DAQ for storage along with the event readout data. In addition, all trigger objects found, whether they were responsible for the L1 trigger or not, are also sent. The decision whether to trigger on a specific crossing or to reject that crossing is transmitted via the Trigger Timing and Control (TTC) system to all of the detector subsystem front end and readout systems.

The **calorimeter trigger** begins with trigger tower energy sums formed by the

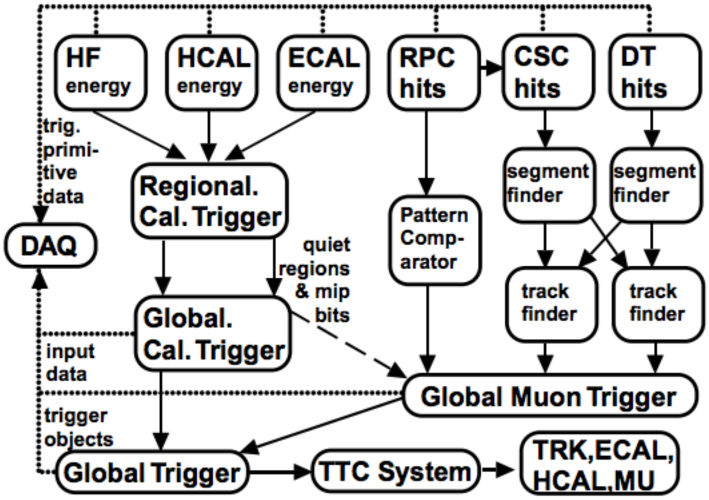

Figure 2.13: Level-1 Trigger system

ECAL, HCAL and HF upper level readout Trigger Primitive Generator (TPG) circuits from the individual calorimeter cell energies. For the ECAL, these energies are accompanied by a bit indicating the transverse extent of the electromagnetic energy deposit. For the HCAL, the energies are accompanied by a bit indicating the presence of minimum ionizing energy. The TPG information is transmitted over high speed copper links to the Regional Calorimeter Trigger (RCT), which finds candidate electrons, photons, taus, and jets. The RCT separately finds both isolated and nonisolated electron/photon candidates. The RCT transmits the candidates along with sums of transverse energy to the Global Calorimeter Trigger (GCT). The GCT sorts the candidate electrons, photons, taus, and jets and forwards the top 4 of each type to the global trigger. The GCT also calculates the total transverse energy and total missing energy vector. It transmits this information to the global trigger as well. The RCT also transmits an (η,ϕ) grid of quiet regions to the global muon trigger for muon isolation cuts.

Each of the L1 **muon trigger** systems has its own trigger logic. The RPC strips are connected to a Pattern Comparator Trigger (PACT), which is projective in η and ϕ. The PACT forms trigger segments which are connected to segment processors which find the tracks and calculate the p_T. The RPC logic also provides some hit data to the CSC trigger system to improve resolution of ambiguities caused by 2 muons in the same CSC. The Cathode Strip Chambers form Local Charged Tracks (LCT) from the Cathode Strips, which are combined with the Anode wire information for bunch crossing identification on a Trigger Motherboard The LCT pattern logic assigns a p_T and quality, which is used to sort the LCT on the Motherboard and the Muon Port Card that collects LCTs from up to 9 CSC chambers. The top 3 LCTs from all the MPCs in a sector are transmitted to the CSC Track Finder, which combines the LCTs into full muon tracks and assigns p_T values to them. The CSC and Drift Tube Track-Finders exchange track segment information in the region where the chambers overlap. The Barrel Muon Drift Tubes are equipped with Bunch and Track Identifier (BTI) electronics that finds track segments from coincidences of aligned hits in 4 layers of one drift tube superlayer. The track segments positions and angles are sent to the Track Correlator (TRACO), which attempts to combine the segments from the two SuperLayers (SL) measuring the ϕ coordinate. The best combinations from all TRACOs of a single chamber together with the SL η segments are collected by the Trigger Server. The Trigger Server then sends the best two segments (if found) to the Track Finder, which combines the segments from different stations into full muon tracks and assigns p_T values to them. The Global Muon Trigger sorts the RPC, DT and CSC muon tracks, converts these tracks into the same η, ϕ and p_T scale, and validates the muon sign. It then attempts to correlate the CSC and DT tracks with RPC tracks. It also correlates the found muon tracks with an $\eta - \phi$ grid of quiet calorimeter towers to determine if these muons are isolated. The final ensemble of muons are sorted based on their initial quality, correlation and p_T and then the 4 top muons are sent to the Global Trigger.

The **Global Trigger** accepts muon and calorimeter trigger information, synchronizes matching sub-system data arriving at different times and communicates the Level-1 decision to the timing, trigger and control system for distribution to the sub-systems to initiate the readout. The global trigger decision is made using logical combinations of the trigger data from the Calorimeter and Muon Global Triggers. The CMS L1 system sorts ranked trigger objects, rather than histogramming objects over a fixed threshold. This allows all trigger criteria to be applied and varied at the Global Trigger level rather than earlier in the trigger processing. All trigger objects are accompanied by their coordinates in (η, ϕ) space. This allows the Global Trigger to vary thresholds based on the location of the trigger objects. It also allows the Global Trigger to require trigger objects to be close or opposite from each other. In addition, the presence of the trigger object coordinate data in the trigger data, which is read out first by the DAQ after a L1A, permits a quick determination of the regions of interest where the more detailed HLT analyses should focus. Besides handling physics triggers, the Global Trigger provides for test and calibration runs, not necessarily in phase with the machine, and for prescaled triggers, as this is an essential requirement for checking trigger efficiencies and recording samples of large cross section data. The Global L1 Trigger transmits a decision to either accept (L1A) or reject each bunch crossing. This decision is transmitted through the Trigger Throttle System (TTS) to the Timing Trigger and Control system (TTC). The TTS allows the reduction by prescaling or shutting off of L1A signals in case the detector readout or DAQ buffers are at risk of overflow.

2.2.5.2 High Level Trigger

The CMS L1 Trigger System is required to reduce the input interaction rate of 1 GHz to a filtered event rate of 100 kHz. For physics analysis and further event filtering, the data corresponding to each selected event must then be moved from about 512 front-end buffers to a single location. To match the capabilities of the mass storage and offline computing systems, the final output of the experiment should not exceed 100 events per second. These functions are performed by a system employing a high performance readout network to connect the sub-detector readout units via a switch fabric to the event filter units (which are implemented by a computer farm). The flow of event data are controlled by an event manager system. In order to optimize the data flow, the filter farm performs event selection in progressive stages by applying a series of HLT filters. The initial filtering decision is made on a subset of the data, from detector components such as the calorimeter and muon systems. This avoids saturating the system bandwidth by reading out the large volume of tracking data at 100 kHz. It is expected that initial filtering can reduce the event rate by at least one order of magnitude. The remainder of the full event data are only transferred to the farm after passing these initial filters and the final HLT algorithms are then applied to the complete event. The High Level Triggers have access to all the information used in L1 since this is stored locally in the L1 trigger crates. Consequently, HLT can make further combinations and other topological calculations on the digital list of objects transmitted from L1. More importantly, much information is not available on the time scale of the L1 trigger decision. This information is then used in the HLT which includes that from the tracker and the full granularity of the calorimeters. Eventually, the HLT uses the full event data for the decision to keep an event. The HLT, implemented as a processing farm that is designed to achieve a rejection factor of 10^3, write up to 100 events/second to mass storage. The last stage of HLT processing does reconstruction and event filtering with the primary goal of making data sets of different signatures on easily accessed media.

Chapter 3

CMS Software and Event Reconstruction

3.1 CMS Software

The overall collection of software, referred to as CMSSW, is built around Event Data Model (EDM) Framework. The primary goal of the Framework and EDM is to facilitate the development and deployment of reconstruction and analysis software. The CMSSW event processing model consists of one executable, called cmsRun, and many plug-in modules which are managed by the Framework. All the code needed in the event processing (calibration, reconstruction algorithms, etc.) is contained in the modules. The same executable is used for both detector and Monte Carlo data.

The CMS Event Data Model (EDM) is centered around the concept of an Event. An Event is a C++ object container for all RAW and reconstructed data related to a particular collision. During processing, data are passed from one module to the next via the Event, and are accessed only through the Event. All objects in the Event may be individually or collectively stored in ROOT files, and are thus directly browsable in ROOT. This allows tests to be run on individual modules in isolation. Auxiliary information needed to process an Event is called Event Setup, and is accessed via the EventSetup.

Physically, an event is the result of a single readout of the detector electronics and the signals that will (in general) have been generated by particles, tracks, energy deposits, present in a number of bunch crossings. The task of the online Trigger and Data Acquisition System (TRIDAS) is to select, out of the millions of events recorded in the detector, the most interesting 100 or so per second, and then store them for further analysis. An event has to pass two independent sets of tests, or Trigger Levels, in order to qualify. The tests range from simple and of short duration (Level-1) to sophisticated ones requiring significantly more time to run (High Levels 2 and 3, called HLT). In the end, the HLT system creates RAW data events containing:

- the detector data
- the level 1 trigger result
- the result of the HLT selections (HLT trigger bits) and
- some of the higher-level objects created during HLT processing.

The CMS data flow includes several steps (Fig - 3.1). Raw data from the HLT is digitized, and collision events are reconstructed to form the Reco dataset from which the AOD dataset is generated. AOD comprises about one to four billion events of roughly 400 kilobytes each

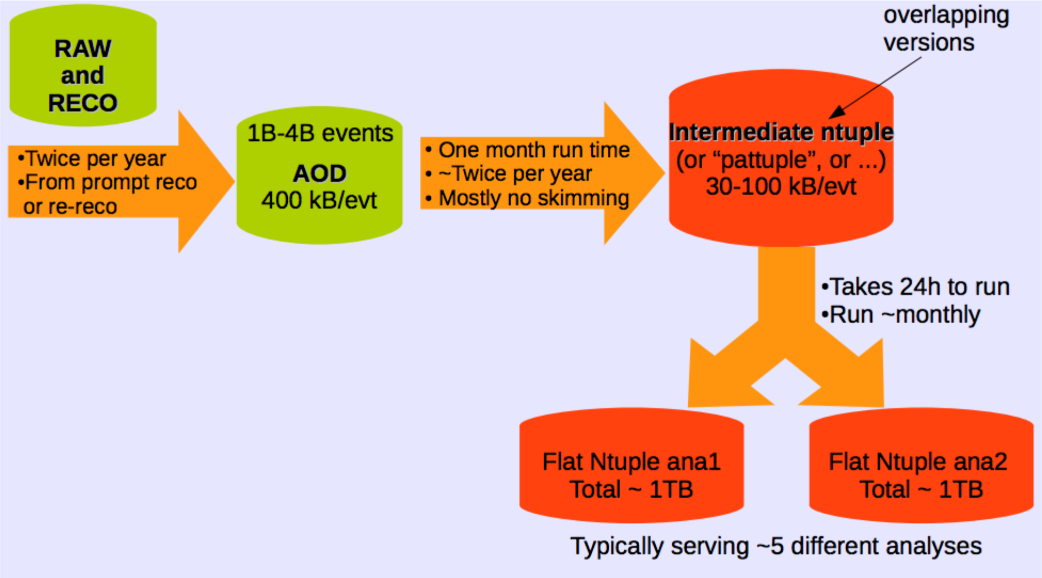

Figure 3.1: Data flow in CMSSW

in size. From multiple copies of AOD spread across many CMS computing sites, physics analysis groups generates intermediate datasets called ntuples that have more specialized formats intended for particular analysis needs. The last step is for individual analysis groups to generate simple, flat ntuples for their specific needs from the intermediate ntuples. Unfortunately, the different sets of intermediate ntuples were largely overlapping, and many copies of them were made throughout the CMS storage infrastructure. In Run 2, given the vast increase in the amount of data, this data flow would not be sustainable. The new CMS data flow for Run 2 replaces the many, duplicative intermediate ntuples with one standard, condensed dataset called Mini-AOD. Without the need for specialized intermediate ntuples, the multiple copies of AOD used in Run 1 to support ntuple generation have also been eliminated. Mini-AOD is produced centrally by the CMS computing group and provides a common foundation for CMS physics analyses. Its compressed format is one tenth the size of AOD, and it provides CMS the solution for handling the large influx of data coming from

Run 2. It is designed to meet the needs of most CMS physics analyses while fitting within storage constraints.

3.2 Event Reconstruction

Event reconstruction in the CMS is accomplished using the particle flow (PF) algorithm [22] which aims at identifying and reconstructing individually each particle arising from the LHC proton-proton collision, by combining the information from all the subdetectors. The resulting particle-flow event reconstruction leads to an improved performance for the reconstruction of jets and MET, and for the identification of electrons, muons, and taus. The ingredients for an efficient PF algorithm arise from these principles: to maximise the separation between charged and neutral hadrons, a large field integral and a good calorimeter granularity are of primary importance. An efficient tracking is a key item as well as a material budget in front of the calorimeters as small as possible. The CMS detector fulfill several of these conditions with a field integral more than twice larger than in other past or existing experiments; an electromagnetic calorimeter with an excellent resolution and granularity, and a tracker system fully exploited by the iterative tracking algorithm.

The CMS PF algorithm relies on a efficient and pure track reconstruction, on a clustering algorithm able to disentangle overlapping showers, and on an efficient link procedure to connect together the deposits of each particle in the sub-detectors. Simplifying, the algorithm can be described as follows: The tracks are extrapolated through the calorimeters, if they fall within the boundaries of one or several clusters, the clusters are associated to the track. The set of track and cluster(s) constitute a charged hadron and the building bricks are not considered anymore in the rest of the algorithm. Muons are identified beforehand so that their track does not give rise to a charged hadron. Electrons are more difficult to deal with. Indeed, due to the frequent Bremsstrahlung photon emission, a specific track reconstruction is needed as well as a dedicated treatment to properly attach the photon clusters to the electron and avoid energy double counting. Once all the tracks are treated, the remaining clusters result in photons in case of the electromagnetic calorimeter (ECAL) and neutral hadrons in the hadron calorimeter (HCAL).

Once all the deposits of a particle are associated, its nature can be assessed, and the information of the sub-detectors combined to determine optimally its four-momentum. In case the calibrated calorimeter energy of the clusters, which is simply a linear combination of the ECAL and HCAL energy deposits, associated to a track is found to be in excess with respect to the track momentum at more than one sigma, the excess is attributed to an overlapping neutral particle (photon or hadron), carrying an energy corresponding to the difference of the two measurements. Reconstruction of photons and jets will not be discussed as they are irrelevant to this analysis.

3.2.1 Track Reconstruction

Track reconstruction [23] refers to the process of using the hits, obtained from the local reconstruction, to obtain estimates for the momentum and position parameters of the charged particles responsible for the hits (tracks). As part of this process, a translation between the local coordinate system of the hits and the global coordinate system of the track is necessary. Reconstructing the trajectories of charged particles is a computationally challenging task. The tracking software at CMS is commonly referred to as the Combinatorial Track Finder (CTF), which is an adaptation of the combinatorial Kalman filter, which in turn is an extension of the Kalman filter to allow pattern recognition and track fitting to occur in the same framework. The collection of reconstructed tracks is produced by multiple passes (iterations) of the CTF track reconstruction sequence, in a process called iterative tracking. The basic idea of iterative tracking is that the initial iterations search for tracks that are easiest to find (e.g., of relatively large p_T, and produced near the interaction region). After each iteration, hits associated with tracks are removed, thereby reducing the combinatorial complexity, and simplifying subsequent iterations in a search for more difficult classes of tracks (e.g., low-pT, or greatly displaced tracks). Iteration 0, the source of most reconstructed tracks, is designed for prompt tracks (originating near the pp interaction point) with pT $>$ 0.8 GeV that have three pixel hits. Iteration 1 is used to recover prompt tracks that have only two pixel hits. Iteration 2 is configured to find low-pT prompt tracks. Iterations 3?5 are intended to find tracks that originate outside the beam spot (luminous region of the pp collisions) and to recover tracks not found in the previous iterations. At the beginning of each iteration, hits associated with high-purity track found in previous iterations are excluded from consideration (masked). Each iteration proceeds in four steps:

- Seed generation provides initial track candidates found using only a few (2 or 3) hits. A seed defines the initial estimate of the trajectory parameters and their uncertainties.

- Track finding is based on a Kalman filter. It extrapolates the seed trajectories along the expected flight path of a charged particle, searching for additional hits that can be assigned to the track candidate.

- The track-fitting module is used to provide the best possible estimate of the parameters of each trajectory by means of a Kalman filter and smoother.

- Track selection sets quality flags, and discards tracks that fail certain specified criteria.

The main differences between the six iterations lie in the configuration of the seed generation and the final track selection.

3.2.1.1 Seed generation

The seeds define the starting trajectory parameters and associated uncertainties of potential tracks. In the quasi-uniform magnetic field of the tracker, charged particles follow helical paths and therefore five parameters are needed to define a trajectory. Extraction of these five parameters requires either three 3-D hits, or two 3-D hits and a constraint on the origin of the trajectory based on the assumption that the particle originated near the beam spot. To limit the number of hit combinations, seeds are required to satisfy certain weak restrictions, for example, on their minimum p_T and their consistency with originating from the pp interaction region.

In principle, it is possible to construct seeds in the outermost regions of the tracker, where the track density is smallest, and then construct track candidates by searching inwards from the seeds for additional hits at smaller distances from the beam-line. However, there are several reasons why an alternative approach, of constructing seeds in the inner part of the tracker and building the track candidates outwards, has been chosen instead. First, although the track density is much higher in the inner region of the tracker, the high granularity of the pixel detector ensures that the channel occupancy of the inner pixel layer is much lower than that of the outer strip layer. Second, the pixel layers produce 3-D spatial measurements, which provide more constraints and better estimates of trajectory parameters. Finally, generating seeds in the inner tracker leads to a higher efficiency for reconstructing tracks. Although most high-pT muons traverse the entire tracker, a significant fraction of the produced pions interact inelastically in the tracker. In addition, many electrons lose a significant fraction of their energy to bremsstrahlung radiation in the tracker. Therefore, to ensure high efficiency, track finding begins with trajectory seeds created in the inner region of the tracker. This also facilitates reconstruction of low-momentum tracks that are deflected by the strong magnetic field before reaching the outer part of the tracker.

Seed generation requires information on the position of the centre of the reconstructed beam spot, obtained prior to track finding and the locations of primary vertices in the event, including those from pileup events. This information is obtained by running a very fast track and vertex reconstruction algorithm, that uses only hits from the pixel detector. The tracks and primary vertices found with this algorithm are known as pixel tracks and pixel vertices, respectively.

The seed generation algorithm is controlled by two main sets of parameters: seeding layers and tracking regions. The seeding layers are pairs or triplets of detector layers in which hits are searched for. The tracking regions specify the limits on the acceptable track parameters, including the minimum p_T, and the maximum transverse and longitudinal distances of closest approach to the assumed production point of the particle, taken to be located either at the centre of the reconstructed beam spot or at a pixel vertex. If the seeding layers correspond to pairs of detector layers, then seeds are constructed using one hit in each layer. A hit pair is accepted as a seed if the corresponding track parameters are consistent with the requirements of the tracking region. If the seeding layers correspond to triplets of detector layers, then, after pairs of hits are found in the two inner layers of each triplet, a search is performed in the outer detector layer for another hit. If the track parameters derived from the three hits are compatible with the tracking region requirements, the seed is accepted. It is also possible to check if the hits associated with the seed have the expected charge distribution from the track parameters: a particle that enters the detector at a grazing angle will have a larger cluster size than a particle that enters the detector at a normal angle. Requiring the reconstructed charge distribution to match the expected charge distribution can remove many fake seeds.

3.2.1.2 Track finding

The track-finding module of the CTF algorithm is based on the Kalman filter method. The filter begins with a coarse estimate of the track parameters provided by the trajectory seed, and then builds track candidates by adding hits from successive detector layers, updating the parameters at each layer. The information needed at each layer includes the location and uncertainty of the detected hits, as well as the amount of material crossed, which is used to estimate the effects of multiple Coulomb scattering and energy loss. The track finding is implemented in the four steps listed below.

- The first step (navigation) uses the parameters of the track candidate, evaluated at the current layer, to determine which adjacent layers of the detector can be intersected through an extrapolation of the trajectory, taking into account the current uncertainty in that trajectory. The navigation service can be configured to propagate along or opposite to the momentum vector, and uses a fast analytical propagator to find the intercepted layers. The analytical propagator assumes a uniform magnetic field, and does not include effects of multiple Coulomb scattering or energy loss. With these assumptions, the track trajectory is a perfect helix, and the propagator can therefore extrapolate the trajectory from one layer to the next using rapid analytical calculations. In the barrel, the cylindrical geometry makes navigation particularly easy, since the extrapolated trajectory can only intercept the layer adjacent to the current one. In the endcap and barrel-endcap transition regions, navigation is more complex, as the crossing from one layer does not uniquely define the next one.

- The second step involves a search for compatible silicon modules in the layers returned by the navigation step. A module is considered compatible with the trajectory if the position at which the trajectory intercepts the module surface is no more than some given number (currently three) of standard deviations outside the module boundary. Since the propagation of the trajectory parameters, and of the corresponding uncertainties, to the sensor surface involves mathematical operations and routines that are generally quite time-consuming the code responsible for searching for compatible modules is optimized to limit the number of sensors that are considered, while preserving an efficiency of $>$99% in finding the relevant sensors.

- The third step forms groups of hits, each of which is defined by the collection of all the hits from one of the module groups. A configurable parameter provides the possibility of adding a ghost hit to represent the possibility that the particle failed to produce a hit in the module group, for example, as a result of module inefficiency. The hit positions and uncertainties are refined using the trajectory direction on the sensor surface, to calculate more accurately the Lorentz drift of the ionization-charge carriers inside the silicon bulk. A χ^2 test is used to check which of the hits are compatible with the extrapolated trajectory. The current (configurable) requirement is $\chi^2 < 30$ for one degree of freedom (dof). The χ^2 calculation takes into account both the hit and trajectory uncertainties. In the endcap regions and the barrel-endcap transition regions, the extrapolation distances and the amount of material traversed are generally greater, with correspondingly larger uncertainties in the trajectory, and the probability of finding spurious hits compatible with the track tends therefore to be greater.

- The fourth and last step is to update the trajectories. From each of the original track candidates, new track candidates are formed by adding exactly one of the compatible hits from each module grouping. As the modules in a given group are mutually exclusive, it would not be expected that a track would have more than one hit contributing from each group. The trajectory parameters for each new candidate are then updated at the location of the module surface, by combining the information from the added hits with the extrapolated trajectory of the original track candidate.

All resulting trajectory candidates are then grown in turn to the next compatible layer(s), and the procedure is repeated until either the outermost layer of the tracker is reached or a "stopping condition" is satisfied. In order not to bias the result, all trajectory candidates are grown in parallel. To avoid an exponential increase of the number of trajectory candidates, the total number of candidates is truncated at each layer. To limit the number of combinations, and hence to avoid an exponential increase thereof, only a limited number of these are retained at each step, based on their normalized χ^2 and number of valid and invalid hits.

Ambiguities in track finding arise because a given track may be reconstructed starting from different seeds, or because a given seed may result in more than 1 trajectory candidate. These ambiguities, or mutually exclusive track candidates, must be resolved in order to avoid double counting of tracks. The ambiguity resolution is based on the fraction of hits that are shared between 2 trajectories. For any pair of track candidates, this fraction is defined in the following way:

$$f_{\text{shared}} = \frac{N^{\text{hits}}_{\text{shared}}}{\min(N^{\text{hits}}_1, N^{\text{hits}}_2)} \tag{3.1}$$

where $N^{\text{hits}}_1(N^{\text{hits}}_2)$ is the number of hits in the first (second) track candidate. If this fraction exceeds a value of 0.5, the track with the least number of hits is discarded, or, if both tracks have the same number of hits, the track with the highest χ^2 value is discarded. The ambiguity resolution is applied twice: the first time on all track candidates resulting from a single seed, and the second time on the complete set of track candidates from all seeds.

3.2.1.3 Track fitting

For each trajectory, the building stage results in a collection of hits and in an estimate of the track parameters. However, the full information is only available at the last hit of the trajectory and the estimate can be biased by constraints applied during the seeding stage. Therefore the trajectory is refitted using a least-squares approach, implemented as a combination of a standard Kalman filter and smoother. The Kalman filter is initialized at the location of the innermost hit with an estimate obtained during seeding. The corresponding covariance matrix is scaled by a large factor in order to avoid any bias. The fit then proceeds in an iterative way through the list of hits. For each valid hit the position estimate is re-evaluated using the current values of the track parameters: information about the angle of incidence increases the precision of the measurement especially in the pixel modules. The track parameters and their covariance matrix are updated with the measurement and the trajectory is propagated to the surface associated with the next hit. The track parameters and their covariance matrix are modified according to the estimates for energy loss and multiple scattering at the target surface and the sequence is repeated until the last hit is included. This first filter is complemented with a smoothing stage: a second filter is initialized with the result of the first one - except for the covariance matrix, which is scaled with a large factor and run backward toward the beam line. At each hit the "updated" parameters of this second filter, which contain all information from the outermost hit up to and including the current hit, are combined with the "predicted" parameters of the first filter, i.e., the information from the innermost hit outward, but excluding the current hit. This filtering and smoothing procedure yields optimal estimates of the parameters at the surface associated with each hit and, specifically, at the first and the last hit of the trajectory. Estimates on other surfaces, e.g., at the impact point, are then derived by extrapolation from the closest hit.

3.2.1.4 Track selection

In a typical LHC event containing jets, the track-finding procedure described above yields a significant fraction of fake tracks, where a fake track is defined as a reconstructed track not associated with a charged particle. The fake rate (fraction of reconstructed tracks that are fake) can be reduced substantially through quality requirements. Tracks are selected on the basis of the number of layers that have hits, whether their fit yielded a good χ^2/dof, and how compatible they are with originating from a primary interaction vertex. If several primary vertices are present in the event, as often happens due to pileup, all are considered. To optimize the performance, several requirements are imposed as a function of the track η and p_T, and on the number of layers (N_{layers}) with an assigned hit (where a layer with both rϕ and stereo strip modules is counted as a single layer). Since quality of tracks are paramount to this analysis, reconstructed tracks of highest quality, known in CMS as high-purity tracks are used at the cost of efficiency. The high purity track selection is based on:

- χ^2/n_{dof} of the track fit;
- transverse and longitudinal impact parameters w.r.t. the PV, namely d_0 and d_z;
- significance of impact parameters, $d_0/\delta d_0$ and $d_z/\delta d_z$, where δd_0 and δd_z are uncertainties on impact parameters from the track fit;
- number of tracker layers with a hit on the track;
- number of tracker "3D" layers with a hit on the track (either pixel layers or matched strip layers);
- number of layers missing hits between the first and last hit on the track;
- $\delta p_T/p_T$ from the track fit.

3.2.2 Reconstruction of Beam Spot

The beam spot represents a 3-D profile of the luminous region, where the LHC beams collide in the CMS detector. The beam spot parameters are determined from an average over many events, in contrast to the event-by-event primary vertex that gives the precise position of a single collision. Measurements of the centre and dependence of the luminous region on r and z are important components of event reconstruction. The position of the centre of the beam spot, corresponding to the centre of the luminous region, is used, especially in the HLT, (i) to estimate the position of the interaction point prior to the reconstruction of the primary vertex; (ii) to provide an additional constraint in the reconstruction of all the primary vertices of an event; and (iii) to provide the primary interaction point in the full reconstruction of low-multiplicity data.

The position of the centre of the beam spot can be determined in two ways. The first method is through the reconstruction of primary vertices (see section 6.1), which map out the collisions as a function of x, y and z, and therefore the shape of the beam spot. The mean position in x, y and z, and the size of the luminous region can be determined through a fit of a likelihood to the 3-D distribution of vertex positions. The second method utilizes a correlation between d0 and that appears when the centre of the beam spot is displaced relative to its expected position.

3.2.3 Reconstruction of Primary Vertex

The goal of primary-vertex reconstruction is to measure the location, and the associated uncertainty, of all proton-proton interaction vertices in each event, including the ‘signal’ vertex and any vertices from pileup collisions, using the available reconstructed tracks. It consists of three steps: (i) selection of the tracks, (ii) clustering of the tracks that appear to originate from the same interaction vertex, and (iii) fitting for the position of each vertex using its associated tracks. Track selection involves choosing tracks consistent with being produced promptly in the primary interaction region, by imposing requirements on the maximum value of significance of the transverse impact parameter (< 5) relative to the centre of the beam spot, the number of strip and pixel hits associated with a track (≥ 2 pixel layers, pixel+strip ≥ 5), and the normalized χ^2 from a fit to the trajectory (< 20). To ensure high reconstruction efficiency, even for minimum-bias events, there is no requirement on the p_T of the tracks.

The selected tracks are then clustered on the basis of their z-coordinates at their point of closest approach to the centre of the beam spot. This clustering allows for the reconstruction of any number of proton-proton interactions in the same LHC bunch crossing. The clustering algorithm must balance the efficiency for resolving nearby vertices in cases of high pileup against the possibility of accidentally splitting a single, genuine interaction vertex into more than one cluster of tracks. Track clustering is performed using a deterministic annealing (DA) algorithm, finding the global minimum for a problem with many degrees of freedom, in a way that is analogous to that of a physical system approaching a state of minimal energy through a series of gradual temperature reductions.

After identifying candidate vertices based on the DA clustering in z, those candidates containing at least two tracks are then fitted using an adaptive vertex fitter to compute the best estimate of vertex parameters, including its x, y and z position and covariance matrix, as well as the indicators for the success of the fit, such as the number of degrees of freedom for the vertex, and weights of the tracks used in the vertex. In the adaptive vertex fit, each track in the vertex is assigned a weight between 0 and 1, which reflects the likelihood that it genuinely belongs to the vertex. Tracks that are consistent with the position of the reconstructed vertex have a weight close to 1, whereas tracks that lie more than a few standard deviations from the vertex have small weights. The number of degrees of freedom in the fit is defined as,

$$n_{\text{dof}} = -3 + 2\Sigma w_i \tag{3.2}$$

where w_i is the weight of the i^{th} track, and the sum runs over all tracks associated with the vertex. The value of n_{dof} is therefore strongly correlated with the number of tracks compatible with arising from the interaction region. For this reason, n_{dof} can be also used to select true proton-proton interactions.

3.2.4 Muon Reconstruction

Muon reconstruction [24] starts with the local reconstruction done at the detector level. Tracks are first reconstructed independently in the inner tracker (tracker track) and in the muon system (standalone-muon track). The standalone muon reconstruction uses only data from the muon detectors - the silicon tracker. Both tracking detectors (DT and CSC) and RPCs participate in the reconstruction. Despite the coarser spatial resolution, the RPCs complement the tracking chambers, especially where the geometrical coverage is problematic, mostly in the barrel-endcap overlap region. The reconstruction starts with the track segments from the muon chambers obtained by the local reconstruction. The state vectors (track position, momentum, and direction) associated with the segments found in the innermost chambers are used to seed the muon trajectories, working from inside out, using the Kalman-filter technique. The predicted state vector at the next measurement surface is compared with existing measurements and updated accordingly. In the barrel DT chambers, reconstructed track segments are used as measurements in the Kalman-filter procedure. In the endcap CSC chambers, where the magnetic field is inhomogeneous, the individual reconstructed constituents (3-D hits) of the segments are used instead. Reconstructed hits from the RPC chambers are also included. A suitable χ^2 cut is applied in order to reject bad hits, mostly due to showering, delta rays and pair production. The procedure is iterated until the outermost measurement surface of the muon system is reached. A backward Kalman filter is then applied, working from outside in, and the track parameters are defined at the innermost muon station. Finally, the track is extrapolated to the nominal interaction point and a vertex-constrained fit to the track parameters is performed. Based on these objects, two reconstruction approaches are used:

1. Global muon reconstruction (outside-in)
2. Tracker Muon reconstruction (inside-out)

This analysis utilizes global muons due to the fact that global muon reconstruction is more efficient than tracker muon reconstruction at high momenta, $p \geq 5$ GeV, because global muon reconstruction is designed to have high efficiency for muons penetrating through more than one muon station and typically requires segments in at least two muon stations. The global muon reconstruction consists in extending the muon trajectories to include hits in the silicon tracker (silicon strip and silicon pixel detectors). Starting from a standalone reconstructed muon, the muon trajectory is extrapolated from the innermost muon station to the outer tracker surface, taking into account the muon energy loss in the material and the effect of multiple scattering. Silicon layers compatible with the muon trajectory are then determined, and a region of interest within them is defined in which to perform regional track reconstruction. The determination of the region of interest is based on the track parameters and their corresponding uncertainties of the extrapolated muon trajectory, obtained with the assumption that the muon originates from the interaction point. The definition of the region of interest has a strong impact on the reconstruction efficiency, fake rate, and CPU reconstruction time: well measured muons are reconstructed faster and with higher efficiency than poorly measured ones. Inside the region of interest, initial candidates for the muon trajectory (regional seeds) are built from pairs of reconstructed hits. The 2 hits forming a seed must come from 2 different tracker layers, and all combinations of compatible pixel and double-sided silicon strip layers are used in order to achieve high efficiency. In addition, a relaxed beam-spot constraint is applied to track candidates above a given transverse momentum threshold to obtain initial trajectory parameters. Starting from the regional seeds, a track-reconstruction algorithm is applied as mentioned before. At large transverse momenta, $p_T \geq 200$ GeV, the global-muon fit can improve the momentum resolution compared to the tracker-only fit.

Chapter 4

Datasets and Event Simulation

4.1 Monte Carlo Event Simulation

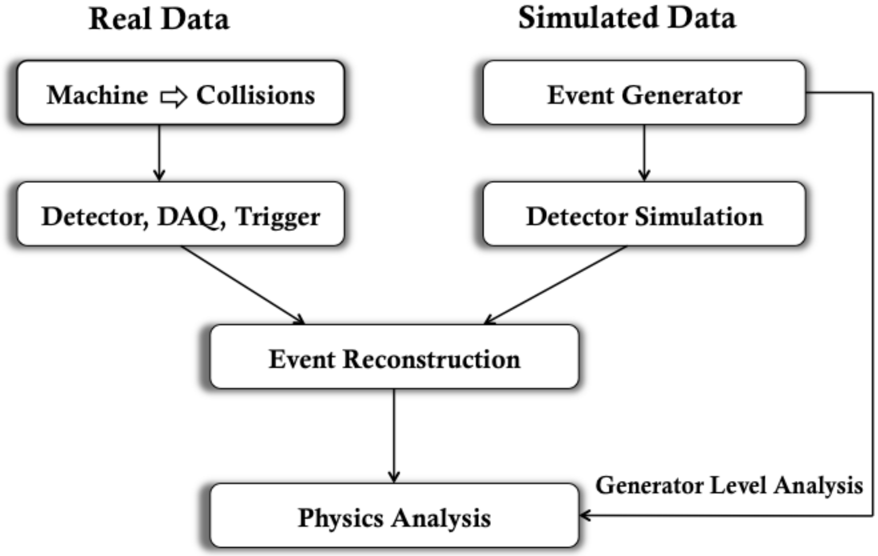

Figure 4.1: Event Generation, Simulation and Reconstruction

Monte Carlo (MC) event generators are essential components of almost all experimental analyses and are widely used by experiments at the LHC to make predictions and preparations for future experiments. Specifically, it gives particle physicists a feeling for the kind of events one may expect to find, and at what rates. The data simulated by these event generators go through the same steps as the real data. The events generated are given as input to the detector simulation which records the virtual hits created by the virtual particles using the detector simulation software Geant4. The event reconstruction algorithms then reconstruct the events i.e. the electronics signals (from wire chambers, calorimeters, and all the rest) may be translated into a deduced setup of charged tracks or neutral energy depositions, in the best of worlds with full knowledge of momenta and particle species identifying them as electrons, muons, taus, photons, hadrons etc. These are then stored at tier 2 centers to be used by research groups for physics analysis. This cycle is illustrated above.

The structure of a proton-proton collision at the LHC as built up by event generators can be described by a few main steps. These are illustrated in below figure where two protons come in from either side and make a collision. The following are the steps into

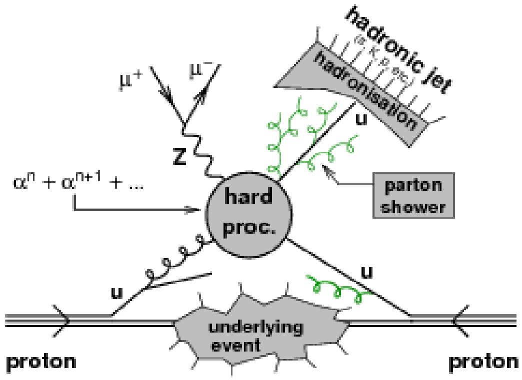

Figure 4.2: Structure of a proton-proton collision

which most event generators divide the process:

- Hard process and Parton Distribution Functions(PDF)
- Parton shower
- Hadronization
- Beam Remnants and Multiple Interactions
- Decays

4.1.1 Hard Process and PDF

When studying proton-proton collisions, most of them are not interesting in the sense that only a few soft hadrons are produced and most of the event goes out along the beam pipe direction. Only a tiny fraction of events contain a high momentum-transfer process of interest. It is therefore not feasible to simulate all possible proton-proton collisions but the simulation needs to be structured with a focus on deciding what hard process is wanted much like the triggers used for selecting only a fraction of the events observed by the detector. This is done by starting the simulation at the heart of the collision and calculating from perturbation theory the probability distribution of a particular hard scatter, which is the highest momentum transfer process in the event. Simulating the hard process is relatively straightforward because PDFs describe partons coming into the process and lowest order perturbation theory gives a probabilistic distribution of the outgoing partons.

The cross section for a process $ij \to k$ is given by,

$$\sigma_{ij\to k} = \int dx_1 \int dx_2 f_i^1(x_1) f_j^2(x_2) \hat{\sigma}_{ij\to k} \tag{4.1}$$

Here $\hat{\sigma}$ is the cross section for the hard partonic process, as codified in the matri$x$elements for each specific process. For processes with many particles in the final state it would be replaced by an integral over the allowed final-state phase space. The $f_j^a(x)$ are the parton-distribution functions, which describe the probability to find a parton i inside beam particle a, with parton i carrying a fraction x of the total a momentum. Actually, parton distributions also depend on some momentum scale Q^2 that characterizes the hard process. Parton distributions are most familiar for hadrons, such as the proton, which are inherently composite objects, made up of quarks and gluons. Since we do not understand QCD, a derivation from first principles of hadron parton distributions does not yet exist, although some progress is being made in lattice QCD studies. It is therefore necessary to rely on parameterizations, where experimental data are used in conjunction with the evolution equations for the Q^2 dependence, to pin down the parton distributions. Several different groups have therefore produced their own fits, based on slightly different sets of data, and with some variation in the theoretical assumptions. The default in Pythia is CTEQ 5L.

4.1.2 Parton showers

The partons involved in the hard process are coloured particles, quarks and gluons. From Quantum Electrodynamics (QED) it is well known that scattered electric charges radiate photons, this is what is called Bremsstrahlung. In the same way, scattered colour charges

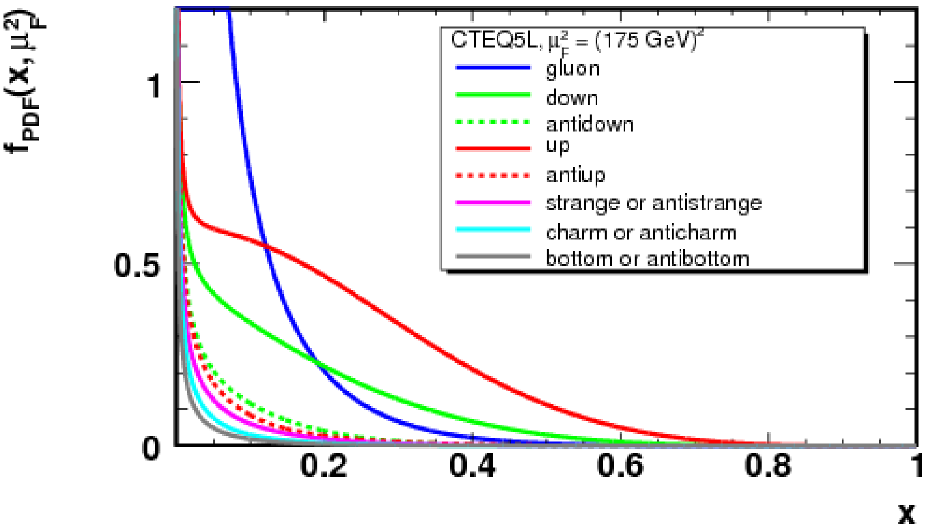

Figure 4.3: Parton Distribution functions

radiate gluons and this happens for partons on their way in and out of a collision leading to Initial State Radiation (ISR) and Final State Radiation (FSR). The main difference to QED is that, due to the non-Abelian structure of SU(3), gluons themselves are coloured and so an emitted gluon can itself trigger new radiation. This leads to an extended shower and the phase space fills up with (mostly) soft gluons. The parton shower can be simulated as a sequential step-by-step process that is formulated as an evolution in momentum transfer scale. The parton shower evolution starts from the hard process and works downwards to lower and lower momentum scales to a point where perturbation theory breaks down.

FSR is fully inclusive in the sense that we want to generate the distribution of all possible parton radiation, for ISR the goal is different. Here, we want to be able to choose the hard process and ask what radiation this process is accompanied by. So, even though the physics involved in ISR and FSR is essentially the same, we have certain kinematic

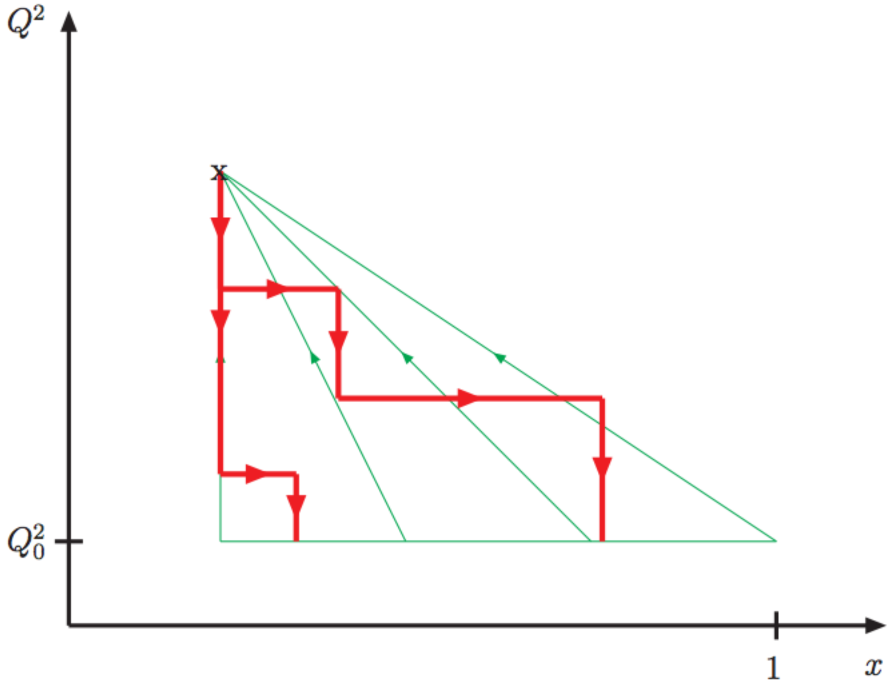

Figure 4.4: The green lines illustrate the flow of information in analytic solutions of the DGLAP evolution equation, which yields the value of the parton distribution function at a given value of $x$and Q^2 as a function of its values at some lower value of Q^2, Q_0^2, and all higher values of x The red lines illustrate typical backward evolution paths that lead to the same $x$and Q^2 value: each path corresponds to one event and each corner on the path to one emitted parton.

constraints for ISR, e.g. we know $x$and Q^2, and we therefore do not want to generate all possible distributions but only those subject to having a fixed parton momentum at the end of the process. As illustrated in Figure 4.4, we can reformulate the evolution as a backward evolution, which probabilistically undoes the DGLAP evolution equations. We start from a particular x and Q^2 point and work down in q^2 and up in x towards the incoming hadron, asking progressively, what is the probability distribution of radiation that accompanies a parton of this flavour and kinematics. In the end, one finds that this algorithm is identical to FSR, but with $\Delta_i(Q^2, q^2)$ replaced by $\Delta_i(Q^2, q^2)/f_i(x, q^2)$.

4.1.3 Hadronization

QCD perturbation theory, formulated in terms of quarks and gluons, is valid at short distances. At long distances, QCD becomes strongly interacting and perturbation theory breaks down. In this confinement regime, the coloured partons are transformed into colourless hadrons, a process called hadronization. It can be considered as the combination of fragmentation and the subsequent decay of unstable particles. The fragmentation process has yet to be understood from first principles, starting from the QCD Lagrangian. This has left the way clear for the development of a number of different phenomenological models. Three main schools are usually distinguished, string fragmentation (SF), independent fragmentation (IF) and cluster fragmentation (CF), but many variants and hybrids exist. Being models, none of them can lay claims to being 'correct', although some may be better founded than others. The SF model is the default in Pythia for all applications though independent fragmentation options also exist.

4.1.4 Decays

A large fraction of the particles produced by fragmentation are unstable and subsequently decay into the observable stable (or almost stable) ones. It is therefore important to include all particles with their proper mass distributions and decay properties. Although involving little deep physics, this is less trivial than it may sound: while a lot of experimental information is available, there is also very much that is missing. For charm mesons, it is necessary to put together measured exclusive branching ratios with some inclusive multiplicity distributions to obtain a consistent and reasonably complete set of decay channels, a rather delicate task. For bottom even less is known, and for some B baryons only a rather simple phase-space type of generator has been used for hadronic decays. Normally it is assumed that decay products are distributed according to phase space, i.e. that there is no dynamics involved in their relative distribution. However, in many cases additional assumptions are necessary, e.g. for semileptonic decays of charm and bottom hadrons one needs to include the proper weak matri$x$elements. Particles may also be produced polarized and impart a non-isotropic distribution to their decay products. Many of these effects are not at all treated in the program. In fact, spin information is not at all carried along, but has to be reconstructed explicitly when needed. This normal decay treatment makes use of a set of tables where branching ratios and decay modes are stored. It encompasses all hadrons made out of d, u, s, c and b quarks, and also the leptons. The decay products are hadrons, leptons and photons. Some $\mathrm{b\bar{b}}$ states are sufficiently heavy that they are allowed to decay to partonic states, like $\Upsilon \rightarrow \mathrm{ggg}$ which subsequently fragment, but these are exceptions.

4.1.5 Beam Remnants and Multiple Interactions

If each incoming particle had only one parton which takes part in hard processes, and that all other constituents sail through unaffected, then the whole process can be described well with the 4 steps that was mentioned above. This approach is appropriate in $\mathrm{e^+e^-}$ or ep events, but not necessarily so in hadron-hadron collisions. Here each of the beam particles contains a multitude of partons, and so the probability for several interactions in one and the same event need not be negligible. In principle these additional interactions could arise because one single parton from one beam scatters against several different partons from the other beam, or because several partons from each beam take part in separate $2 \rightarrow 2$

scatterings. Both are expected, but combinatorics should favour the latter. The understanding of multiple interaction is still very primitive. Pythia therefore contains several different options. These differ on the basis of 'pedestal' effect as well as other differences concerning the level of detail in the generation of scatterings after the first one, and the model that describes how the scatterings are intercorrelated in flavour, colour, and momentum space.

4.2 Datasets

The study is performed on proton-proton collision data of a total integrated luminosity of 19.71 fb^{-1} and 2.09 fb^{-1}, collected with the CMS detector at center-of-mass energies of 8 TeV and 13 TeV respectively.

Table 4.1: Overview of the datasets used in this analysis

Dataset	**Luminosity [fb^{-1}]**
Di-Muon Sample - 2012 (Stream A)	0.876
Di-Muon Sample - 2012 (Stream B)	4.411
Di-Muon Sample - 2012 (Stream C)	7.055
Di-Muon Sample - 2012 (Stream D)	7.369
Di-Muon Sample - 2015 (Stream C)	0.016
Di-Muon Sample - 2015 (Stream D)	2.077

This analysis uses PYTHIA-6.4 [25] and MADGRAPH-5 [26] for simulation of data which performs matrixelement calculations for event generation at Leading Order (LO). The PYTHIA parameters that steer the simulation of hadronisation and the underlying event are set to the most recent PYTHIA Z2* tune. This tune is derived from the Z1 tune [27], which uses the CTEQ5L parton distribution function (PDF) set, whereas Z2* adopts the CTEQ6L PDF set [28]. The list of samples so generated are as given below:

- **NMSSM Higgs signal:**Generation of the gluon-fusion process gg → H_2 as well as $H_2 \to 2H_1$ and $H_1 \to \tau\tau$ decays is done with the LO program PYTHIA. The p_T distribution of the H_2 boson emerging from gluon-fusion is reweighted with NNLO k-factors obtained by the program HqT [29,30], thereby taking into account most precise spectrum calculated to NNLO with resummation to NNLL order.

- **QCD multijet background:** QCD processes are simulated with PYTHIA, followed by filtering procedure at the generator level, selecting events containing at least one muon with transverse momentum exceeding 15GeV.

- **W/Z + Jets production:** The kinematics of W/Z + Jets production with subsequent leptonic decays of the W and Z bosons is simulated using the MADGRAPH event generator interfaced to PYTHIA to account for QCD initial and final state radiation.

- **Inclusive $t\bar{t}$ background:** This background is simulated using the MADGRAPH event generator interfaced to PYTHIA.

- **Di-boson production:** This background is simulated using the PYTHIA event generator.

- **Tau decays:** For all signal and background samples that include taus in the final state, their subsequent decays are simulated using the TAUOLA software package [31], taking into 32 account the polarization properties where appropriate.

The resulting generated events are propagated through a full simulation of the CMS detector based on the GEANT4 package [32] and also including pile-up effects. A weight is associated with each processed event according to the relation:

$$w_{mc} = \frac{\sigma.\mathcal{L}.\epsilon_{mc}}{N_{processed}} \tag{4.2}$$

where σ denotes the cross section of the process considered, $\mathcal{L}$ its integrated luminosity, ϵ_{mc} the MC filter efficiency and $N_{\mathrm{processed}}$ the number of processed MC events.

Chapter 5

Signal Topology and NMSSM Parameter Scans

5.1 Introduction

The recently discovered particle with mass close to 125 GeV [33–35] has been shown to have properties that are consistent with those of a standard model (SM) Higgs boson [36–46]. Supersymmetric (SUSY) extensions of the SM [47] also predict a particle with such properties and resolve some problems of the SM [48]. The minimal supersymmetric standard model (MSSM) [49,50] postulates the existence of two Higgs doublets, resulting in five physical states: two CP-even, one CP-odd, and two charged Higgs bosons. This version of SUSY has been extensively tested using data collected by the ATLAS and CMS experiments at the CERN LHC. However, non-minimal SUSY extensions have received far less attention. One example is the next-to-MSSM (NMSSM), which extends the MSSM by an additional singlet superfield, interacting only with itself and the two Higgs doublets [49,51–57].

This scenario has all the desirable features of SUSY, including a solution of the hierarchy problem and gauge coupling unification. In the NMSSM, the Higgs mixing parameter μ is naturally generated at the electroweak scale through the vacuum expectation value of the singlet field, thereby solving the so-called μ problem of the MSSM [58]. Furthermore, the amount of fine tuning required in the NMSSM to obtain a CP-even Higgs boson with a mass of 125 GeV is significantly reduced compared to the MSSM [59–61]. The Higgs sector of the NMSSM is larger than that of the MSSM. There are seven Higgs bosons: three CP-even ($\mathrm{h}_{1,2,3}$), two CP-odd ($\mathrm{a}_{1,2}$), and two charged Higgs states. By definition, $m_{\mathrm{h}_1} < m_{\mathrm{h}_2} < m_{\mathrm{h}_3}$ and $m_{\mathrm{a}_1} < m_{\mathrm{a}_2}$. Over large parts of the NMSSM parameter space, the observed boson with mass close to 125 GeV, hereafter denoted H(125), could be identified with one of the two lightest scalar NMSSM Higgs bosons, h_1 or h_2. A vast set of next-to-minimal supersymmetric models is consistent with the SM measurements and constraints from searches for SUSY particles made with LHC, Tevatron, SLAC and LEP data, as well as with the properties of the H(125) boson measured using Run 1 LHC data [62–67]. These models provide possible signatures that cannot be realized in the MSSM given recent experimental constraints [68]. For example, the decays $\mathrm{H}(125) \to \mathrm{h}_1\mathrm{h}_1$ and $\mathrm{H}(125) \to \mathrm{a}_1\mathrm{a}_1$ are allowed when kinematically possible. These decay signatures have been investigated in phenomenological studies considering a variety of production modes at the LHC [69–76].

The analysis presented in this paper is motivated by the NMSSM scenarios that predict a very light h_1 or a_1 state with mass in the range $2m_\tau < m_{\mathrm{h}_1}(m_{\mathrm{a}_1}) < 2m_\mathrm{b}$, where m_τ is the mass of the τ lepton and m_b is the mass of the b quark. Such a light state is potentially accessible in final states with four τ leptons, where $\mathrm{H}(125) \rightarrow \mathrm{h}_1\mathrm{h}_1(\mathrm{a}_1\mathrm{a}_1) \rightarrow 4\tau$ [77,78]. In these scenarios the decay $\mathrm{H}(125) \rightarrow \mathrm{a}_2\mathrm{a}_2$ is not kinematically allowed.

Several searches for $\mathrm{H}(125) \rightarrow \phi_1\phi_1$ decays, where ϕ_1 can be either the lightest CP-even state h_1 or the lightest CP-odd state a_1, have been performed. The analyses carried out by the OPAL and ALEPH Collaborations at LEP [79,80] searched for the decay of the CP-even Higgs boson into a pair of light CP-odd Higgs bosons, exploiting the Higgs-strahlung process, where the CP-even state is produced in association with a Z boson. These searches found no evidence for a signal, and limits were placed on the signal production cross section times branching fraction. However, searches at LEP did not probe masses of the CP-even state above 114 GeV. A similar study has been performed by the D0 Collaboration at the Tevatron [81], searching for inclusive production of the CP-even Higgs boson in pp collisions followed by its decay into a pair of light CP-odd Higgs bosons. No signal was detected and upper limits were set on the signal production cross section times branching fraction in the mass ranges $3.6 < m_{\mathrm{a}_1} < 19$ GeV and $89 < m_{\mathrm{H}} < 200$ GeV. The limits set by the D0 analysis are a factor one to seven times higher compared to the SM production cross section for $\mathrm{p\bar{p}} \rightarrow \mathrm{H}(125) + \mathrm{X}$. The CMS Collaboration has recently searched for a very light CP-odd Higgs boson produced in decays of a heavier CP-even state [82]. This study probed the mass of the CP-odd state in the range $2m_\mu < m_{\mathrm{a}_1} < 2m_\tau$, where m_μ is the mass of muon. In this mass range the decay $\mathrm{a}_1 \rightarrow \mu\mu$ can be significant. No evidence for a signal was found and upper limits were placed on the signal production cross section times branching fraction. The ATLAS Collaboration has also recently searched for $\mathrm{h/H} \rightarrow \mathrm{a}_1\mathrm{a}_1 \rightarrow \mu\mu\tau\tau$ [83], covering the mass range $m_{\mathrm{a}_1} =$ 3.7-50 GeV for

$m_{\mathrm{H}} = 125$ GeV, and $m_{\mathrm{H}} = 100$-500 GeV for $m_{\mathrm{a}_1} = 5$ GeV. No excess over SM backgrounds was observed, and upper limits were placed on $\sigma(\mathrm{gg} \to \mathrm{H})\, \mathcal{B}(\mathrm{H} \to \mathrm{a}_1\mathrm{a}_1)\, \mathcal{B}^2(\mathrm{a}_1 \to \tau\tau)$, under the assumption that

$$\frac{\Gamma(\mathrm{a} \to \mu\mu)}{\Gamma(\mathrm{a} \to \tau\tau)} = \frac{m_\mu^2}{m_\tau^2\sqrt{1-(2m_\tau/m_{\mathrm{a}})^2}} \tag{5.1}$$

The search for the production of a pair of light bosons with their subsequent decay into four τ leptons has not yet been performed at the LHC and is the subject of this paper. The choice of the 4τ channel makes it possible to probe the signal cross section times branching fraction

$$(\sigma\mathcal{B})_{\mathrm{sig}} \equiv \sigma(\mathrm{gg} \to \mathrm{H}(125))\, \mathcal{B}(\mathrm{H}(125) \to \phi_1\phi_1)\, \mathcal{B}^2(\phi_1 \to \tau\tau) \tag{5.2}$$

in a model-independent way.

5.2 NMSSM tools and parameter scans

In our analysis we focus on the simplest version of the NMSSM where the μ term of the MSSM is replaced by a scale invariant super potential,

$$\mu\hat{H}_1\hat{H}_2 \to \lambda\hat{S}\hat{H}_1\hat{H}_2 + \frac{\kappa}{3}\hat{S}^3 \tag{5.3}$$

with the associated soft SUSY breaking terms being

$$m_{H_1}^2 H_1^2 + m_{H_2}^2 H_2^2 + m_S^2 S^2 + \lambda A_\lambda H_1 H_2 S + \frac{\kappa}{3} A_\kappa S^3 \tag{5.4}$$

where with hatted and non hatted capital letters we indicate the superfields and their correspondent scalar component respectively. It is possible to recast $m_{\mathrm{H}_1}, m_{\mathrm{H}_2}$ and m_S in terms of $M_{\mathrm{Z}}, \tan\beta$ and $\mu_{\mathrm{eff}} = \lambda \mathrm{s}$ with $s = \langle S \rangle$ the VEV of the singlet Higgs field, and, assuming CP conservation in the Higgs sector, the latter is determined by just 14 Electroweak parameters: tan β, the trilinear couplings in the superpotential, λ and κ, the corresponding SUSY breaking parameters, A_λ and A_κ, μ_{eff}, the gaugino mass parameters, $M_{1,2,3}$, the squark and slepton trilinear couplings, $A_{t,b,\tau}$ and mass parameters, M_{f_L} and M_{f_R}, where for simplicity we have assumed universality across the three generations for the last three set of parameters. We have performed our parameter's space scan using NMSSMTools 4.1 [84] fixing the parameters that intervene in the Higgs sector at loop level at the value of,

$$M_{1,2,3} = 150, 300, 1000 \text{ GeV} \tag{5.5}$$

$$A_{t,b,\tau} = 2500 \text{ GeV} \tag{5.6}$$

$$M_{f_L}, M_{f_R} = 1000 \text{ GeV} \tag{5.7}$$

therefore varying only tan $\beta, \mu_{\mathrm{eff}}, \lambda, \kappa, A_\lambda, A_\kappa$. Besides the constraints already implemented into the NMSSMTools 4.1 package, we have also performed a χ^2 fit of the Higgs signal strengths with respect to the publicly available CMS data for the following final states: $\mathrm{b\bar{b}}$ [1], WW [2], ZZ [3] and $\gamma\gamma$ [4] that are reported in table 5.1. We have performed the fit on the SM like Higgs boson, after it has been identified between h_1 and h_2 with a mass window selection (122.7 GeV $< m_{\mathrm{h(SM)}} <$ 128.7 GeV), neglecting any contribution of the non-SM-like Higgs and assuming an unique production process for each case, that in

Table 5.1: CMS signal strengths for the Higgs boson decaying into b$\bar{\text{b}}$, WW, ZZ and $\gamma\gamma$ final states from [1–4]

	$\hat{\mu}_j \pm \delta\hat{\mu}_j$
$\mu_{\mathrm{b\bar{b}}}$	1.0 ± 0.5
μ_{WW}	0.72 ± 0.19
μ_{ZZ}	0.92± 0.27
$\mu_{\gamma\gamma}$	0.93 ±0.27

particular have been assumed to be:

- 100% of Higgs-Strahlung production for b$\bar{\text{b}}$ final state
- 100% of gluon fusion production for the WW*, ZZ* and $\gamma\gamma$ final states

The signal strength μ for a specific production mode and in a given decay channel has been computed as,

$$\mu_{xx}^{prod} = \frac{[\sigma(pp \to h^{SM})_{prod} \,.\, \mathcal{B}(h^{SM} \to xx)]_{NMSSM}}{[\sigma(pp \to h^{SM})_{prod} \,.\, \mathcal{B}(h^{SM} \to xx)]_{SM}} \tag{5.8}$$

and the χ^2 is given by,

$$\chi^2 = \sum_{j=1} \frac{(\mu_j - \hat{\mu}_j)^2}{\delta\hat{\mu}_j^2}; \quad j = b\bar{b}, WW^*, ZZ^*, \gamma\gamma \tag{5.9}$$

where $\hat{\mu}_j$ and $\delta\hat{\mu}_j$ are reported in table 5.1. We then have excluded from our results the points where $\chi^2 > 9.72$, that corresponds to a p-value greater than ≈ 0.05 for a χ^2 with four degrees of freedom. It should however need to be stressed that within the constraints implemented into the NMSSMTools package a χ^2 fit is already present and constraints on a SM-like Higgs mass (125.7 ± 3 GeV) and its signal rates, from [85], are applied so that our χ^2 fit acts as a check on the one already performed within the program. For our results the cross section for the production of the SM like Higgs boson via gluon fusion (ggh), vector boson fusion (VBF) and Higgs-Strahlung (Vh) for the 8 and 14 TeV LHC has been calculated using the production cross section for a SM Higgs boson provided by the Higgs Cross SectionWorking Group [86] re-weighted for the corresponding reduced couplings square that are hgg, for ggh production, and hVV, for VBF and Vh productions, provided by the NMSSMTools package.

5.3 Topology of $\mathbf{h}^{\mathbf{SM}}_{1,2} \rightarrow \mathbf{a}_1\mathbf{a}_1$

The first topology under analysis is the one where the SM-like Higgs boson decays into a pair of light pseudoscalars a_1 that then decay into a τ pair each,

$$\mathrm{h}^{\mathrm{SM}}_{1,2} \rightarrow \mathrm{a}_1\mathrm{a}_1 \tag{5.10}$$

Since we are interested in a 4τ final state we want to focus on the region where $m_{\mathrm{a}_1} < 10$ GeV in order to be under the $\mathrm{b}\bar{\mathrm{b}}$ threshold and have a significant branching ratio into $\tau\tau$ final state. We have firstly performed a scan over a broad range of the NMSSM parameter space,

$$100 \text{ GeV} < \mu_{\text{eff}} < 1000 \text{ GeV} \tag{5.11}$$

$$1.5 < \tan\beta < 50 \tag{5.12}$$

$$0 < \lambda, \kappa < 1 \tag{5.13}$$

$$-4000 \text{ GeV} < A_\lambda, A_\kappa < 4000 \text{ GeV} \tag{5.14}$$

and from Fig. (5.1) we observe that in order to have a light a_1, small μ_{eff} and A_κ value are preferred. Moreover it was shown in [73], there is a important correlation exists between the combination $\frac{\mu_{\text{eff}}.\kappa}{\lambda}$ and the region where h_1 or h_2 is the SM Higgs boson. In particular when $\frac{\mu_{\text{eff}}.\kappa}{\lambda} < 60$ GeV, h_1 is light and h_2 is the SM like Higgs boson and this constraints can be imposed in order to focus on the region of the parameter space where both the CP even h_1 and h_2 can be the SM like Higgs boson.

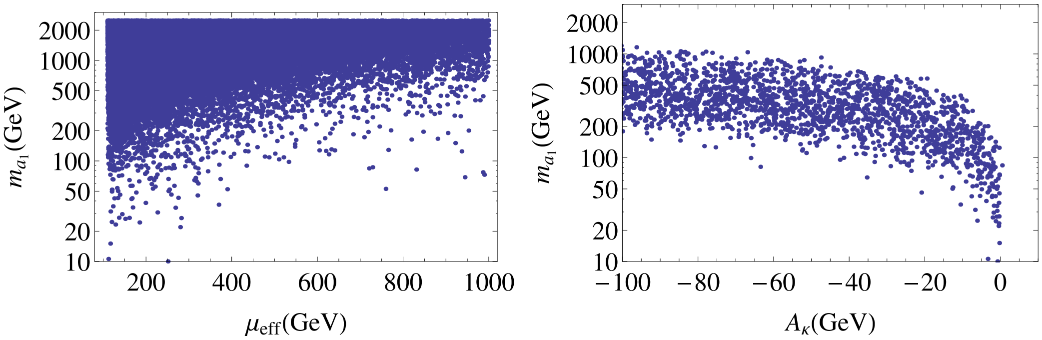

Figure 5.1: Mass of the lightest pseudoscalar a_1 as function of μ_{eff} (left) and A_κ (right).

Following these results we perform a scan adding the following constraints to the parameter space defined in eq. (5.9-5.12),

$$100 \text{ GeV} < \mu_{\text{eff}} < 300 \text{ GeV} \tag{5.15}$$

$$0 < \frac{\mu_{\text{eff}}.\kappa}{\lambda} < 200 \text{ GeV} \tag{5.16}$$

$$-30 < A_\kappa < 10 \tag{5.17}$$

$$m_{\mathrm{a}_1} < 10 \text{ GeV} \tag{5.18}$$

The results for the process,

$$\sigma(\mathrm{pp} \to \mathrm{h}_j^{\mathrm{SM}})_i \ . \ \mathcal{B}(\mathrm{h}_j^{\mathrm{SM}} \to \mathrm{a}_1\mathrm{a}_1) \ . \ \mathcal{B}(\mathrm{a}_1 \to \tau\tau)^2; \quad i = \mathrm{ggH, \ VBF, \ VH}; \quad j = 1, 2 \tag{5.19}$$

for the 8 and 14 TeV LHC are shown in Fig. (5.2) and Fig. (5.3) for both regions where the SM-like Higgs boson (again, identified by a mass window 122.7 GeV $< m_{\mathrm{h}}^{SM} <$ 128.7 GeV) is either h_1 (blue points) or h_2 (cyan points), as a function of the relevant reduced coupling for the production process under consideration, that are $\mathrm{g}_{\mathrm{ggH}}/\mathrm{g}_{\mathrm{ggH}}^{\mathrm{SM}}$ for ggH and $\mathrm{g}_{\mathrm{VVH}}/\mathrm{g}_{\mathrm{VVH}}^{\mathrm{SM}}$ for VBF and VH.

5.4 Topology of $\mathbf{h}_{1,2}^{\mathbf{SM}} \to \mathbf{h}_1\mathbf{h}_1$

We now consider the second topology where the SM Higgs boson is h_2, that decays into a pair of light h_1,

$$\mathrm{h}_{1,2}^{\mathrm{SM}} \to \mathrm{h}_1\mathrm{h}_1 \tag{5.20}$$

With respect to the scan defined in eq. (5.13-5.16) we have defined,

$$0 < \frac{\mu_{\mathrm{eff}} . \kappa}{\lambda} < 50 \text{ GeV} \tag{5.21}$$

$$-400 \text{ GeV} < A_\kappa < 10 \text{ GeV} \tag{5.22}$$

The results for the cross section for the process,

$$\sigma(\mathrm{pp} \to \mathrm{h}_2^{\mathrm{SM}})_i \ . \ \mathcal{B}(\mathrm{h}_2^{\mathrm{SM}} \to \mathrm{h}_1\mathrm{h}_1) \ . \ \mathcal{B}(\mathrm{h}_1 \to \tau\tau)^2; \quad i = \mathrm{ggH} \tag{5.23}$$

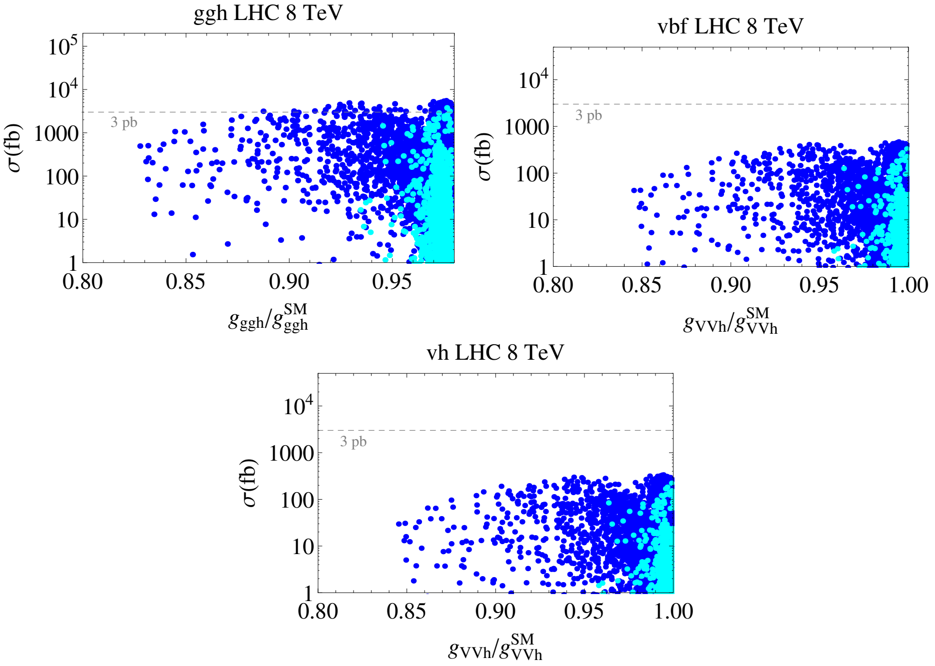

Figure 5.2: Inclusive cross section for the process of eq. (5.17) for the 8 TeV LHC. In blue and cyan the points where h_1 or h_2 is the SM Higgs boson respectively.

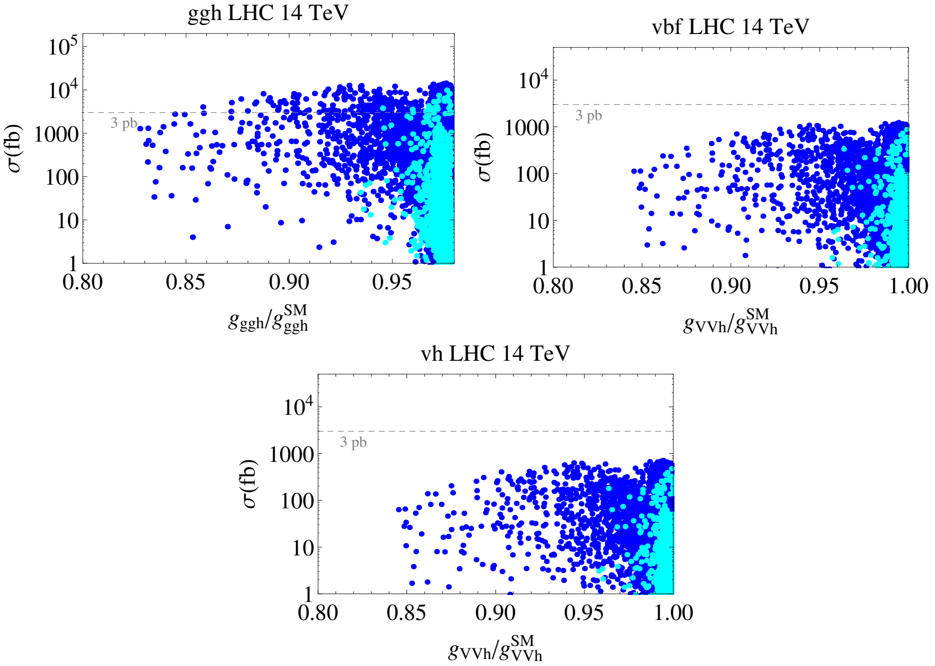

Figure 5.3: Inclusive cross section for the process of eq. (5.17) for the 14 TeV LHC. In blue and cyan the points where h_1 or h_2 is the SM Higgs boson respectively.

for the 8 and 14 TeV LHC for the case of gluon fusion production are shown in Fig. 5.4.

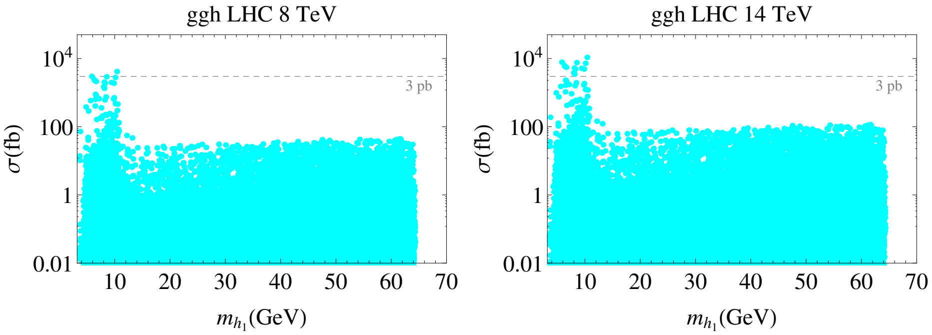

Figure 5.4: Inclusive cross section for the process of eq. (5.21) for the 8 and 14 TeV LHC in function of the mass of the lightest CP even Higgs h_1

5.5 Signal Topology

This analysis searches for the production of the recently discovered state at a mass near 125 GeV, denoted H(125), via gluon fusion with subsequent decay into a pair of light NMSSM Higgs bosons ϕ_1, where ϕ_1 can be either the lightest CP-even state h_1 or the lightest CP-odd state a_1. The signal can be associated with one of three possible scenarios:

- H(125) corresponds to h_2 and decays into a pair of h_1 states, $\mathrm{h}_2 \to \mathrm{h}_1\mathrm{h}_1$;
- H(125) corresponds to h_2 and decays into a pair of a_1 states, $\mathrm{h}_2 \to \mathrm{a}_1\mathrm{a}_1$;
- H(125) corresponds to h_1 and decays into a pair of a_1 states, $\mathrm{h}_1 \to \mathrm{a}_1\mathrm{a}_1$.

The signal topology is illustrated in Fig. 5.5. The search is performed for very light ϕ_1 states, covering a mass range of 4 to 8 GeV. Within this mass range the ϕ_1 boson is expected to decay predominantly into a pair of tau leptons, $\phi_1 \to \tau\tau$. One of the tau leptons in each $\phi_1 \to \tau\tau$ decay leg is identified via its muonic decay. The other tau lepton in each ϕ_1 decay leg is allowed to decay either leptonically, or via the 1-prong semi-hadronic mode (where the tau decays into one charged hadron and one or more neutral particles). Therefore the tau will only have one charged particle among its decay products. We identify these decays by the presence of one reconstructed opposite sign track with respect to the selected muon, and thus the neutral particles will have no effect on the event selection. Given the large difference in mass between the ϕ_1 and the H(125) states ($m_{\mathrm{H(125)}} \gg m_{\phi_1}$), one expects that the ϕ_1 bosons produced will be highly boosted, and consequently their decay products are expected to be strongly collimated. Furthermore, in the gluon fusion process the H(125) is mainly produced with relatively small transverse momentum. Thus, in the majority of H(125) → $\phi_1\phi_1$ decays, the ϕ_1 states will be produced nearly back-to-back in the plane transverse to the beams, with the particles stemming from one ϕ_1 boson decay well separated in azimuthal angle ϕ from the particles produced by the decay of the other ϕ_1 boson. In the gluon fusion process, the H(125) state can be also produced with relatively high boost when a hard gluon is radiated off the initial state gluons or the heavy quark loop. In this

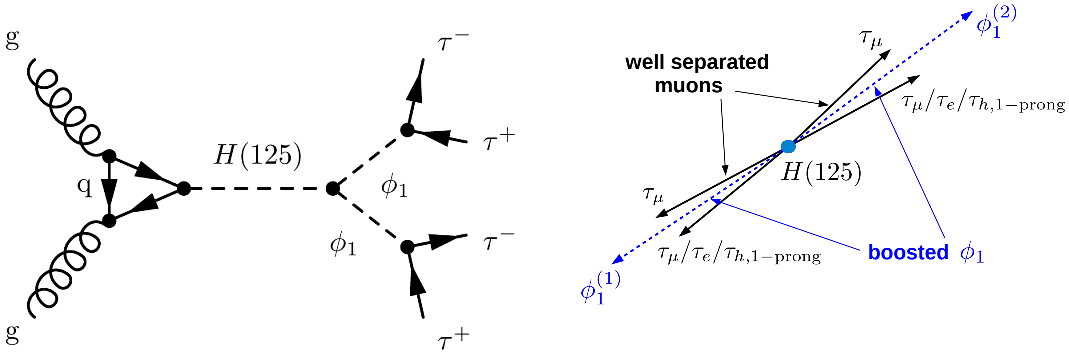

Figure 5.5: Left: Feynmann diagram for the signal process. Right: Illustration of the signal topology.

case, the separation between two ϕ_1 bosons in azimuthal angle can be reduced, while the separation in pseudorapidity η can still be large.

The signal properties discussed above define the search topology. The analysis presented here searches for the signal in a sample of dimuon events with large angular separation imposed between the muons. Each muon is accompanied by one nearby opposite sign track originating from the same ϕ_1 decay leg. Throughout this analysis, the signal yields are normalized to the benchmark value of the signal production cross section times branching fraction of 5 pb. The choice of the benchmark scenario is motivated by recent phenomenological analyses [77, 78].

Chapter 6

Event Selection and Scale Factors

6.1 Trigger selection

Two triggers are used namely HLT_Mu17_Mu8 and HLT_Mu17_TkMu8 and events are selected if one atleast one of them fires. These are dimuon triggers with thresholds on the p_T of the leading and the sub-leading muon being 17 and 8 GeV respectively along with the requirement that the difference between longitudinal impact parameters of muon tracks is less than 2mm. For HLT_Mu17_TkMu8, there is an additional requirement on the sub-leading muon to be a tracker-muon with $p_T > 8$ GeV.

6.2 Primary Vertex

Reconstructed vertices are required to have a z position within 24 cm of the nominal detector center and a radial position within 2 cm from the beamspot. There must be more than four degrees of freedom in the vertex fit. From the set of PV [87] passing these criteria, the vertex with the maximum p_T^2 sum of tracks associated with the vertex is chosen as the hard interaction vertex. With increasing instantaneous luminosity of the LHC machine, the data taking conditions have been changing rapidly. In particular, additional energy is attributed to the reconstructed jets which is not associated to the primary interaction, rather than with other proton-proton interactions at the PV. These additional interactions constitute the Pile Up (PU), and as a consequence a difference in the number of reconstructed PV between the data and the simulated samples is observed. In order to correct for these effects and model coherently the number of PU events in simulation as observed in experimental data, the simulated events are reweighted as a function of the simulated PU interactions as described in Reference [88].

6.3 Muon Identification and Selection

Two muons are selected if they are identified as muons by the particle-flow (PF) algorithm [89, 90] while they are reconstructed by the Global reconstruction algorithm [24]. The muons must fulfill the requirements corresponding to the PF-Tight Muon criteria formulated by the Muon POG (Physics Object Group):

- The χ^2/ndof of the global track fit must be smaller than 10.
- At least one segment in the muon detector is included in the global track fit.
- Muon track segments must be present in at least two stations of the muon detector.
- There must be one hit in the pixel detector and hits in more than 5 layers in the inner track detector.

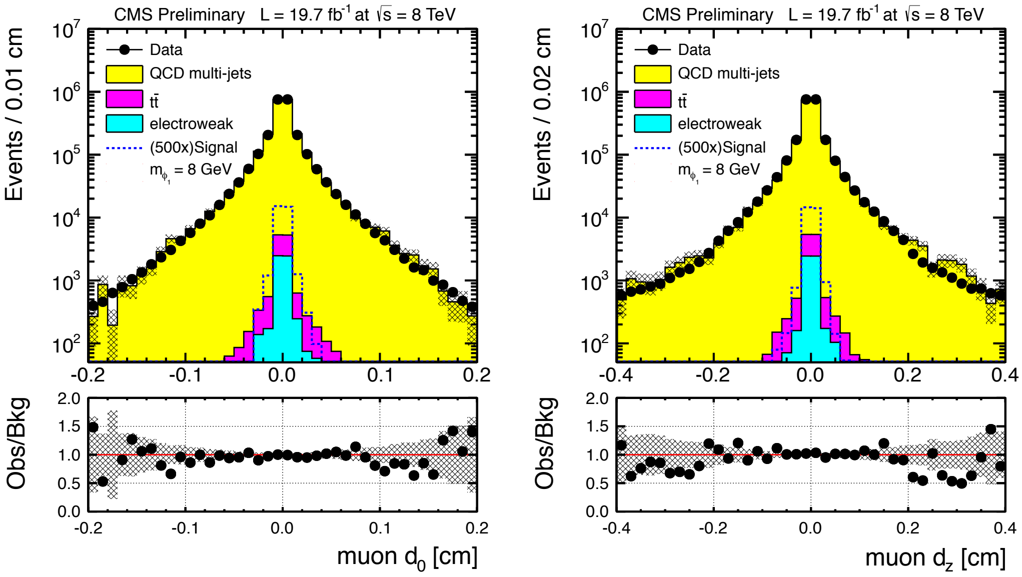

Figure 6.1: Distributions of the muon transverse impact parameter d_0 (left plot) and longitudinal impact parameter d_z (right plot) with respect to the primary interaction vertex in the selected sample of same-sign muon pairs. Data (dots) is compared with the Monte Carlo background predictions (histograms). The dashed histogram shows distribution in the signal sample with $m_{\mathrm{H}_1} = 8$ GeV. The signal distribution is scaled to cross section times branching ratio of 500 pb.

Muons are required to match trigger objects associated with triggers used in the analysis. To reject QCD multi-jet events with muonic decays of the hadrons containing charm and bottom quarks, the cuts are imposed on impact parameters of muon tracks. The impact parameter in the transverse plane with respect to the PV is required to be $|d_0| <$ 0.03 cm. The longitudinal impact parameter with respect to the PV is required to be $|d_z|$ $<$ 0.1 cm.

Further selection imposes the following kinematic cuts:

- pseudorapidity of the leading and the sub-leading muons should be $|\eta| < 2.1$.
- $p_T > 17$ GeV for the leading muon and $p_T > 10$ GeV for the sub-leading muon.

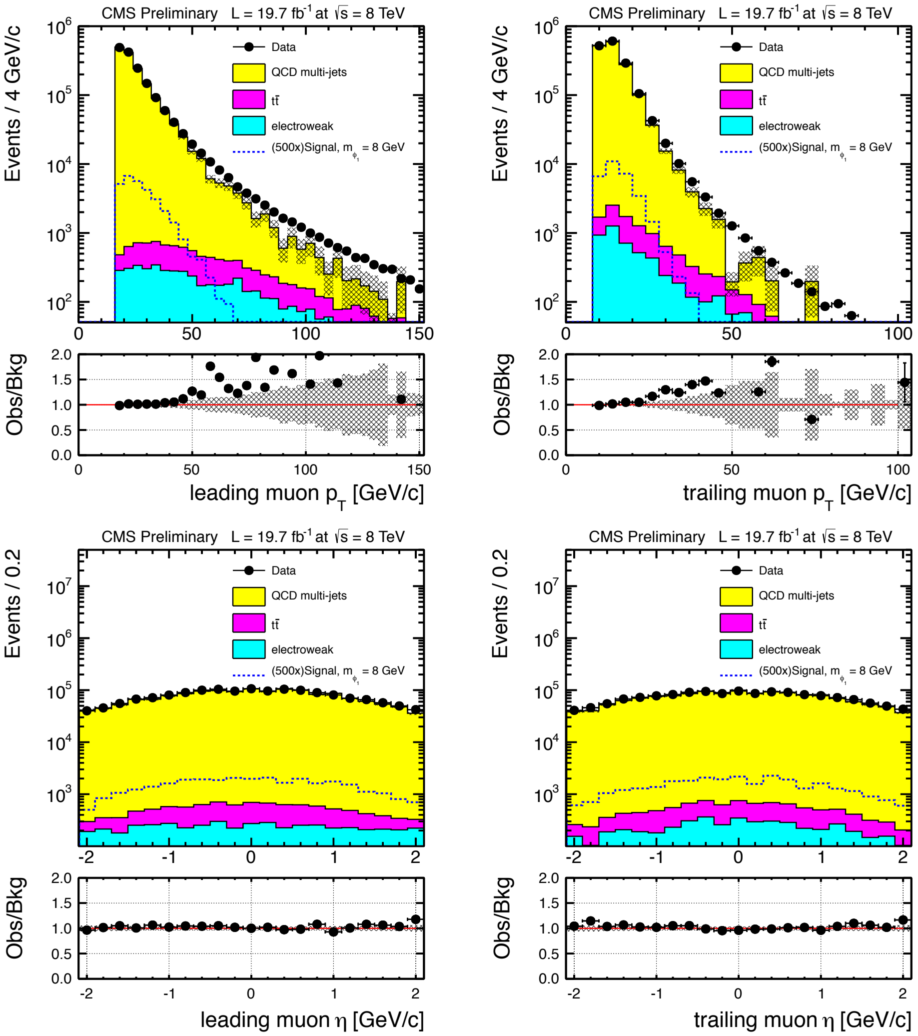

Figure 6.2: Distributions of the leading muon p_T (upper left plot), trailing muon p_T (upper right plot), leading muon pseudo-rapidity (lower left plot) and trailing muon pseudo-rapidity (lower right plot) in the selected sample of same-sign muon pairs.

Two muons are required to have same sign. This requirement significantly suppresses background coming from the Drell-Yan process, top-quark pair production and QCD multi-jet events with muonic decays of heavy flavor hadrons. If more than one same-sign muon pair is found in the event, the pair with the largest sum of muon transverse momenta is chosen. Figure 6.1 compares distributions of the muon impact parameters between

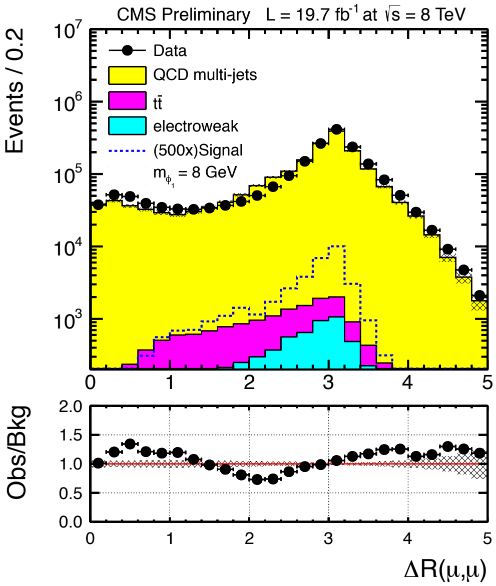

Figure 6.3: Distribution of the $\Delta R(\mu, \mu)$ variable in the selected sample of same-sign muon pairs.

data and simulation in a selected sample of same-sign di-muon events. The kinematical distributions of the two muons are presented in Figure 6.2. Distribution of the $\Delta R(\mu, \mu)$ variable is shown in Figure 6.3. Good agreement between data and simulation is found in the distributions of the muon impact parameters and pseudo-rapidity. However, significant discrepancies between data and simulation are observed in distributions of muon transverse momenta and the $\Delta R(\mu, \mu)$ variable. It should be noted at this point that no simulated events are used for estimation of the background shapes and normalization. Instead the background is evaluated from the control data samples.

6.4 Track Selection

The analysis makes use of the reconstructed tracks [87] with highest quality, known in CMS as high purity tracks. The high purity track selection is based on:

- the χ^2/ndof of the track fit;
- transverse and longitudinal impact parameters with respect to the PV, namely d_0 and d_z;
- significance of impact parameters, $d_0/\delta d_0$ and $d_z/\delta d_z$, where δd_0 and δd_z are uncertainties on impact parameters from the track fit;
- number of tracker layers with a hit on the track;
- number of tracker "3D" layers with a hit on the track (either pixel layers or matched strip layers);
- number of layers missing hits between the first and the last hit on the track;
- $\delta p_T/p_T$ from the track fit.

Tracks must have $p_T > 1$ GeV and pseudo-rapidity $|\eta| < 2.4$. The impact parameter in the transverse plane with respect to the PV is required to be $|d_0| < 1$ cm. The longitudinal impact parameter with respect to the PV is required to be $|d_z| < 1$ cm. These loose requirements on the track impact parameters are necessitated by the definition of the muon isolation criteria described in the next Section. The isolation criteria involve tracks directly coming from the PV as well as tracks originating from decays of the heavy flavor hadrons, giving rise displaced tracks with respect to the primary interaction vertex.

6.5 Topological Selection

Two selected same-sign muons are required to be separated by $\Delta R(\mu,\mu) > 2$.

Isolation requirement: Given the search topology (Fig. 5), we require each muon to have

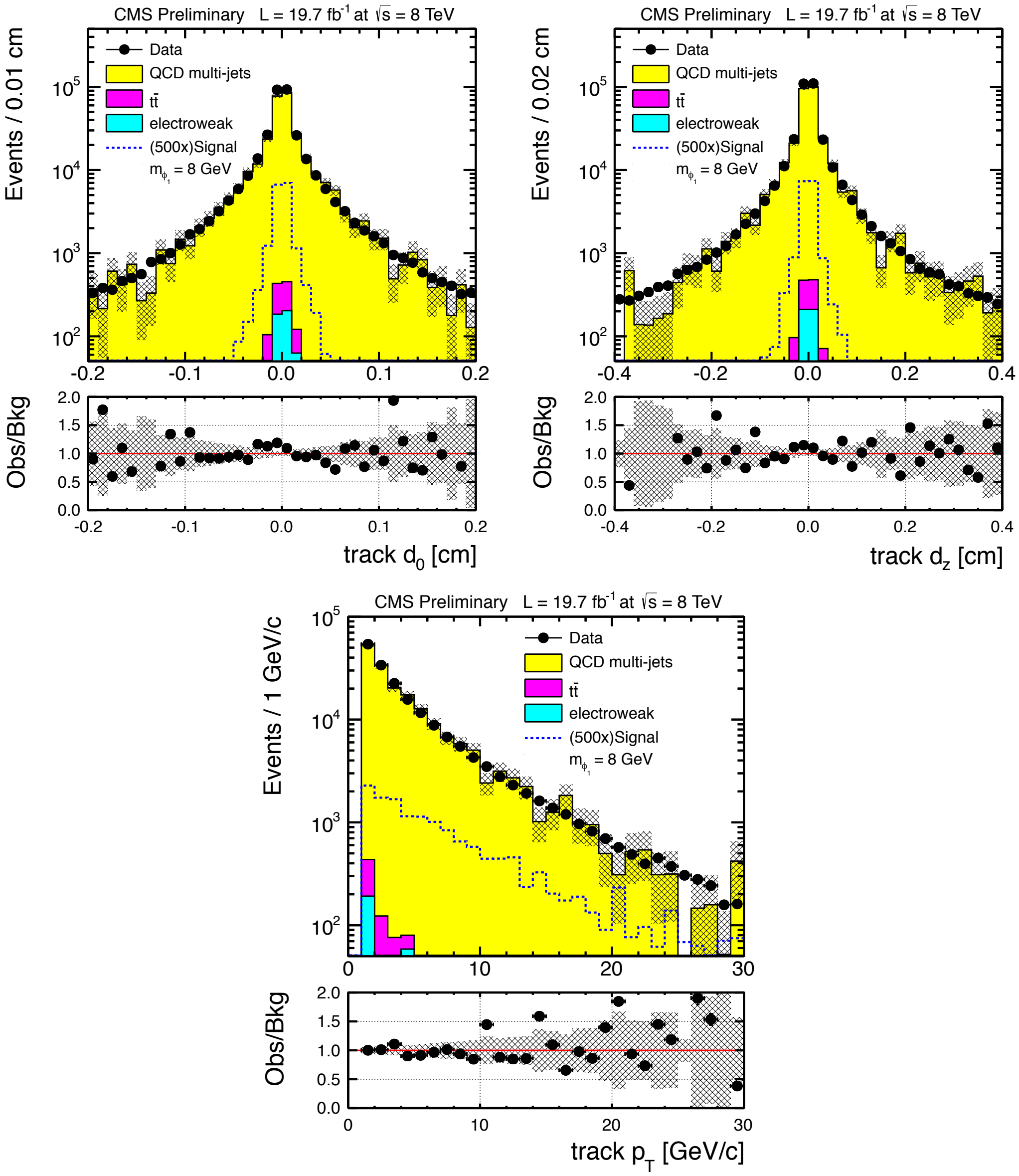

Figure 6.4: Distribution of the transverse impact parameter (upper left plot), the longitudinal impact parameter (upper right plot) and the transverse momentum (lower plot) of the tracks regarded as one-prong tau decay candidates.

only one track with momentum $p_T > 1$ GeV, pseudo-rapidity $|\eta| < 2.4$ and impact parameters $|d_0| < 1$ cm and $|d_z| < 1$ cm within a ΔR cone of 0.5 around the muon momentum.

Selection of the one-prong tau decay candidates: The single track around each muon must fulfill selection criteria imposed on the one-prong tau-lepton decay candidate:

- the net charge of track and close-by muon must be zero, $q_\mu + q_{trk} = 0$;
- track momentum has to be $p_T > 2.5$ GeV and pseudo-rapidity $|\eta| < 2.4$;
- transverse and longitudinal impact parameters of the track are required to be $|d_0| < 0.02$ cm and $|d_z| < 0.04$ cm, respectively.

With the criteria outlined above the background from the QCD multi-jet events is significantly suppressed. Figure 6.4 presents the distribution of variables used in selection of the one-prong tau-lepton decay candidates.

6.6 Muon Identification, Isolation and Trigger Efficiencies

Correction factors are applied to the simulated signal samples in order to compensate for differences in the trigger, the muon identification and the isolation efficiencies found between data and simulation. The efficiencies are estimated using a tag-and-probe technique, which is applied on the samples of di-muon events originating from the decays of Z bosons. The Z → $\mu\mu$ sample is selected with the HLT_IsoMu24 trigger.

The tag muon is required to pass the PF-Tight Muon criteria and match the HLT_IsoMu24 trigger object. The probe muons are subject to the muon identification requirements outlined in Section 6.3. Furthermore, the isolation requirement, equivalent to that used in the analysis for muon-track pairs from each ϕ_1 decay leg, is applied to the probe muons in the Z → $\mu\mu$ sample:

- there must be no tracks with $p_T > 1$ GeV and impact parameters of $d_0 < 1$ cm and $d_z < 1$ cm with respect to the PV within a ΔR cone of 0.5 around the probe muon.

The measured efficiencies of muon identification and isolation along with the scale factors applied to the simulated signal samples, are reported in Table 6.1 for different (p_T, η) bins. For the simulated samples, the simulation of the trigger response is not used. Instead, in order to account for the HLT_Mu17_Mu8 OR HLT_Mu17_TkMu8 trigger inefficiency, each simulated event is assigned with a weight:

$$\begin{aligned} V =&(\epsilon^{leg17}(p_{T_1}, \eta_1)\ .\ \epsilon^{leg8}(p_{T_2}, \eta_2) + \\ &\epsilon^{leg17}(p_{T_2}, \eta_2)\ .\ \epsilon^{leg8}(p_{T_1}, \eta_1) - \\ &\epsilon^{leg17}(p_{T_1}, \eta_1)\ .\ \epsilon^{leg17}(p_{T_2}, \eta_2)) \\ &\times\ \epsilon_{dZfilter} \end{aligned} \tag{6.1}$$

where

- $\epsilon^{leg17}(p_T, \eta) - p_T$ and η dependent efficiency of the trigger leg with p_T threshold of 17 GeV;
- $\epsilon^{leg8}(p_T, \eta) - p_T$ and η dependent efficiency of the trigger leg with p_T threshold of 8 GeV (Mu8 OR TkMu8);
- p_{T_1} and η_1 are transverse momentum and pseudo-rapidity of the first muon;

- p_{T_2} and η_2 are transverse momentum and pseudo-rapidity of the second muon;

- $\epsilon_{dZfilter}$ - efficiency of dZfilter of the double muon trigger.

Table 6.1: Muon Id and isolation efficiencies in data and MC samples derived using tag-andprobe technique, applied on the Z→ $\mu\mu$ sample. Also the data-simulation scale factors (SF) are reported.

p_T (GeV)	η	ϵ_{data}	ϵ_{MC}	SF
10-15	0-0.8	0.618	0.657	0.942
	0.8-1.6	0.697	0.716	0.973
	1.6-2.1	0.753	0.757	0.993
15-20	0-0.8	0.640	0.651	0.983
	0.8-1.6	0.686	0.718	0.956
	1.6-2.1	0.729	0.727	1.003
20-25	0-0.8	0.674	0.683	0.987
	0.8-1.6	0.708	0.727	0.974
	1.6-2.1	0.749	0.762	0.982
25-30	0-0.8	0.706	0.724	0.974
	0.8-1.6	0.722	0.733	0.984
	1.6-2.1	0.755	0.775	0.974
> 30	0-0.8	0.755	0.778	0.971
	0.8-1.6	0.762	0.781	0.975
	1.6-2.1	0.787	0.801	0.983

The trigger efficiencies as measured with the tag-and-probe technique using a sample of Z $\rightarrow$ $\mu\mu$ decays are given in Tables 6.2-6.3. The trigger efficiencies are measured relative to the offline selection while combining both the muon identification and the isolation requirements. The efficiency of the dZfilter of the HLT_Mu17_Mu8 OR

Table 6.2: HLT_Mu17_Mu8 OR HLT_Mu17_TkMu8 : efficiency of the Mu8 leg.

p_T (GeV)	$0 < \eta \leq 0.8$	$0.8 < \eta \leq 1.2$	$1.2 < \eta \leq 2.1$
10-12.5	0.96	0.97	0.92
12.5-15	0.97	0.97	0.93
15-17.5	0.98	0.97	0.94
17.5-20	0.98	0.98	0.94
20-30	0.97	0.98	0.95
>30	0.98	0.98	0.95

Table 6.3: HLT_Mu17_Mu8 OR HLT_Mu17_TkMu8 : efficiency of the Mu17 leg.

p_T (GeV)	$0 < \eta \leq 0.8$	$0.8 < \eta \leq 1.2$	$1.2 < \eta \leq 2.1$
10-12.5	0.00	0.00	0.00
12.5-15	0.00	0.02	0.01
15-17.5	0.24	0.22	0.23
17.5-20	0.96	0.93	0.91
20-30	0.97	0.94	0.92
>30	0.96	0.93	0.92

HLT_Mu17_TkMu8 trigger is measured to be 95%.

6.7 Higgs p_T Reweighting

As it has been already elaborated in chapter 4(section 4.2), Pythia was used for the generation of the signal samples which provides the leading order diagrams and cross section for the processes of interest. However, in order to account for NNLO and NNLL effects that may affect the signal acceptance, the p_T spectrum has been reweighted with the use of the HqT code [29,30].

The purpose is to assign a unique weight on the initial p_T spectrum from Pythia per bin i:

$$W^i_{bin} = \frac{(\mathrm{HqT})^i_{bin}}{(\mathrm{Pythia})^i_{bin}} \tag{6.2}$$

In the case of the HqT the above procedure has been repeated for a different choice of the factorization and the normalization scales. The nominal scale thereafter denotes the scale where the factorization and the normalization scales are set equal to the Higgs boson mass (125 GeV), while Scale-Up and Scale-Down refer to twice and half the Higgs boson mass respectively. Further, in order to assess the contribution of b-loop diagrams on the signal acceptance, the above mentioned workflow was exercised with a dedicated PowHeg (b-loop) dataset but only for the nominal scale. Figure 6.5 shows the obtained weights of the p_T distribution for the range 0 to 300 GeV obtained from the HqT. Above 300 GeV a weight of unity has been assigned. Further, Figure 6.6 overlays the p_T spectrum obtained from Pythia before and after the reweighting for the different considered scales for both HqT and PowHeg (b-loop).

Finally, the effect of the reweighting procedure as described above has been obtained for the two masses of the signal considered in this analysis and is summarized in Table 6.4. As it can be seen, the effect is rather small at the level of few percent.

Figure 6.5: The weights distribution for the p_T spectrum of the Higgs with the use of the HqT code for the nominal (left), Scale-Up (middle) and the Scale-Down (right). The nominal scale is defined when the factorization and the normalization scales are set equal to the Higgs mass (125 GeV) while Scale-Up (Scale-Down) when the factorization and the normalization scale is set equal to two (half) times the Higgs mass.

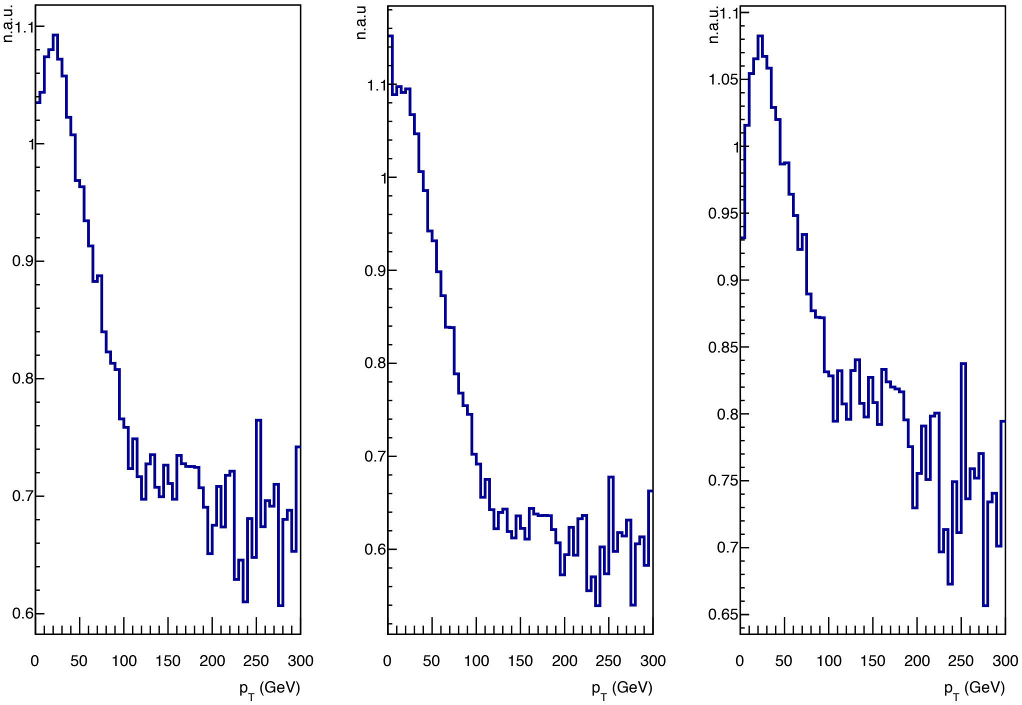

Table 6.4: Signal acceptances of the two considered light Higgs masses (4 and 8 GeV) for the unweighted and the weighted p_T spectrum of the nominal (for both HqT and PowHeg(b-loop)), Scale-Up and Scale-Down cases.

Quantity	Signal Acceptance	
	m_{ϕ_1} = **4 GeV**	m_{ϕ_1} = **8 GeV**
no p_T Reweighing	$(5.28 \pm 0.22) \times 10^{-4}$	$(3.05 \pm 0.18) \times 10^{-4}$
Nominal scale (HqT)	$(5.38 \pm 0.23) \times 10^{-4}$	$(3.13 \pm 0.18) \times 10^{-4}$
Nominal scale (PowHeg(b-loop))	$(5.55 \pm 0.23) \times 10^{-4}$	$(3.20 \pm 0.18) \times 10^{-4}$
Scale up	$(5.41 \pm 0.23) \times 10^{-4}$	$(3.16 \pm 0.18) \times 10^{-4}$
Scale down	$(5.35 \pm 0.23) \times 10^{-4}$	$(3.09 \pm 0.18) \times 10^{-4}$

Figure 6.6: The p_T spectrum in both linear (left) and log scale (right) of the Higgs before (dashed) and after been reweighted with the use of the HqT and PowHeg(b-loop) samples (full lines). Nominal refers to the case where the factorization and normalization scales are set equal to the Higgs mass, while Scale-Up (Scale-Down) when the factorization and the normalization scale is set equal to two (half) times the Higgs mass as explained in the text.

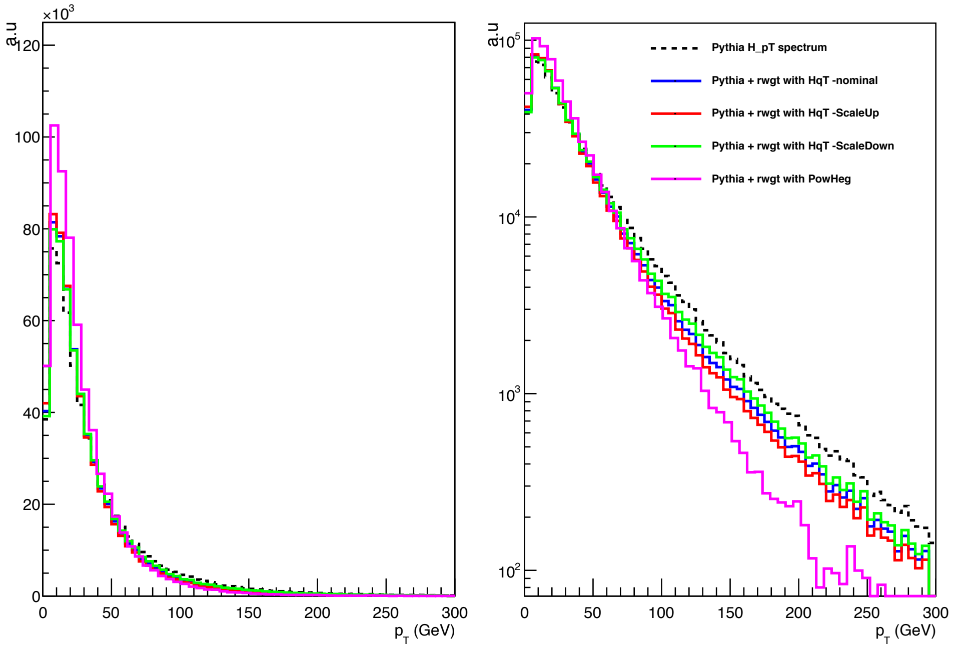

Chapter 7

Signal Extraction and Modeling of QCD Background

7.1 Signal Extraction

The set of selection requirements outlined in chapter 6 defines the signal region, which will be used to extract the signal. The number of data events, expected background events selected in the signal region, as well as signal acceptance are reported in Table 7.1. The expected background and signal yields, along with the signal acceptances, are obtained from simulation. The signal yields are normalized to the benchmark value of the signal production cross section times branching fraction of 5 pb. The quoted uncertainties in predictions from simulation include only MC statistical uncertainties. Thus, since the expected signal yield is comparable with the statistical uncertainty on the number of selected data events, a simple counting experiment will have limited sensitivity to any potential signal. The expected background yields presented in Table 6.4 show that the final selected sample is dominated by QCD multijet events, and that the contribution from other background sources is negligible, constituting less than 1% of all selected events. Although MC simulation is not directly used to estimate background, the simulated samples play an important role in the validation of the background modelling as described in Section 6. The signal acceptances are computed with respect to all possible decays of the four τ leptons i.e. we assume the $\mathrm{B}(\phi \to \tau\tau) = 100\%$, and include a branching fraction factor,

$$\frac{1}{2}\mathcal{B}^2(\phi_1 \to \tau_\mu \tau_{\mathrm{one-prong}}) \approx 3.5\% \tag{7.1}$$

where the factor 1/2 accounts for the selection of same-sign muon pairs, and

$\mathcal{B}(\phi_1 \to \tau_\mu \tau_{\mathrm{one-prong}})$ denotes the branching fraction of the $\phi_1 \to \tau\tau$ decays to the final states characterized by the presence of only two charged particles where at least one of the charged particles is a muon.

This branching fraction is expressed as,

$$\mathcal{B}(\phi_1 \to \tau_\mu \tau_{\mathrm{one-prong}}) = 2\mathcal{B}(\tau \to 1\mathrm{one-prong})\mathcal{B}(\tau \to \mu\nu\bar{\nu}) - \mathcal{B}^2(\tau \to \mu\nu\bar{\nu}) \tag{7.2}$$

where $\mathcal{B}(\tau \to \mathrm{one-prong})$ denotes the total branching fraction of the τ decay to one charged particle with any number of neutral particles. The factor of two in the first term accounts for the two possible charges of the required muonic decay: $\tau^-\tau^+ \to \mu^- + \mathrm{one-prong}^+$ and $\tau^-\tau^+ \to \mu^+ + \mathrm{one-prong}^-$. Subtraction of the term $\mathcal{B}^2(\tau \to \mu\nu\bar{\nu})$ avoids double counting

Table 7.1: The number of data events, expected background and signal events and signal acceptance after final selection. Signal acceptance includes branching ratio factor $\mathcal{B}^2(\tau \rightarrow \mu\nu\bar{\nu}).(2\mathcal{B}(\tau \rightarrow \text{one-prong}) - \mathcal{B}(\tau \rightarrow \mu\nu\bar{\nu}))^2 \approx 7\%$, as well as a factor of 1/2 due to the selection of same-sign muon pairs. Electroweak background includes Drell-Yan process, W + Jets events and di-boson production, WW, WZ and ZZ. The number of signal events is reported for the signal cross section times branching ratio of 5 pb. The quoted uncertainties for predictions from simulation include only statistical errors.

Sample	**Number of events**
Data	873
Expected background events	
QCD multi-jets	820 ± 320
$t\bar{t}$	1.2 ± 0.2
Electroweak	5.0 ± 4.7
Signal Acceptance, A(gg $\rightarrow$ H(125) $\rightarrow \phi_1\phi_1 \rightarrow 4\tau$)	
$m_{\phi_1} = 4$ GeV	$(5.38 \pm 0.23).10^{-4}$
$m_{\phi_1} = 5$ GeV	$(4.36 \pm 0.21).10^{-4}$
$m_{\phi_1} = 6$ GeV	$(4.00 \pm 0.23).10^{-4}$
$m_{\phi_1} = 7$ GeV	$(4.04 \pm 0.20).10^{-4}$
$m_{\phi_1} = 8$ GeV	$(3.13 \pm 0.18).10^{-4}$
Number of signal events for σ(gg $\rightarrow$ H(125)).$\mathcal{B}$(H(125) $\rightarrow \phi_1\phi_1$).$\mathcal{B}^2(\phi_1 \rightarrow \tau\tau)$ = 5 pb	
$m_{\phi_1} = 4$ GeV	$(53.0 \pm 2.3).10^{-4}$
$m_{\phi_1} = 5$ GeV	$(43.0 \pm 2.0).10^{-4}$
$m_{\phi_1} = 6$ GeV	$(39.5 \pm 2.0).10^{-4}$
$m_{\phi_1} = 7$ GeV	$(39.9 \pm 2.0).10^{-4}$
$m_{\phi_1} = 8$ GeV	$(30.8 \pm 1.8).10^{-4}$

in the case where the two τ leptons produced by a given ϕ_1 both decay to muons.

The invariant mass of each selected muon and the nearby track is reconstructed. The two dimensional distribution of the invariant mass of each selected muon and the nearby track is used to discriminate between the signal and the QCD multijet background; the signal is extracted by means of a fit to this two-dimensional distribution. The binning of the two dimensional (m_1, m_2) distributions is illustrated in Fig. 7.1. For masses below 3 GeV, bins of 1 GeV width are used for both m_1 and m_2. For masses in the range $3 < m_1(m_2) < 10$ GeV, a single bin is used. This choice avoids poorly populated bins in the two-dimensional (m_1, m_2) distributions in the background control regions used to construct and validate the QCD multijet background model (Section 6). For each selected event, the (m_1, m_2) histogram is filled once if the pair of quantities (m_1, m_2) occurs in one of the diagonal bins and twice, once with values (m_1, m_2) and a second time with the swapped values (m_1, m_2), for off-diagonal bins. This procedure insures the symmetry of the two-dimensional (m_1, m_2) distribution. To avoid double counting of events, the off-diagonal bins (i, j) with $i > j$ are excluded from the procedure of the signal extraction. Thus, the number of independent bins is reduced from $4\times4 = 16$ to $4\times(4 + 1)/2 = 10$.

In order to fit the data in the 10 bins of the two-dimensional distribution of Fig. 7.1, a two component fit is performed using two-dimensional distributions ("templates") describing the QCD multijet background and the signal. The normalizations of background and signal components are free parameters in this fit. The two-dimensional template for the signal is obtained from the simulation using the generator described in chapter 4. The two-dimensional template for the QCD multijet background is extracted from the data as explained in the next section.

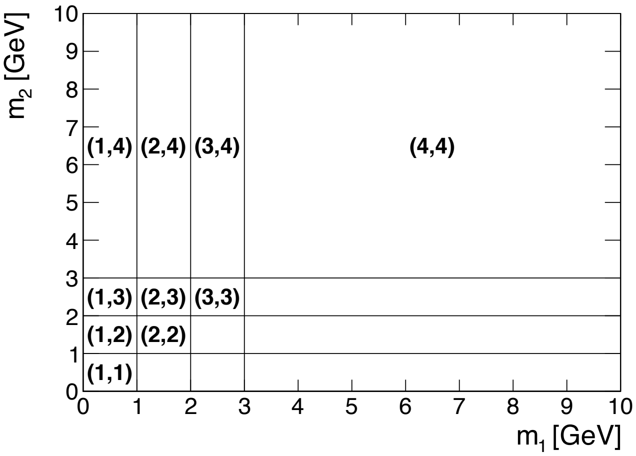

Figure 7.1: Binning of the two-dimensional (m_1, m_2) distribution with the off-diagonal bins excluded in the statistical analysis.

7.2 Modelling of the QCD multijet background shape

A simulation study shows that the sample of same-sign dimuon events selected as described in Section 4, but without requiring a presence of one-prong τ candidates and without applying the isolation requirement for the muon-track systems, is dominated by QCD multijet production, where 94% of all selected events contain b quarks in the final state. The same-sign muon pairs in these events originate mainly in the following sources:

- Muonic decay of a bottom hadron in one b-quark jet, and cascade decay of a bottom hadron into a charmed hadron with subsequent muonic decay of a charmed hadron in the other b-quark jet.
- Muonic decay of a bottom hadron in one b-quark jet, and decay of a quarkonium state into a pair of muons in the other jet.
- Muonic decay of a bottom hadron in one b-quark jet, and muonic decay of a neutral

B meson in the other b-quark jet. The same-sign muon pair in this case may appear as a result of $\mathrm{B}^0 - \bar{\mathrm{B}}^0$ oscillations.

The normalization of the QCD multijet background is not constrained prior to the extraction of the signal. The procedure used to model the shape of the two-dimensional (m_1, m_2) distribution of QCD multijet events in the signal region is described in this section. Given the symmetry of the two-dimensional (m_1, m_2) distribution, the modelling of the QCD multijet background shape is derived from the two-dimensional probability density function (pdf),

$$f_{2D}(m_1, m_2) = C(m_1, m_2) f_{1D}(m_1) f_{1D}(m_2) \tag{7.3}$$

where:

- $f_{2D}(m_1, m_2)$ is the normalized two-dimensional distribution of the muon-track pair invariant masses, m_1 and m_2, in the sample of QCD background events selected in the signal region;
- $f_{1D}(m_i)$ is the normalized one-dimensional distribution of the muon-track pair in the sample of QCD background events selected in the signal region;
- $C(m_1, m_2)$ is a symmetric function of 2 arguments, $C(m_1, m_2) = C(m_2, m_1)$, reflecting correlation between masses m_1 and m_2.

A constant correlation function would indicate the absence of correlation between m_1 and m_2. Based on Eq. 7.3, the content of bin (i, j) of the symmetric normalized two-dimensional distribution $f_{2D}(m_1, m_2)$ is computed as

$$f_{2D}(i,j) = C(i,j)\ f_{1D}(i)\ f_{1D}(j) \tag{7.4}$$

where:

- $C(i,j)$ is the correlation coefficient in the bin (i,j) of the correlation function $C(m_1, m_2)$;
- $f_{1D}(i)$ is the content of bin i in the normalized one-dimensional distribution $f_{1D}(m_i)$.

The modelling of $f_{1D}(m)$ and $C(m_1, m_2)$, is necessary in order to build the template $f_{2D}(i,j)$ and is described in the following sections.

7.2.1 Modelling of $f_{1D}(m)$

The $f_{1D}(m)$ pdf is modelled using a QCD-enriched control data sample disjoint from the signal region. Events in the control sample are required to satisfy all selection criteria, except for the isolation of the second muon-track system. The second muon is required to be accompanied by either two or three nearby tracks with $p_T > 1$ GeV and impact parameters smaller than 1 cm relative to the PV both in the transverse plane and along the beam axis. The simulation shows that more than 99% of events selected in this control region, hereafter referred to as N_{23}, are QCD multijet events. The modelling of the $f_{1D}(m)$ pdf is based on the assumption that the kinematic distributions for the first muon-track system are not affected by the isolation requirement imposed on the second, and therefore the $f_{1D}(m)$ pdf of the isolated muon-track system is the same in the signal region and the region N_{23}. A direct test of this assumption, given the limited size of the simulated sample of QCD multijet events, is not conclusive, and a test is therefore performed with an additional control sample. Events are selected in this control sample if one of the muons has at least one track passing the one-prong τ decay candidate criteria within a ΔR cone of radius 0.5 around the muon direction, with any number of additional tracks within the same ΔR cone. As more than one of these tracks can pass the selection criteria for a one-prong τ decay candidate, we investigate two scenarios. In one scenario, the lowest p_T ("softest") track passing the one-prong τ decay candidate criteria is used to calculate the muon-track invariant mass,while in the other scenario the highest p_T ("hardest") track passing the one-prong τ decay candidate criteria is used. If only one τ track is found around the first muon, the track is regarded as both "hardest" and "softest". For the second muon, two isolation requirements are considered: when the muon is accompanied by only one track passing the one-prong τ decay candidate criteria ($N_{trk,2} = 1$) as in the signal region, or when it is accompanied by two or three tracks ($N_{trk,2} = 2,\ 3$) with $p_T > 1$GeV and impact parameters smaller than 1 cm relative to the PV as in the region N_{23}. The shapes of invariant mass distributions of the first muon and the softest or hardest accompanying track are then compared for the two different isolation requirements on the second muon, $N_{trk,2}$ $= 1$ and $N_{trk,2} = 2,\ 3$. The test is performed both on data and on the simulated sample of QCD multijet events. The results of this study for 8 TeV and 13 TeV data are illustrated in Fig. 7.2 and Fig. 7.3 respectively. In all considered cases, the shape of the invariant mass distribution is compatible within statistical uncertainties between the two cases, $N_{trk,2} =$ 1 and $N_{trk,2} = 2,\ 3$. This observation validates the assumption that the $f_{1D}(m)$ pdf can be determined in the control region N_{23}. Fig. 7.4 presents the normalized invariant mass distribution of the muon-track system for data selected in the signal region, and for the QCD multijet background model derived from the control region N_{23}. The data and QCD multijet background distributions are compared to the signal distribution normalized to unity (signal pdf), obtained from simulation, for two representative mass hypotheses, $m_{\phi_1} = 4$ and 8 GeV. The invariant mass of the muon-track system is found to have high discrimination power between the QCD multijet background and signal at $m_{\phi_1} = 8$ GeV. At smaller m_{ϕ_1} the signal shape becomes more similar to the background shape, resulting in a reduction of discrimination power. The normalized distribution $f_{1D}(i)$ with the binning defined in Fig. 7.1 is extracted from the background distribution shown in Fig. 7.4.

7.2.2 Modeling of $C(m_1, m_2)$

In order to determine the correlation coefficients $C(i, j)$ we define an additional control region A enriched in QCD multijet events. This control region consists of events that contain two same-sign muons passing the identification and kinematic selection criteria outlined in chapter. Each muon is required to have two or three nearby tracks within a ΔR cone of radius 0.5 around the muon direction. One and only one of these tracks must satisfy the criteria imposed on one-prong τ lepton decay candidates with $p_T > 2.5$ GeV. The additional tracks must have transverse momentum in the range $1 < p_T < 2.5$ GeV. A total of 9127 data events are selected in this control region. The MC simulation predicts that the QCD multijet background dominates in region A, comprising more than 99% of all selected events. The simulation study also shows that the overall background-to-signal ratio is enhanced compared to the signal region by a factor of 15 to 20, depending on the mass hypothesis m_{ϕ_1}. Despite the large increase in the overall background-to-signal ratio, potential signal contamination in individual bins of the mass distributions can be non negligible. Bin-by-bin signal contamination in region A is discussed in Section 7.3. For each event in control region A, the pair (m_1, m_2) of muon-track invariant masses is calculated. This pair is used to build the symmetrized normalized two-dimensional distribution $f_{2D}(i, j)$ defined in Fig. 7.1. Then $C(i, j)$ is obtained according to Eq. (7.4) as,

$$C(i, j) = \frac{f_{2D}(i, j)}{f_{1D}(i)\ f_{1D}(j)} \tag{7.5}$$

where $f_{1D}(i)$ is the one-dimensional normalized distribution with two entries per event (m_1 and m_2) built as in Fig. 4 using 8 TeV data. Correlation coefficients $C(i, j)$ derived from data in region A are presented in Fig. 7.5. The correlation coefficients have been derived using 13 TeV data as well and are shown in Fig. 7.6. The results are similar to that for 8 TeV. A direct comparison of $C(i, j)$ between the signal region and region A would be impossible in the simulated sample of QCD multijet events because of the very small numbers of events selected in the signal region and in region A. In order to assess the difference in $C(i, j)$ between the signal region and region A, a dedicated MC study is performed, making use of a large exclusive sample generated with PYTHIA. The simulation includes only two leading-order QCD multijet production mechanisms: the creation of a $\mathrm{b\bar{b}}$ quark pair via $\mathrm{gg} \to \mathrm{b\bar{b}}$ and $\mathrm{q\bar{q}} \to \mathrm{b\bar{b}}$. The detector simulation and event reconstruction are not performed for this sample, and the comparison of $C(i, j)$ between the signal region and region A is made using generator-level quantities. These simplifications are validated by performing a set of

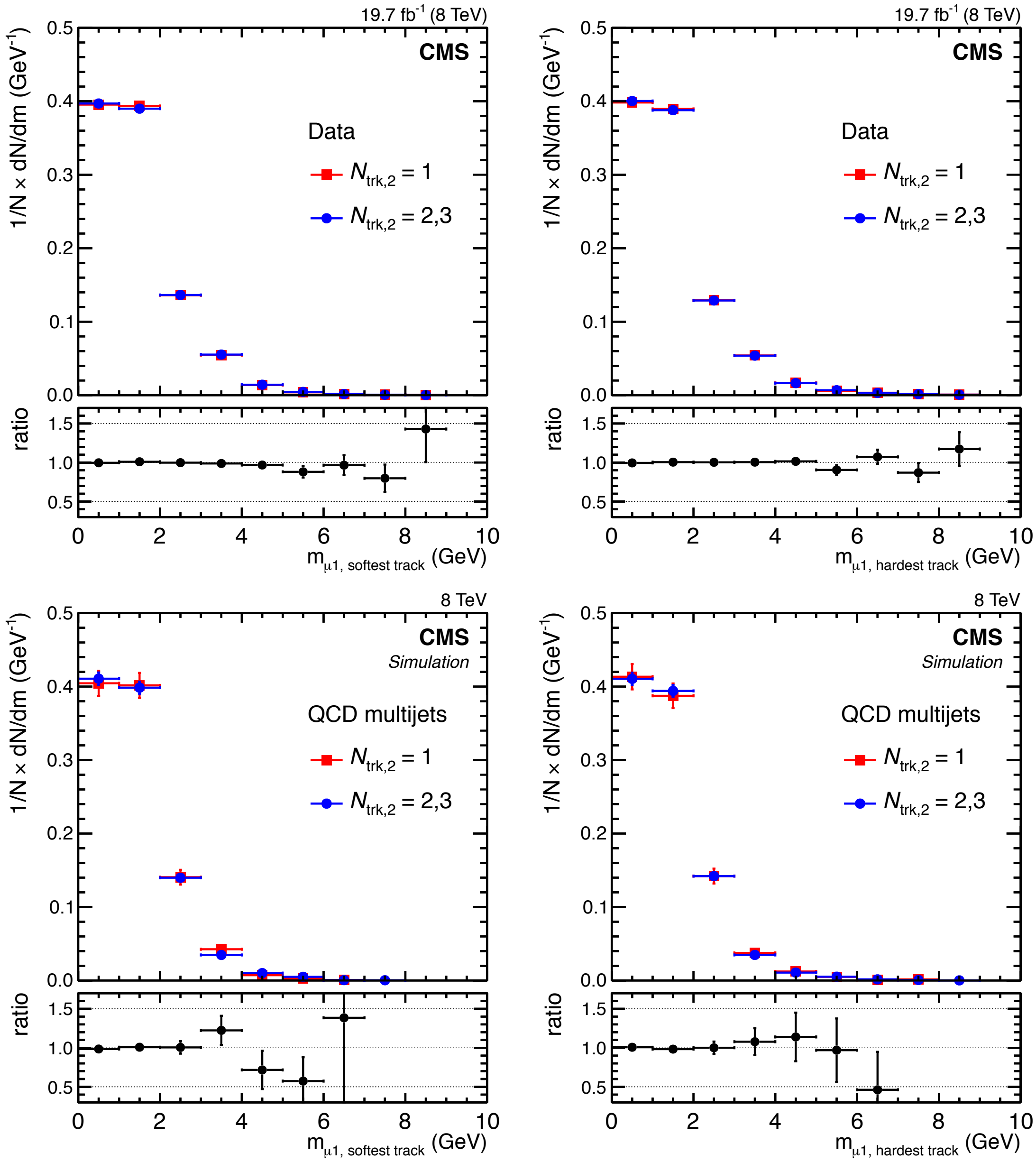

Figure 7.2: Normalized invariant mass distributions of the first muon and the softest (left plots) or hardest (right plots) accompanying track for different isolation requirements imposed on the second muon: when the second muon has only one accompanying track ($N_{trk,2}$ = 1; squares); or when the second muon has two or three accompanying tracks ($N_{trk,2}$ = 2, 3; circles). The upper plots show distributions obtained from data. The lower plots show distributions obtained from the sample of QCD multijet events generated with PYTHIA. Lower panels in each plot show the ratio of the $N_{trk,2} = 1$ distribution to the $N_{trk,2} = 2$, 3 distribution.

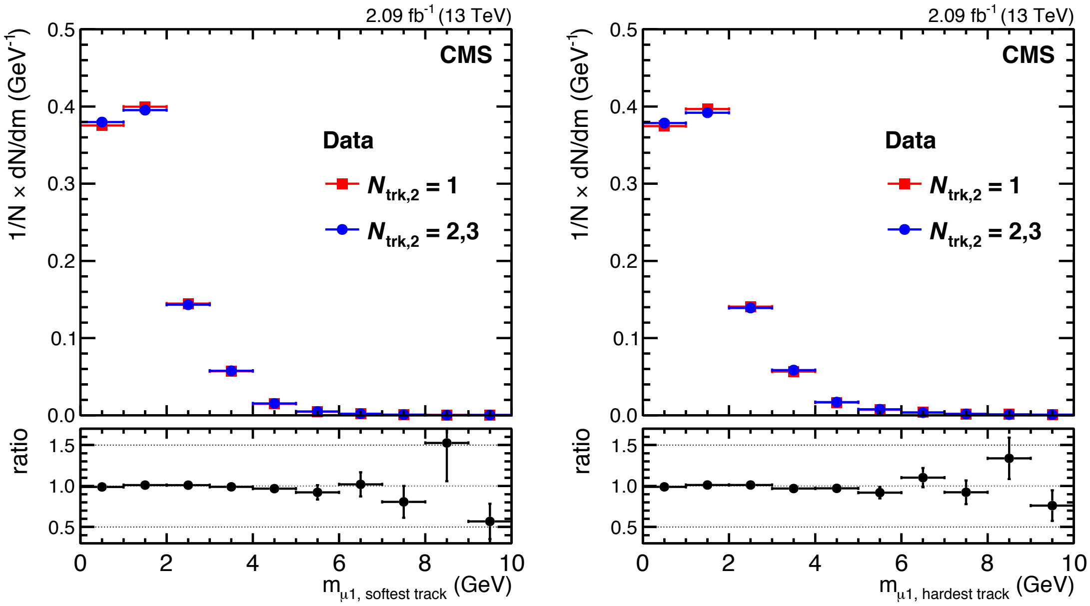

Figure 7.3: Normalized invariant mass distributions of the first muon and the softest (left plots) or hardest (right plots) accompanying track for different isolation requirements imposed on the second muon: when the second muon has only one accompanying track ($N_{trk,2}$ $= 1$; squares); or when the second muon has two or three accompanying tracks ($N_{trk,2}$ $=$ 2, 3; circles).

consistency tests, making use of the available MC sample of QCD multijet events processed through the full detector simulation and event reconstruction. These tests are performed in a control region B, where each muon is required to have at least one track passing the one-prong τ decay candidate selection criteria, i.e. with $p_T > 2.5$ GeV and impact parameters smaller than 200 μm and 400 μm in the transverse plane and along beam axis, respectively. Along with this requirement each muon is allowed to have one or more tracks within a ΔR cone of radius 0.5 around the muon direction, with $p_T > 1$ GeV and impact parameters smaller than 1 cm. Control region B is characterized by a significantly larger yield of QCD multijet events compared to the signal region and control region A, thus making it possible to perform reliable MC consistency tests and assess the uncertainties in $C(i, j)$.

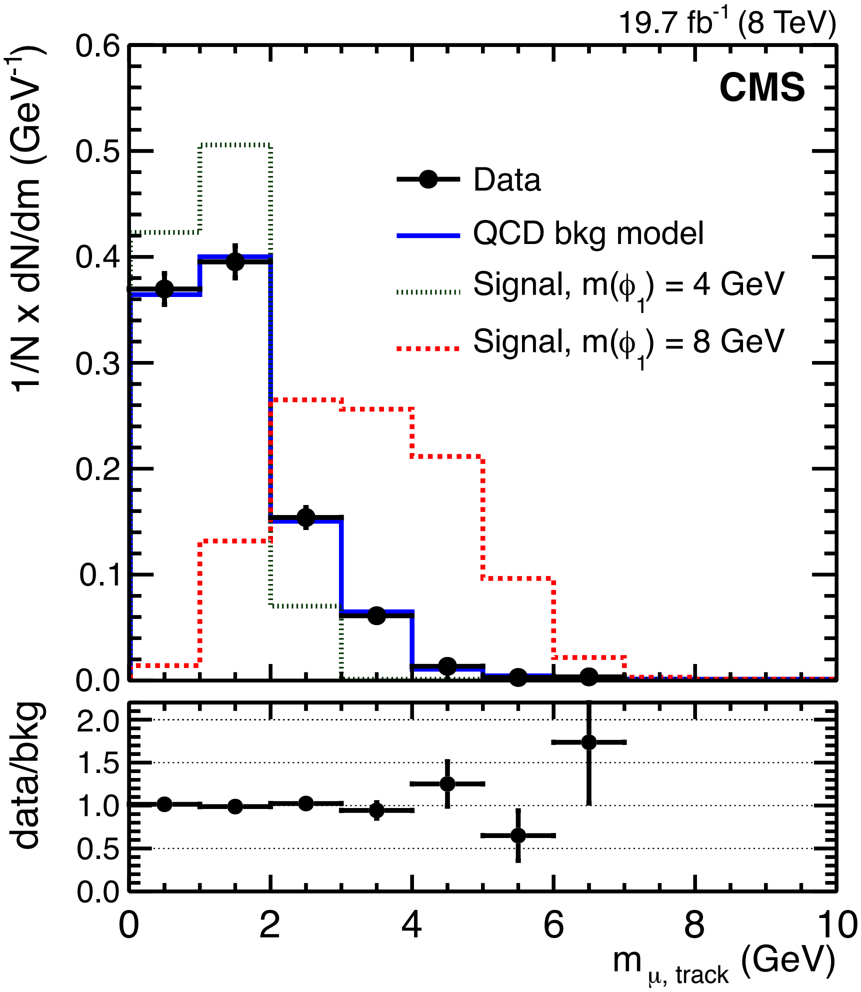

Figure 7.4: Normalized invariant mass distribution of the muon-track system for events passing the signal selection. Data are represented by points. The QCD multijet background model is derived from the control region N_{23}. Also shown are the normalized distributions from signal simulations for two mass hypotheses, $m_{\phi_1} = 4$ GeV (dotted histogram) and 8 GeV (dashed histogram). Each event contributes two entries to the distribution, corresponding to the two muon-track systems passing the selection requirements. The lower panel shows the ratio of the distribution observed in data to the distribution, describing the background model.

Two scenarios are investigated: 1) muons are paired with the softest one-prong τ decay candidate and 2) muons are paired with the hardest one-prong τ decay candidate. If only one one-prong τ decay candidate is found around a muon, it is regarded as both "softest" and

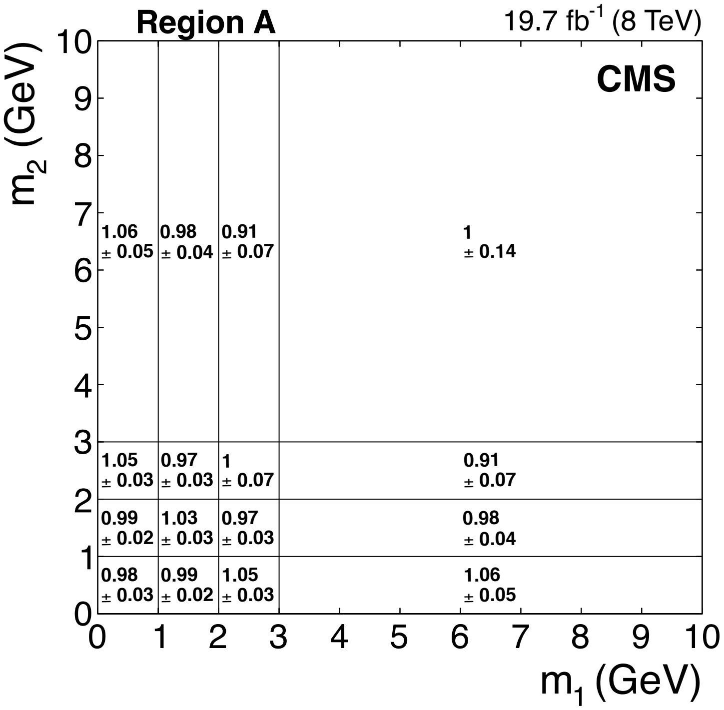

Figure 7.5: The (m_1, m_2) correlation coefficients $C(i,j)$ along with their statistical uncertainties, derived from 8 TeV data in the control region A.

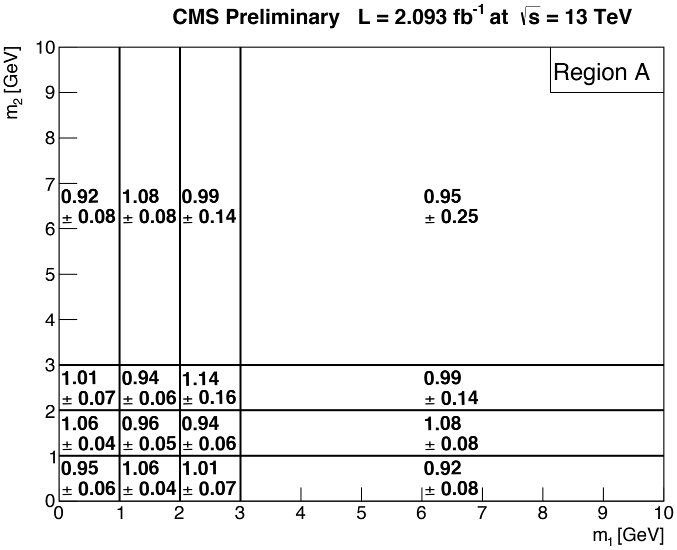

Figure 7.6: The (m_1, m_2) correlation coefficients $C(i,j)$ along with their statistical uncertainties, derived from 13 TeV data in the control region A.

"hardest". In both scenarios the correlation coefficients computed using the reconstructed four-momenta of muons and tracks are found to be compatible with those computed using generator-level four-momenta, within statistical uncertainties. Furthermore, the correlation coefficients computed with the inclusive QCD multijet sample are found to be compatible with those computed in the exclusive MC sample including only the $\mathrm{gg}(\mathrm{q\bar{q}}) \rightarrow \mathrm{b\bar{b}}$ production mechanisms. This observation validates the use of the generator-level information and the exclusive $\mathrm{b\bar{b}}$ MC sample to compare $C(i, j)$ between the signal region and control region A. This comparison is presented in Fig. 7.7. The uncertainties in $C(i, j)$ represent a quadratic sum of the systematic and MC statistical uncertainties. The systematic uncertainties are derived from the control region B.

They take into account 1) any differences in $C(i, j)$ calculated using the inclusive QCD multijet sample compared with the exclusive $\mathrm{b\bar{b}}$ sample and 2) any differences in $C(i, j)$ calculated using full detector simulation and event reconstruction compared with the study using generator-level quantities. Within their uncertainties the correlation coefficients $C(i, j)$ in the signal region and in region A are compatible. We therefore use $C(i, j)$ derived from data in region A to predict the QCD multijet background shape in the signal region according to Eq. 7.4.

7.3 Systematic uncertainties

The analysis is affected by various systematic uncertainties,which are classified into two groups. The first group consists of uncertainties related to the background, while the second group includes uncertainties related to the signal. The systematic uncertainties are

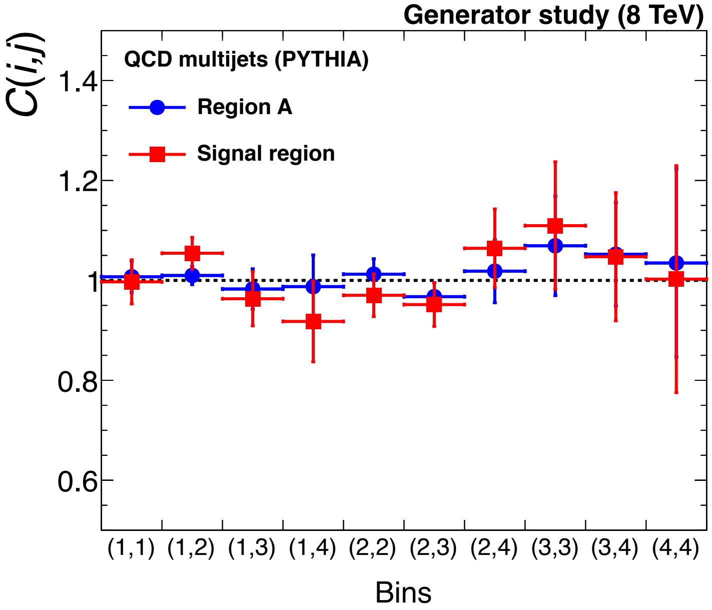

Figure 7.7: The (m_1, m_2) correlation coefficients $C(i,j)$ determined in the control region A (circles) and in the signal region (squares) from the MC study carried out at generator level with the exclusive MC sample of QCD multijet events resulting from $gg(q\bar{q}) \rightarrow b\bar{b}$ production mechanisms. The bin notation follows the definition presented in Fig. 7.1. The vertical bars include both statistical and systematic uncertainties.

summarized in Table 2.

7.3.1 Uncertainties related to background

The estimation of the QCD multijet background is based solely on data and is therefore not affected by imperfections in the simulation of the detector response and inaccuracies in the modelling of the muon and track reconstruction. The shape of the background in the two-dimensional (m_1, m_2) distribution is modelled according to Eq. 7.4. The uncertainty in the two-dimensional shape $f_{2D}(m_1, m_2)$ is dominated by uncertainties in the correlation coefficients $C(i,j)$ derived in the QCD multijet background enriched control region A as described in Section 7.2. The statistical uncertainties in $C(i,j)$ in region A range from 2 to 14%, as seen in Fig. 7.5. These uncertainties are accounted for in the signal extraction procedure by 10 independent nuisance parameters, one nuisance parameter per bin in the (m_1, m_2) distribution. The systematic uncertainties related to the extrapolation of $C(i,j)$ from the control region A to the signal region are derived from the dedicated MC study. The correlation coefficients are found to be compatible between the signal region and the control region A within uncertainties ranging from 2 to 22% (Fig. 7.7). These uncertainties are accounted for by 10 additional independent nuisance parameters.

The possible contamination of control region A by the signal may bias the estimation of the correlation coefficients and consequently have an impact on the evaluation of the QCD multijet background. The effect is estimated with a conservative assumption on the branching fraction $\mathcal{B}(\mathrm{H}(125) \to \phi_1\phi_1)\mathcal{B}^2(\phi_1 \to \tau\tau)$ of 32%, which corresponds to the 95% confidence level (CL) upper limit set by CMS on the branching fraction of the H(125) boson decays to non-standard model particles [35], while the cross section for gluon-gluon fusion is set to the value predicted in the standard model (19.3 pb). Under these assumptions, the contamination of region A by the signal is estimated to be less than 2% for all mass hypotheses m_{ϕ_1} and in all bins of the two dimensional (m_1, m_2) distribution, with the exception of bin (4,4), where the contamination can reach 12% for $m_{\phi_1} = 8$ GeV. However, the overall effect on the signal extraction is found to be marginal. Within this conservative scenario, variations of $C(i,j)$ due to possible contamination of control region A by the signal modify the observed and expected upper limits at 95% CL on $(\sigma\mathcal{B})_{\mathrm{sig}}$ by less than 1% for all considered values of m_{ϕ_1}.

7.3.2 Uncertainties related to signal

The following uncertainties in the signal estimate are taken into account, and are summarized in Table 7.2. An uncertainty of 2.6% is assigned to the integrated luminosity estimate [91]. The uncertainty in the muon identification and trigger efficiency is estimated to be 2% using the tag-and-probe technique applied to a sample of Z $\rightarrow \mu\mu$ decays. Because final states with two muons are selected in this analysis, this uncertainty translates into a 4% systematic uncertainty in the signal acceptance. The track selection and isolation efficiency is assessed with a study performed on a sample of Z bosons decaying into a pair of τ leptons. In the selected Z $\rightarrow \tau\tau$ events, one τ lepton is identified via its muonic decay, while

Table 7.2: List of systematics uncertainties and their effect on estimates of the QCD multijet background and signal.

Source	Value	Affected sample	Type	Effect on the total yield
Statistical Uncertainties in $C(i,j)$	2–14 %	bkg.	bin-by-bin	—
Extrapolation Uncertainties in $C(i,j)$	2–22 %	bkg.	bin-by-bin	—
Integrated Luminosity	2.6%	signal	norm	2.6%
Muon ID and trigger efficiency	2 % per muon	signal	norm.	4 %
Track selection and isolation efficiency	5 % per track	signal	norm.	10 %
MC statistical uncertainties	2–100 %	signal	bin-by-bin	4–6 %
Theory uncertainties in the signal acceptance				
μ_r and μ_f variations	1%	signal	norm	1%
PDF	1%	signal	norm	1%
Effect of b-quark loop contribution to gg $\rightarrow$ H(125)	3%	signal	norm	3%

the other is identified as an isolated track resulting from a one-prong decay. The track is required to pass the nominal selection criteria used in the main analysis. From this study the uncertainty in the track selection and isolation efficiency is estimated to be 5%. As the analysis requires each muon to be accompanied by one track, this uncertainty gives rise to a 10% systematic uncertainty in the signal acceptance. The muon momentum and track momentum scale uncertainties are smaller than 0.5% and have a negligible effect on the analysis. The bin-by-bin MC statistical uncertainties in the signal acceptance range from 7 to 100%. Their impact on the signal normalization is between 4 and 6% as indicated in Table 7.1. These uncertainties are accounted for in the signal extraction procedure by 10 nuisance parameters, corresponding to 10 independent bins in the (m_1, m_2) distribution.

Theoretical uncertainties have an impact on the differential kinematic distributions of the produced H(125) boson, in particular its p_T spectrum, thereby affecting signal acceptance. The uncertainty due to missing higher-order corrections to the gluon-gluon fusion process are estimated with the HQT program by varying the renormalization (μ_r) and factorization (μ_f) scales. The H(125) p_T-dependent k factors are recomputed according to these variations and applied to the simulated signal samples. The resulting effect on the signal acceptance is estimated to be of the order of 1%. The HQT program is also used to evaluate the effect of the PDF uncertainties. The nominal k factors for the H(125) boson p_T spectrum are computed with the MSTW2008nnlo PDF set [92]. Variations of the MSTW2008nnlo PDFs within their uncertainties change the signal acceptance by about 1%, whilst using the CTEQ6L1 PDF set changes the signal acceptance by about 0.7%. These variations are covered by the assigned uncertainty of 1%. The contribution of b-quark loops to the gluon-gluon fusion process depends on the NMSSM parameters, in particular tan β, the ratio of the vacuum expectation values of the two NMSSM Higgs doublets. The corresponding uncertainty is conservatively estimated by calculating k-factors for the H(125) boson p_T spectrum with POWHEG [93–96], removing any contribution from the top quark loop and retaining only the contribution from the b-quark loop. The modified k-factors applied to the simulated signal samples change the signal acceptance by approximately 3% for all mass hypotheses m_{ϕ_1}.

Chapter 8

Results

The signal is extracted with a binned maximum-likelihood fit applied to the two-dimensional (m_1, m_2) distribution in data. For eachmass hypothesis of the ϕ_1 boson, the (m_1, m_2) distribution in data is fitted with the QCD multijet background shape and the gg → H(125) signal shape for the ϕ_1 mass under test. The contribution to the final selected sample from vector boson fusion and vector boson associated production of the H(125) boson is suppressed by the selection described in chapter 6, i.e. by the requirement $\Delta R(\mu, \mu) > 2$. The impact of other backgrounds on the fit is found to be negligible. The signal shapes are derived from simulation. The background shape is evaluated from data, as described in chapter 7. The systematic uncertainties are accounted for in the fit via nuisance parameters with log-normal pdfs. The contribution to the final selected sample from vector boson fusion (qqh) and vector boson associated production (Vh) of the H(125) boson is suppressed by the selection described in chapter 6, especially by the requirement $\Delta R(\mu, \mu) > 2$. For the values of the H(125) boson production cross sections predicted in the SM, the expected contribution from the qqh and Vh processes to the final selected sample is estimated to be less than 4% of total signal yield for all tested m_{ϕ_1} hypotheses. The shapes of the two-dimensional (m_1, m_2) distributions are found to be nearly indistinguishable among the three considered production modes, making it difficult to extract individual contributions from these processes in a model independent way. In the following these contributions are neglected, resulting in more conservative upper limits on $(\sigma\mathcal{B})_{\mathrm{sig}}$. Subtraction of the qqh and Vh contributions assuming the SM cross sections for the H(125) production mechanisms would decrease the upper limits on $(\sigma\mathcal{B})_{\mathrm{sig}}$ by less than 4% for all tested values of m_{ϕ_1}. First, the data are examined for their consistency with the background-only hypothesis by means of a fit performed with the normalization of the signal fixed to zero.

Figure 8.1 (left) shows the two-dimensional (m_1, m_2) distribution unrolled into a one-dimensional array of analysis bins after performing the maximum-likelihood fit under the background-only hypothesis. The signal distribution, although not used in the fit, is also included for comparison, for the mass hypotheses $m_{\phi_1} = 4$ and 8 GeV. Table 8.1 presents the number of observed data events, the predicted background yields obtained from a fit under the background-only hypothesis, and the expected signal yields obtained from simulation, for each unique bin in the two-dimensional (m_1, m_2) distribution. The data are well described by the background-only model. The signal cross section times branching fraction is constrained by performing a fit under the signal+background hypothesis, where both the background and signal normalisations are allowed to vary freely in the fit. A representative example of the fit under the signal+background hypothesis at $m_{\phi_1} = 8$ GeV is presented in Fig. 8.1

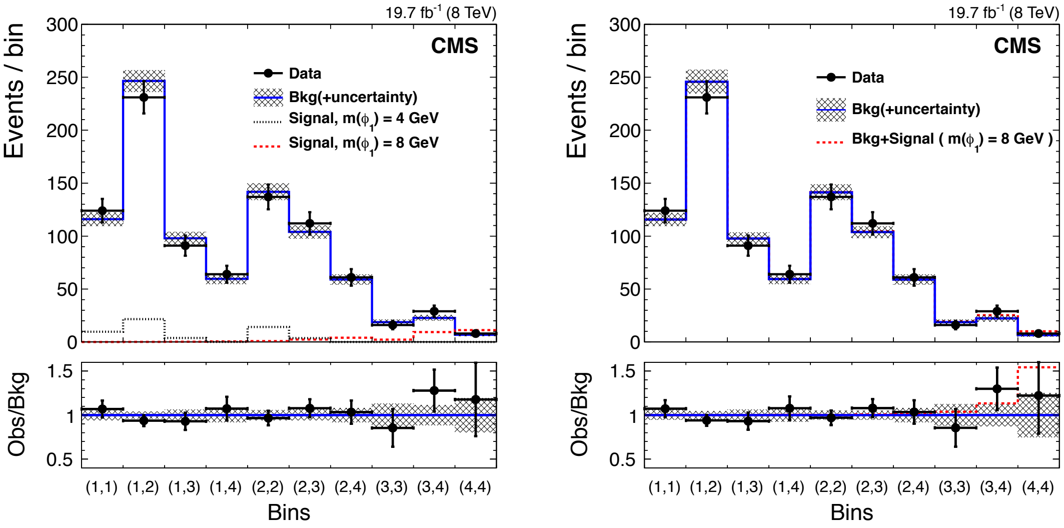

Figure 8.1: The two-dimensional (m_1, m_2) distribution unrolled into a one-dimensional array of analysis bins. In the left plot, data (points) are compared with the background prediction (solid histogram) after applying the maximum-likelihood fit under the background-only hypothesis and with the signal expectation for two mass hypotheses, $m_{\phi_1} = 4$ and 8 GeV (dotted and dashed histograms, respectively). The signal distributions are obtained from simulation and normalized to a value of the cross section times branching fraction of 5 pb. In the right plot, data (points) are compared with the background prediction (solid histogram) and the background+signal prediction for $m_{\phi_1} = 8$ GeV (dashed histogram) after applying the maximum likelihood fit under the signal+background hypothesis. The bin notation follows the definition presented in Fig. 7.1.

(right).

No significant deviations from the background expectation are observed in data. Only a small excess is found for $6 \leq m_{\phi_1} \leq 8$ GeV, with a local significance ranging between 1.2σ ($m_{\phi_1} = 8$ GeV) and 1.4σ ($m_{\phi_1} = 6$ GeV). Results of the analysis are used to set upper limits on $(\sigma\mathcal{B})_{\text{sig}}$ at 95% CL. The modified frequentist CLs criterion [97, 98], implemented in the ROOSTATS package [99], is used for the calculation of the exclusion limits.

Figure 8 shows the observed upper limit on $(\sigma\mathcal{B})_{\text{sig}}$ at 95% CL, together with the expected limit obtained under the background-only hypothesis, for m_{ϕ_1} in the range from 4 to 8 GeV. Exclusion limits are also reported in Table 8.2. The observed limit is compatible

Table 8.1: The number of observed data events, the predicted background yields, and the expected signal yields, for different masses of the ϕ_1 boson in individual bins of the (m_1, m_2) distribution. The background yields and uncertainties are obtained from the maximum-likelihood fit under the background-only hypothesis. The signal yields are obtained from simulation and normalized to a signal cross section times branching fraction of 5 pb. The uncertainties in the signal yields include systematic and MC statistical uncertainties. The bin notation follows the definition presented in Fig. 7.1.

Bin	Data	Bkg.	Signal for $(\sigma\mathcal{B})_{\text{sig}} = 5$ pb, $m_{\phi_1} =$				
			4 GeV	5 GeV	6 GeV	7 GeV	8 GeV
(1,1)	124	116 ± 7	9.7 ± 1.5	1.9 ± 0.5	<0.1	0.1 ± 0.1	<0.1
(1,2)	231	247 ± 10	21.6 ± 2.9	6.8 ± 1.1	1.9 ± 0.5	0.3 ± 0.2	0.1 ± 0.1
(1,3)	91	98 ± 6	3.8 ± 0.8	4.9 ± 0.9	2.4 ± 0.6	0.9 ± 0.3	0.2 ± 0.2
(1,4)	64	60 ± 5	0.1 ± 0.1	1.5 ± 0.4	1.8 ± 0.5	0.8 ± 0.3	0.5 ± 0.2
(2,2)	137	142 ± 8	14.2 ± 2.0	8.2 ± 1.3	2.8 ± 0.6	1.5 ± 0.4	0.8 ± 0.3
(2,3)	112	104 ± 6	3.7 ± 0.7	10.4 ± 1.6	9.2 ± 1.4	4.4 ± 0.8	2.3 ± 0.6
(2,4)	61	59 ± 5	<0.1	2.6 ± 0.6	5.6 ± 1.0	8.1 ± 1.3	4.0 ± 0.8
(3,3)	16	19 ± 2	<0.1	4.8 ± 0.9	4.8 ± 0.9	3.7 ± 0.7	2.2 ± 0.5
(3,4)	29	23 ± 3	<0.1	1.9 ± 0.5	8.0 ± 0.9	11.1 ± 1.5	9.4 ± 1.4
(4,4)	8	7 ± 1	<0.1	<0.1	3.1 ± 0.6	9.1 ± 1.4	11.2 ± 1.7

Table 8.2: The observed upper limit on $(\sigma\mathcal{B})_{\text{sig}}$ at 95% CL, together with the expected limit obtained in the background-only hypothesis, as a function of m_{ϕ_1}. Also shown are $\pm 1\sigma$ and $\pm 2\sigma$ probability intervals around the expected limit.

m_{ϕ_1} [GeV]	Upper limits on $(\sigma\mathcal{B})_{\text{sig}}$ [pb] at 95% CL					
	observed	-2σ	-1σ	expected	$+1\sigma$	$+2\sigma$
4	7.1	5.7	7.6	10.6	14.9	20.2
5	10.3	5.4	7.3	10.3	15.0	21.2
6	8.6	2.8	3.8	5.4	7.8	11.0
7	5.0	1.6	2.2	3.1	4.5	6.5
8	4.5	1.5	2.0	2.9	4.3	6.2

with the expected limit within two standard deviations in the entire tested range of the ϕ_1 boson mass, $4 \leq m_{\phi_1} \leq 8$ GeV. The observed limit ranges from 4.5 pb at $m_{\phi_1} = 8$ GeV to 10.3 pb at $m_{\phi_1} = 5$ GeV.

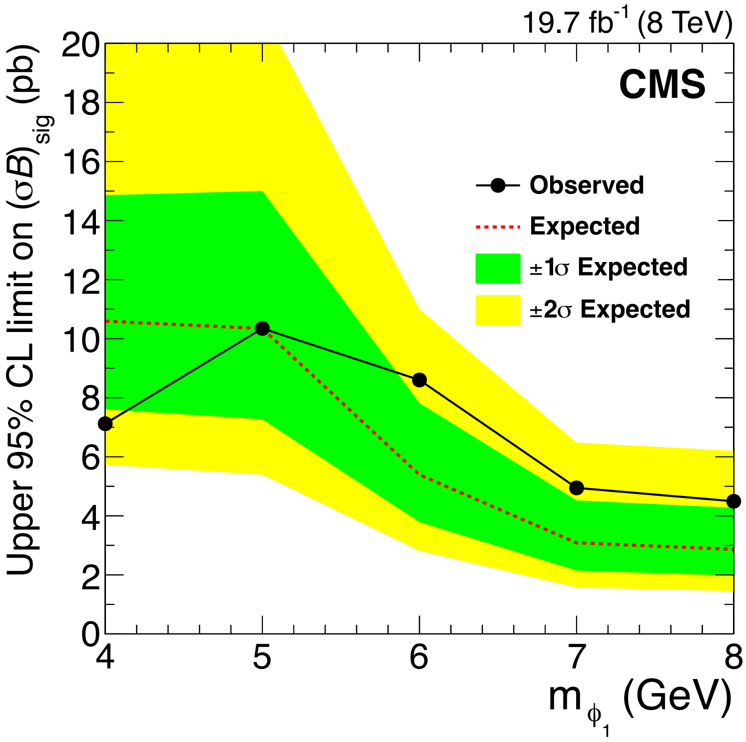

Figure 8.2: The observed and expected upper limits on $(\sigma\mathcal{B})_{\text{sig}}$ in pb at 95% CL, as a function of m_{ϕ_1}. The expected limit is obtained under the background-only hypothesis. The bands show the expected 1σ and 2σ probability intervals around the expected limit.

The expected limit ranges from 2.9 pb at $m_{\phi_1} = 8$ GeV to 10.6 pb at $m_{\phi_1} = 4$ GeV. The analysis presented here complements the search for h/H $\rightarrow a_1a_1 \rightarrow \mu\mu\tau\tau$ performed by the ATLAS Collaboration [100], providing results in the 4τ channel, which has not been previously explored at the LHC.

8.1 Summary

A search for a very light NMSSM Higgs boson a_1 or h_1, produced in decays of the observed boson with a mass near 125 GeV, H(125), is performed on a pp collision data set corresponding to an integrated luminosity of 19.7 fb^{-1}, collected at a centre-of-mass energy of 8 TeV. The analysis searches for the production of an H(125) boson via gluon-gluon fusion, and its decay into a pair of a_1 (h_1) states, each of which decays into a pair of τ leptons. The search covers a mass range of the a_1 (h_1) boson of 4 to 8 GeV. No significant excess above background expectations is found in data, and upper limits at 95% CL are set on the signal production cross section times branching fraction,

$$(\sigma\mathcal{B})_{\mathrm{sig}} \equiv \sigma(gg \rightarrow \mathrm{H}(125))\ \mathcal{B}(\mathrm{H}(125) \rightarrow \phi_1\phi_1)\ \mathcal{B}^2(\phi_1 \rightarrow \tau\tau), \tag{8.1}$$

where ϕ_1 is either the a_1 or h_1 boson. The observed upper limit at 95% CL on $(\sigma\mathcal{B})_{\mathrm{sig}}$ ranges from 4.5 pb at $m_{\phi_1} = 8$ GeV to 10.3 pb at $m_{\phi_1} = 5$ GeV.

Bibliography

[1] CMS Collaboration. Search for the standard model Higgs boson produced in association with a W or a Z boson and decaying to bottom quarks. *Phys. Rev. D*, 89:012003, Jan 2014.

[2] CMS Collaboration. Measurement of Higgs boson production and properties in the WW decay channel with leptonic final states. *Journal of High Energy Physics*, 2014(1):1–86, 2014.

[3] CMS Collaboration. Measurement of the properties of a higgs boson in the four-lepton final state. *Phys. Rev. D*, 89:092007, May 2014.

[4] CMS Collaboration. Updated measurements of the Higgs boson at 125 GeV in the two photon decay channel. 2013.

[5] Kenneth G. Wilson. Confinement of quarks. *Physical Review Letters D*, 10:2445–2459, October 1974.

[6] M. Maki, Z. Nakagawa and S. Sakata. Remarks on the unified model of elementary particles. *Progress of Theoretical Physics*, 28:870–880, November 1962.

[7] N. Cabibbo. Unitary symmetry and leptonic decays. *Physical Review Letters*, 10:531–533, June 1963.

[8] M. Kobayashi and T. Maskawa. CP-Violation in the renormalizable theory of weak interaction. *Progress of Theoretical Physics*, 49:652–657, February 1973.

[9] Michael E. Peskin and Daniel V. Schroeder. *An Introduction To Quantum Field Theory.* Perseus Books Publishing, Reading, Massachusetts, 1995.

[10] A. Pich. Quantum chromodynamics. In *High energy physics. Proceedings, 2nd European School, Sorrento, Italy, August 29-September 1, 1994. Vol. 1, 2*, 1995.

[11] C. N. Yang and R. L. Mills. Conservation of isotopic spin and isotopic gauge invariance. *Physical Review*, 96:191–195, October 1954.

[12] David J. Gross and Frank Wilczek. Ultraviolet Behavior of Non-Abelian Gauge Theories. *Physical Review Letters*, 30, 1973.

[13] Francis Halzen and Alan D. Martin. *Quarks and Leptons.* John Wiley and Sons, Inc, UK, 1984.

[14] Peter W. Higgs. Broken Symmetries and the Masses of Gauge Bosons. *Physical Review Letters*, 13:508–509, 1964.

[15] Peter W. Higgs. Broken Symmetries, Massless Particles and Gauge Fields. *Physical Review Letters*, 12:132, 1964.

[16] C. R. Hagen G. S. Guralnik and T. W. B. Kibble. Global Conservation Laws and Massless Particles. *Physical Review Letters*, 13:585–587, 1964.

[17] Stephen P. Martin. A Supersymmetry primer. 1997. [Adv. Ser. Direct. High Energy Phys.18,1(1998)].

[18] Steven Weinberg. *The Quantum Theory of Fields*, volume 3. Cambridge University Press, 2000.

[19] Michael Benedikt, Paul Collier, V Mertens, John Poole, and Karlheinz Schindl. *LHC Design Report.* CERN, Geneva, 2004.

[20] Oliver Sim Brüning, Paul Collier, P Lebrun, Stephen Myers, Ranko Ostojic, John Poole, and Paul Proudlock. *LHC Design Report.* CERN, Geneva, 2004.

[21] Oliver Sim Brüning, Paul Collier, P Lebrun, Stephen Myers, Ranko Ostojic, John Poole, and Paul Proudlock. *LHC Design Report.* CERN, Geneva, 2004.

[22] CMS Collaboration. Particle-Flow Event Reconstruction in CMS and Performance for Jets, Taus, and MET. Technical Report CMS-PAS-PFT-09-001, CERN, 2009. Geneva, Apr 2009.

[23] CMS Collaboration. Description and performance of track and primary-vertex reconstruction with the CMS tracker. *JINST*, 9(10):P10009, 2014.

[24] CMS Collaboration. Performance of CMS muon reconstruction in pp collision events at $\sqrt{s} = 7$ TeV. *JINST*, 7:P10002, 2012.

[25] Torbjorn Sjöstrand, Stephen Mrenna, and Peter Z. Skands. PYTHIA 6.4 Physics and Manual. *JHEP*, 05:026, 2006.

[26] Johan Alwall, Michel Herquet, Fabio Maltoni, Olivier Mattelaer, and Tim Stelzer. MadGraph 5 : Going Beyond. *JHEP*, 06:128, 2011.

[27] Rick Field. Early LHC Underlying Event Data - Findings and Surprises. In *Hadron collider physics. Proceedings, 22nd Conference, HCP 2010, Toronto, Canada, August 23-27, 2010*, 2010.

[28] Pumplin, J. and Stump, D. R. and Huston, J. and Lai, H. L. and Nadolsky, Pavel M. and Tung, W. K. New generation of parton distributions with uncertainties from global QCD analysis. *JHEP*, 07:012, 2002.

[29] Bozzi, Giuseppe and Catani, Stefano and de Florian, Daniel and Grazzini, Massimiliano. Transverse-momentum resummation and the spectrum of the Higgs boson at the LHC. *Nucl. Phys.*, B737:73–120, 2006.

[30] de Florian, Daniel and Ferrera, Giancarlo and Grazzini, Massimiliano and Tommasini, Damiano. Transverse-momentum resummation: Higgs boson production at the Tevatron and the LHC. *JHEP*, 11:064, 2011.

[31] S. Jadach, Z. Wąs, R. Decker, and J.H. Kühn. The τ decay library TAUOLA, version 2.4. *Computer Physics Communications*, 76(3):361 – 380, 1993.

[32] GEANT4 Collaboration. Geant4 - a simulation toolkit. *Nuclear Instruments and Methods in Physics Research Section A*, 506(3):250 – 303, 2003.

[33] ATLAS Collaboration Collaboration. Observation of a new particle in the search for the Standard Model Higgs boson with the ATLAS detector at the LHC. *Phys. Lett.*, B716:1–29, 2012.

[34] CMS Collaboration. Observation of a new boson at a mass of 125 GeV with the CMS experiment at the LHC. *Phys. Lett.*, B716:30–61, 2012.

[35] CMS Collaboration. Observation of a new boson with mass near 125 GeV in pp collisions at $\sqrt{s} = 7$ and 8 TeV. *JHEP*, 06:081, 2013.

[36] CMS Collaboration. Precise determination of the mass of the Higgs boson and tests of compatibility of its couplings with the standard model predictions using proton collisions at 7 and 8 TeV. *Eur. Phys. J.*, C75(5):212, 2015.

[37] CMS Collaboration. Observation of the diphoton decay of the Higgs boson and measurement of its properties. *Eur. Phys. J.*, C74(10):3076, 2014.

[38] CMS Collaboration. Measurement of the properties of a Higgs boson in the four-lepton final state. *Phys. Rev.*, D89(9):092007, 2014.

[39] CMS Collaboration. Measurement of Higgs boson production and properties in the WW decay channel with leptonic final states. *JHEP*, 01:096, 2014.

[40] CMS Collaboration. Evidence for the 125 GeV Higgs boson decaying to a pair of τ leptons. *JHEP*, 05:104, 2014.

[41] CMS Collaboration. Evidence for the direct decay of the 125 GeV Higgs boson to fermions. *Nature Phys.*, 10:557–560, 2014.

[42] ATLAS Collaboration. Measurement of Higgs boson production in the diphoton decay channel in pp collisions at center-of-mass energies of 7 and 8 TeV with the ATLAS detector. *Phys. Rev.*, D90(11):112015, 2014.

[43] ATLAS Collaboration. Measurements of Higgs boson production and couplings in the four-lepton channel in pp collisions at center-of-mass energies of 7 and 8 TeV with the ATLAS detector. *Phys. Rev.*, D91(1):012006, 2015.

[44] ATLAS Collaboration. Observation and measurement of Higgs boson decays to WW* with the ATLAS detector. *Phys. Rev.*, D92(1):012006, 2015.

[45] ATLAS Collaboration. Evidence for the Higgs-boson Yukawa coupling to tau leptons with the ATLAS detector. *JHEP*, 04:117, 2015.

[46] ATLAS Collaboration. Measurement of the Higgs boson mass from the $H \to \gamma\gamma$ and $H \to ZZ^* \to 4\ell$ channels with the ATLAS detector using 25 fb^{-1} of pp collision data. *Phys. Rev.*, D90(5):052004, 2014.

[47] J. Wess and B. Zumino. Supergauge transformations in four dimensions. *Nuclear Physics B*, 70(1):39 – 50, 1974.

[48] John R. Ellis. Limits of the standard model. In *Lectures given at the PSI Summer School, Zuoz, August 18-24, 2002*, 2002.

[49] Pierre Fayet. Supergauge invariant extension of the Higgs mechanism and a model for the electron and its neutrino. *Nuclear Physics B*, 90:104 – 124, 1975.

[50] P. Fayet. Spontaneously broken supersymmetric theories of weak, electromagnetic and strong interactions. *Physics Letters B*, 69(4):489 – 494, 1977.

[51] Romesh K. Kaul and Parthasarathi Majumdar. Cancellation of quadratically divergent mass corrections in globally supersymmetric spontaneously broken gauge theories. *Nuclear Physics B*, 199(1):36 – 58, 1982.

[52] R. Barbieri, S. Ferrara, and C.A. Savoy. Gauge models with spontaneously broken local supersymmetry. *Physics Letters B*, 119(4):343 – 347, 1982.

[53] H.P. Nilles, M. Srednicki, and D. Wyler. Weak interaction breakdown induced by supergravity. *Physics Letters B*, 120(4):346 – 348, 1983.

[54] J.-M. Frere, D.R.T. Jones, and S. Raby. Fermion masses and induction of the weak scale by supergravity. *Nuclear Physics B*, 222(1):11 – 19, 1983.

[55] J.-P. Derendinger and C.A. Savoy. Quantum effects and SU(2)×U(1) breaking in supergravity gauge theories. *Nuclear Physics B*, 237(2):307 – 328, 1984.

[56] Ulrich Ellwanger, Cyril Hugonie, and Ana M. Teixeira. The Next-to-Minimal Supersymmetric Standard Model. *Phys. Rept.*, 496:1–77, 2010.

[57] M. Maniatis. The Next-to-Minimal Supersymmetric extension of the Standard Model reviewed. *Int. J. Mod. Phys.*, A25:3505–3602, 2010.

[58] Jihn E. Kim and H.P. Nilles. The μ-problem and the strong CP-problem. *Physics Letters B*, 138(1):150 – 154, 1984.

[59] J. R. Espinosa J. A. Casas and I. Hidalgo. The MSSM fine tuning problem: a way out. *Journal of High Energy Physics*, 2004(01):008, 2004.

[60] Radovan Dermíšek and John F. Gunion. Escaping the large fine-tuning and little hierarchy problems in the next to minimal supersymmetric model and $h \to aa$ decays. *Phys. Rev. Lett.*, 95:041801, Jul 2005.

[61] Radovan Dermíšek and John F. Gunion. Next-to-minimal supersymmetric model solution to the fine-tuning problem, precision electroweak constraints, and the largest cern lep higgs event excess. *Phys. Rev. D*, 76:095006, Nov 2007.

[62] Geneviève Bélanger, Ulrich Ellwanger, John F. Gunion, Yun Jiang, Sabine Kraml, and John . Schwarz. Higgs bosons at 98 and 125 GeV at LEP and the LHC. *Journal of High Energy Physics*, 2013(1):1–22, 2013.

[63] G. Belanger, U. Ellwanger, J. F. Gunion, Y. Jiang, and S. Kraml. Two Higgs Bosons at the Tevatron and the LHC? 2012.

[64] John F. Gunion, Yun Jiang, and Sabine Kraml. Diagnosing degenerate higgs bosons at 125 gev. *Phys. Rev. Lett.*, 110:051801, Jan 2013.

[65] John F. Gunion, Yun Jiang, and Sabine Kraml. Could two NMSSM Higgs bosons be present near 125 GeV? *Phys. Rev. D*, 86:071702, Oct 2012.

[66] S.F. King, M. Mühlleitner, and R. Nevzorov. NMSSM Higgs benchmarks near 125 GeV. *Nuclear Physics B*, 860(2):207 – 244, 2012.

[67] S.F. King, M. Mühlleitner, R. Nevzorov, and K. Walz. Natural NMSSM Higgs bosons. *Nuclear Physics B*, 870(2):323 – 352, 2013.

[68] David Curtin, Rouven Essig, Stefania Gori, Prerit Jaiswal, Andrey Katz, Tao Liu, Zhen Liu, David McKeen, Jessie Shelton, Matthew Strassler, Ze'ev Surujon, Brock Tweedie, and Yi-Ming Zhong. Exotic decays of the 125 GeV Higgs boson. *Phys. Rev. D*, 90:075004, Oct 2014.

[69] Ulrich Ellwanger, John F. Gunion, and Cyril Hugonie. Difficult scenarios for nmssm higgs discovery at the lhc. *Journal of High Energy Physics*, 2005(07):041, 2005.

[70] Ulrich Ellwanger, John F. Gunion, Cyril Hugonie, and Stefano Moretti. Towards a no lose theorem for NMSSM Higgs discovery at the LHC. 2003.

[71] U. Ellwanger, J. F. Gunion, C. Hugonie, and S. Moretti. NMSSM Higgs discovery at the LHC. In *Physics at TeV colliders. Proceedings, Workshop, Les Houches, France, May 26-June 3, 2003*, 2004.

[72] Alexander Belyaev, Stefan Hesselbach, Sami Lehti, Stefano Moretti, Alexander Nikitenko, and Claire H. Shepherd-Themistocleous. The Scope of the 4 tau Channel in Higgs-strahlung and Vector Boson Fusion for the NMSSM No-Lose Theorem at the LHC. 2008.

[73] Alexander Belyaev, Jim Pivarski, Alexei Safonov, Sergey Senkin, and Aysen Tatarinov. LHC discovery potential of the lightest NMSSM Higgs boson in the $h_1 \to a_1 a_1 \to 4\mu$ channel. *Phys. Rev. D*, 81:075021, Apr 2010.

[74] Mariangela Lisanti and Jay G. Wacker. Discovering the Higgs boson with low mass muon pairs. *Phys. Rev. D*, 79:115006, Jun 2009.

[75] Mosleh M. Almarashi and Stefano Moretti. Scope of Higgs production in association with a bottom quark pair in probing the Higgs sector of the NMSSM at the LHC. 2012.

[76] M. M. Almarashi and S. Moretti. LHC signals of a heavy CP-even Higgs boson in the NMSSM via decays into a Z and a light CP-odd Higgs state. *Phys. Rev. D*, 85:017701, Jan 2012.

[77] Nils-Erik Bomark, Stefano Moretti, Shoaib Munir, and Leszek Roszkowski. Revisiting a light NMSSM pseudoscalar at the LHC. *PoS*, Charged2014:029, 2015.

[78] S. F. King, M. Mühlleitner, R. Nevzorov, and K. Walz. Discovery prospects for nmssm higgs bosons at the high-energy large hadron collider. *Phys. Rev. D*, 90:095014, Nov 2014.

[79] OPAL Collaboration. Search for a low mass CP-odd Higgs boson in e^+e^- collisions with the OPAL detector at LEP2. *The European Physical Journal C - Particles and Fields*, 27(4):483–495, 2003.

[80] ALEPH Collaboration. Search for neutral Higgs bosons decaying into four taus at LEP2. *Journal of High Energy Physics*, 2010(5):1–19, 2010.

[81] D0 Collaboration. Search for next-to-minimal supersymmetric higgs bosons in the $h \to aa \to \mu\mu\mu\mu$, $\mu\mu\tau\tau$ channels using $p\overline{p}$ collisions at $\sqrt{s} = 1.96$ TeV. *Phys. Rev. Lett.*, 103:061801, Aug 2009.

[82] CMS Collaboration. A search for pair production of new light bosons decaying into muons. *Physics Letters B*, 752:146 – 168, 2016.

[83] ATLAS Collaboration. Search for Higgs bosons decaying to aa in the $\mu\mu\tau\tau$ final state in pp collisions at $\sqrt{s} = 8$ TeV with the ATLAS experiment. *Phys. Rev. D*, 92:052002, Sep 2015.

[84] Ulrich Ellwanger and Cyril Hugonie. NMHDECAY 2.1: An updated program for sparticle masses, higgs masses, couplings and decay widths in the NMSSM. *Computer Physics Communications*, 175(4):290 – 303, 2006.

[85] G. Bélanger, B. Dumont, U. Ellwanger, J. F. Gunion, and S. Kraml. Global fit to Higgs signal strengths and couplings and implications for extended Higgs sectors. *Phys. Rev. D*, 88:075008, Oct 2013.

[86] LHC Higgs Cross Section Working Group Collaboration. Handbook of LHC Higgs Cross Sections: 3. Higgs Properties: Report of the LHC Higgs Cross Section Working Group. Technical Report arXiv:1307.1347. CERN-2013-004, Geneva, 2013. Comments: 404 pages, 139 figures, to be submitted to CERN Report. Working Group web page: https://twiki.cern.ch/twiki/bin/view/LHCPhysics/CrossSections.

[87] The CMS Collaboration. Description and performance of track and primary-vertex reconstruction with the cms tracker. *Journal of Instrumentation*, 9(10):P10009, 2014.

[88] A Perloff and on behalf of the CMS collaboration. Pileup measurement and mitigation techniques in CMS. *Journal of Physics: Conference Series*, 404(1):012045, 2012.

[89] Particle-Flow Event Reconstruction in CMS and Performance for Jets, Taus, and MET. 2009.

[90] Particle-flow commissioning with muons and electrons from J/Psi and W events at 7 TeV. Technical Report CMS-PAS-PFT-10-003, CERN, 2010. Geneva, 2010.

[91] CMS Collaboration. CMS Luminosity Based on Pixel Cluster Counting - Summer 2013 Update. 2013.

[92] A. D. Martin, W. J. Stirling, R. S. Thorne, and G. Watt. Parton distributions for the LHC. *The European Physical Journal C*, 63(2):189–285, 2009.

[93] Simone Alioli, Paolo Nason, Carlo Oleari, and Emanuele Re. NLO Higgs boson production via gluon fusion matched with shower in POWHEG. *Journal of High Energy Physics*, 2009(04):002, 2009.

[94] Paolo Nason. A new method for combining NLO QCD with shower Monte Carlo algorithms. *Journal of High Energy Physics*, 2004(11):040, 2004.

[95] Stefano Frixione, Paolo Nason, and Carlo Oleari. Matching nlo qcd computations with parton shower simulations: the powheg method. *Journal of High Energy Physics*, 2007(11):070, 2007.

[96] Simone Alioli, Paolo Nason, Carlo Oleari, and Emanuele Re. A general framework for implementing NLO calculations in shower Monte Carlo programs: the POWHEG BOX. *Journal of High Energy Physics*, 2010(6):1–58, 2010.

[97] A L Read. Presentation of search results: the CL s technique. *Journal of Physics G: Nuclear and Particle Physics*, 28(10):2693, 2002.

[98] Thomas Junk. Confidence level computation for combining searches with small statistics. *Nuclear Instruments and Methods in Physics Research Section A*, 434(2-3):435 – 443, 1999.

[99] Lorenzo Moneta, Kevin Belasco, Kyle S. Cranmer, S. Kreiss, Alfio Lazzaro, Danilo Piparo, Gregory Schott, Wouter Verkerke, and Matthias Wolf. The RooStats Project. *PoS*, ACAT2010:057, 2010.

[100] ATLAS Collaboration. Search for Higgs bosons decaying to aa in the $\mu\mu\tau\tau$ final state in pp collisions at $\sqrt{s} = 8$ TeV with the ATLAS experiment. *Phys. Rev. D*, 92:052002, Sep 2015.